Astronomy Unit
School of Physics and Astronomy
Queen Mary, University of London

Modelling and analysis of time series of high resolution stellar spectra with differential methods

John Brown Paul Strachan

Supervised by Guillem Anglada-Escudé

Submitted in partial fulfillment of the requirements of the Degree of Doctor of Philosophy

Declaration

I, John Strachan, confirm that the research included within this thesis is my own work or that where it has been carried out in collaboration with, or supported by others, that this is duly acknowledged below and my contribution indicated. Previously published material is also acknowledged below.

I attest that I have exercised reasonable care to ensure that the work is original, and does not to the best of my knowledge break any UK law, infringe any third party's copyright or other Intellectual Property Right, or contain any confidential material.

I accept that the College has the right to use plagiarism detection software to check the electronic version of the thesis.

I confirm that this thesis has not been previously submitted for the award of a degree by this or any other university. The copyright of this thesis rests with the author and no quotation from it or information derived from it may be published without the prior written consent of the author.

Details of collaboration and publications can be found in the Papers section below. All the work in this thesis has been undertaken in collaboration with my supervisor, Dr Guillem Anglada-Escudé. Unless otherwise stated, all figures in this thesis have been created by the author. This work was supported by a Queen Mary University of London PhD studentship.

Signature:
Date:28/02/2020

Abstract and Papers

Abstract

High resolution spectroscopic and photometric surveys of M dwarfs in the solar neighbourhood have detected exoplanets with masses and sizes similar to that of the Earth orbiting in the habitable zone of their parent star. These exoplanets are currently the best candidates for follow up observations for the search for life outside our Solar System. However, high resolution spectra of M dwarfs have blended spectral lines which cause problems for a number of detection and characterisation methods which require the position and identification of each line in the spectrum of the star.

Scattered starlight from an exoplanet, commonly called reflected light, can be used to characterise the planet including the determination of its albedo and inclination of orbit. The relatively low flux ratio between directly observed starlight and starlight scattered off hot Jupiters make these systems prime candidates for detection of reflected light using high-resolution spectroscopy. The first detections have been claimed for 51 Peg b but with spectral lines broader than expected.

We present an algorithm called differential least squares deconvolution (dLSD) to be used in exoplanet characterisation which resolves the problems caused by line blending of spectral lines. We then show how dLSD can be used to measure star-planet obliquity measurements of HD189733 and to characterise short term activity in the M dwarf Ross 154.

We next determine the expected Doppler shift and broadening of starlight scattered off a planet and provide software called REflected STARlighT (RESTART) which given an input stellar spectrum will produce the Doppler shifted and broadened spectrum of the reflected starlight. We use RESTART to demonstrate the broadening in 51 Peg b and predict broadening for other hot Jupiter systems.

dLSD and RESTART will be used in analysis of data in future high resolution spectroscopic surveys of M dwarfs and hot Jupiters.

Papers

Work in this thesis has been published or accepted in the following peer-reviewed papers, in collaboration with the listed authors:

- Strachan, J. B. P. and Anglada-Escudé, G. 2017, Deconvolution method for high precision spectroscopy of stars and exoplanets I. Application to obliquity measurements of HARPS observations of HD189733b. MNRAS, 472, 3467
- Strachan, J. B. P. and Anglada-Escudé, G. 2020, Doppler shifts and spectral line profile changes in the starlight scattered from an exoplanet. MNRAS, Accepted 22nd Jan 2020

Additional work performed as part of the PhD for which I have been a co-author is listed below:

- Dreizler, S., et al., Red Dots: A temperate 1.5 Earth-mass planet in a compact multi-terrestrial planet system around GJ1061. arXiv e-prints, arXiv:1908.04717, August 2019
- Toledo-Padrn, B., et al., Stellar activity analysis of Barnard's Star: very slow rotation and evidence for long-term activity cycle. MNRAS, 488, 5145-5161, October 2019
- Ribas, I., et al., A candidate super-Earth planet orbiting near the snow line of Barnard's star. Nature, 563, 365-368, November 2018
- Quirrenbach, A., et al., CARMENES: high-resolution spectra and precise radial velocities in the red and infrared. Proc. SPIE, p. 107020W, doi: 10.1117/12.2313689, July 2018
- Reiners, A., et al., The CARMENES search for exoplanets around M dwarfs. High-resolution optical and near-infrared spectroscopy of 324 survey stars. A&A, 612, The CARMENES search for exoplanets around M dwarfs. High-resolution optical and near-infrared spectroscopy of 324 survey stars. A&A, 612, A49, April 2018
- Trifonov, T., et al., The CARMENES search for exoplanets around M dwarfs . First visual-channel radial-velocity measurements and orbital parameter updates of seven M-dwarf planetary systems. A&A, 609, A117, February 2018
- Reiners, A., et al., The CARMENES search for exoplanets around M dwarfs. HD147379 b: A nearby Neptune in the temperate zone of an early-M dwarf. A&A, 609, L5, January 2018
- Anglada-Escudé, G., A terrestrial planet candidate in a temperate orbit around Proxima Centauri. Nature, 536, Issue 437-440, August 2016
- Quirrenbach, A., et al., CARMENES: an overview six months after first light. Proc. SPIE, p. 990812, doi: 10.1117/12.2231880, August 2016

Acknowledgements

Firstly I would like to thank my supervisor, Dr Guillem Anglada-Escudé, for his support and mentorship throughout the years of my MSc and then PhD.

My time at Queen Mary has been a thoroughly enjoyable time. I would like to thank the academic and administrative staff of the School of Physics and Astronomy for their friendly support.

I would also like to thank my fellow PhD students at Queen Mary for their good humour and friendship throughout.

I would like to thank my mother and my late father for their support. They were the ones who got my brother and I interested in the natural world around us through outings and walks in the mountains in the North-East of Scotland. I remember climbing to the top of Lochnagar when I was 5 years old and they also bought us our first telescope.

Thanks also to my friends and family who have all shown great support and patience in my astronomy.

Finally thanks to my wife Suzanne who has given me the time and space to carry out my research and has shown me love and understanding throughout.

Contents

1. Summary

In this chapter I explain the purpose of the thesis, provide a brief outline of it, and explain how the different parts of it fit together.

The main purpose of the thesis is to describe algorithms I have developed and report on results using these algorithms that help to build on our knowledge of exoplanets.

Before I do this in the thesis I put this work in context both in terms of our current knowledge in the field and also some motivation as to why we should carry out research in this area.

In terms of the "why" question I start the Introduction Chapter 2 with a discussion as to why knowledge of exoplanets can potentially answer one of the fundamental human questions we have: Is there life beyond the Earth?

Evidence for life on exoplanets will only come after we have first detected them and then have been able to characterise them. So I then move in the next section to a discussion of the different exoplanet detection methods available and then detail distributions of the known exoplanet population in terms of size, mass and distance from host star.

As the algorithms I have developed involve the analysis of high resolution spectroscopic data I go on to describe some current high resolution spectroscopic methods. The first group of these methods are used primarily to detect exoplanets via precision radial velocities (RVs). I introduce an existing differential method here where a time series of spectra are compared with a template built from those spectra in order to calculate precision radial velocities. This method is an improvement over the other RV methods currently used for late type stars, due to its ability to handle line blending and not being subject to errors from line lists which are typically derived from other stars or from incomplete atomic line databases.

Another group of existing spectroscopic methods I go on to describe are those that characterise noise in their parent star. This is crucially important in the exoplanet field as noise from the star can make it difficult or impossible to detect the signals from small, rocky exoplanets and even worse can sometimes appear to mimic the signal from an exoplanet. In particular I discuss the ability of Doppler Tomography

to identify activity such as spots or plages on a rotating star.

I then move on to discuss exoplanet characterisation through a number of different techniques including Rossiter-McLaughlin effect, transmission spectroscopy and high resolution spectroscopy (of thermal emission and reflected starlight from the planet). Transmission spectroscopy and high resolution spectroscopy will eventually provide us with the spectra of small rocky planets and potentially allow us to ascertain whether life may exist on the planet or not. In terms of reflected starlight I note that detection for only one planet has been claimed to date.

At the end of the Chapter 2 I introduce the two main algorithms I have developed and which are the principle subject of the thesis:

1. dLSD (differential Least Squares Deconvolution). This is a differential form of Least Squares Deconvolution where each spectrum is compared via a deconvolution with a high signal to noise template built from an average of each of the observed spectra. The LSD algorithms typically use atomic line lists which are incomplete for late type stars for comparison with the spectra

2. RESTART (REflected STarlighT) - An algorithm which determines what the observed spectrum of reflected light should be taking into account the spectrum of the star, the rotation and sizes of the star and planet and the distance from the star to the planet.

Chapters 3 and 4 describe the use of dLSD to identify distortions in stellar spectral lines caused by two different physical processes. The first is the identification of line profile distortions in high resolution spectra due to an exoplanet transiting its parent star. The second is spectral line profile distortions due to stellar activity on the host star. In the former case I am able to show that dLSD is able to track the exoplanet HD189733b as it transits its host star, I also show that I am able to retrieve the projected spin-orbit misalignment angle for the orbit of the planet with respect to the star and the projected rotational velocity of the star. In the latter case of using dLSD to track spots I was able to fit two spots to spectra obtained for Ross 154. Periodograms of the RVs for the star showed significant periodic behaviour. In tracking the sports I was able to determine the induced radial velocity shifts in the star due to these spots. I removed these velocity shifts from the RVs for the star and then ran periodograms on the resulting RVs. The results from the periodograms showed that the periodic signals had been removed.

In Chapter 5 I describe the RESTART algorithm and show that I am able to explain the broadening in the reflected starlight detected for 51 Peg b using the algorithm.

In the conclusions in Chapter 6 I discuss potential further applications of the algorithms and enhancements to them which I would like to explore in the future. I also discuss the strategic roadmap, in terms of what future plans there are to build large telescopes on the ground and in space with the aim of characterising small, rocky planets and potentially identify signs of life on them. I discuss how the algorithms I have developed could fit into this roadmap.

2. Introduction

2.1. Exoplanets and the quest for the search for life beyond the solar system

For thousands of years, humans have looked up to the starry night sky and pondered some of the big questions about our universe. Are we alone in the universe? Is life only present on the Earth or does it exist out there somewhere else? Did life come to Earth from space or did it develop independently on Earth?

Currently, we have no evidence for life existing outside of the Earth. We also have no evidence whether life originated on Earth or not. We do not understand how to create life. Attempts to find life on other planets or moons of the Solar System has so far failed. Further missions are being proposed to search for life on Mars or the seas under the surfaces of Europa or Enceladus (Clements, 2018). Titan is also another possibility as its conditions on the surface represent to a certain extent those of an early Earth (Coustenis, 1995). However, even if life is found in these parts of the Solar System it is probably not going to be intelligent life and will not be able to communicate with us. If we want to find intelligent life then we are probably going to have to look outside our Solar System.

Early searches for extra-terrestrial intelligence (SETI) outside our Solar System involved both all-sky surveys and targeted searches of stars in the radio and microwave regions e.g. NASAs High Resolution Microwave Survey (Tarter & Gulkis, 1993) in 1992-1993. This government funded research was closed down after a year and most searches since then have been performed by the privately funded SETI institute. Current searches include the search for transients - fast radio bursts - using the Green Bank Telescope (Siemion et al., 2013) and the Very Large Array (Gray & Mooley, 2017). The Breakthrough Listen initiative is currently conducting searches using the Parkes and Green Bank radio telescopes and future searches are planned with the Murchison Widefield Array in Western Australia (Gajjar et al., 2019).

With the discovery of exoplanets other exciting opportunities are now presenting

themselves in the search for life outside the Solar System. An important question is on which planets should we be looking for life or to put it another way which planets are likely to be habitable? Planets could be habitable if they are Earth like (similar mass and size to the Earth) and in a habitable zone where the habitable zone is the region of space around the star which has the right conditions for planets potentially to be able to support liquid water at the surface (Huang, 1959).

Attempts have been made to define habitable zones for planets based on the stellar flux received by the planet and the chemistry in the atmosphere of the planet (Kopparapu et al., 2013) and (Zsom, 2015). The habitable zone for an Earth like planet orbiting a solar type star is 0.99 to 1.7au according to Kopparapu et al. (2013). These planets are difficult to find around nearby stars with current exoplanet detection methods. Transits are rare. The probability for an Earth like planet to transit a solar type star, assuming the orbit of the planet is circular and coplanar with the equator of the star is $\frac{R_*}{a}$ where R_* is the radius of the star and a is the radius of the orbit (Borucki and Summers 1984). So for an Earth like planet orbiting a solar-sized star at 1 astronomic unit the probability of there being a transit is only $\frac{1}{215}$. The amplitude of the radial velocity signal for an Earth like planet orbiting a solar type star is 9cms^{-1} and is too small to currently detect (Lovis & Fischer, 2010).

However, M dwarfs are smaller stars and because of that their habitable zones are much closer to the planet, typically 0.1au (Kasting et al., 1993) and the chances of detecting Earth like planets in the habitable zone is much greater at $\frac{1}{35}$. Nearby transiting planets in the habitable zone of M dwarfs have been found around TRAPPIST-1 (Gillon et al., 2017) and several other M dwarfs. A full list can be found online at the Habitable Exoplanets Catalog (http://phl.upr.edu/projects/habitable-exoplanets-catalog). The current count of transiting planets in the habitable zone which are expected to be rocky is 9.

The next step now is to observe these planets for signs of life. The best way of doing this currently is with transmission spectroscopy where the transmission spectrum of the planet can be obtained (Charbonneau & Deming, 2007). Spectroscopic indicators for life (biosignatures) to look for include oxygen O_2 (Owen, 1980), ozone O_3 and methane CH_4 (Angel et al., 1986). In fact life on Earth produces many more biosignatures than the previous three mentioned (Seager et al., 2012). It should be observed that detecting one of these biosignatures is not sufficiient to state that we have detected evidence for life. For instance, if O_2 was detected it is possible that this formed through an abiotic process on an ice bound planet (Des Marais et al.,

2002).

In addition to searching for individual spectroscopic indicators we could also search for atmospheres whose transmission spectrum is similar to that of the Earth with absorption lines for water, oxygen, ozone and carbon dioxide in the visible to infra-red region and a rayleigh scattering slope (Pallé et al., 2009).

However for the known planets transiting the M dwarfs we will have to wait for the James Webb space telescope (JWST) mission or the next generation of 30 metre telescopes to have instruments which may be sensitive enough to detect these biosignatures.

2.2. Exoplanet detection methods

We saw in the previous section that we will need to increase the sensitivity of our exoplanet detection methods significantly if we want to find candidates in the habitable zone of nearby solar type stars. Here I discuss the different exoplanet detection methods and give a bit of their history.

2.2.1. Pulsars and the timing method

The first planets detected outside the Solar System were planets orbiting pulsars. Pulsars are fast rotating neutron stars which had formed after the collapse of the star from a supernova. The pulsars are highly-magnetised and emit a narrow beam of radiation parallel to their magnetic dipole axis. This beam of radiation can be detected using radio telescopes where it appears as a very regular periodic pulse. The first pulsar detected was reported by Hewish et al. (1968). Detection of planets around pulsars is possible by the timing detection method. A planet orbiting around the pulsar causes the pulsar itself to orbit around the centre of mass of the system. This barycentric motion means that a difference in the period of the pulse can be observed provided the inclination of the orbit is not face on to the observer. The difference in period is due to the different distances the light from the beam travels, and thus the time taken to reach the observer, depending on where the pulsar is on its orbit. The amplitude in the change of period τ_p is given by (Perryman, 2018):

$$\tau_p = \frac{1}{c} \frac{a \ \sin i \ m_p}{m_*} \tag{2.1}$$

where c is the speed of light a is the semi-major axis, i is the inclination of the orbit and m_p and m_* is the mass of the planet and star respectively.

The first planetary mass objects were (minimum mass 2.8 and 3.4 Earth masses) detected orbiting pulsar PSR B1257+12 (Wolszczan & Frail, 1992). To date 16 planets have been detected around pulsars according to the online exoplanet encyclopaedia http://exoplanet.eu (Schneider et al., 2011).

Timing methods have also been used to detect planet candidates orbiting pulsating stars (Schuh et al., 2010) and eclipsing binaries (Sybilski et al., 2010). A timing method called transit timing variations has also been used to detect several planets. In this method the existence of the planet is inferred from from its gravitational tug causing a change in the transit time of a known transiting exoplanet in the system (Agol et al., 2005).

2.2.2. Astrometry

The main searches for planets orbiting main sequence stars were initially attempted using astrometry. Astrometry measures the position of stars on the sky. Astronomers had measured the motion of some binary stars around their barycentre e.g. the motion of Sirius due to it having a white dwarf companion (Bessel, 1844) so it was plausible that the same method could be performed to measure the motion of stars due to planets orbiting them. In fact, Peter Van der Kemp in 1963 claimed detection of a 1.6 Jupiter mass planet orbiting Barnards star with a period of 24 years (van de Kamp, 1963). Unfortunately the signal turned out to be due to instrumental systematic effects which had been difficult to identify due to the long timeframe of observations.

To understand why it is difficult to detect exoplanets using astrometry I look at the amplitude of the observable we are trying to detect. We assume a two body system where the planet and star have circular orbits around the centre of mass of the system. The observer will detect a circular motion of the star if the orbit is face-on, a straight line if the orbit is edge on, or an ellipse otherwise. We define a to be the semi-major axis (radius) of the orbit of the planet. The magnitude of the observable α which is the angular semi-major axis α made by the orbit of the star is given by (Wright & Gaudi, 2013)

$$\alpha = \left(\frac{M_p}{M_*}\right)\left(\frac{a}{1au}\right)\left(\frac{d}{1pc}\right)^{-1} arcsec; \tag{2.2}$$

where d is the distance from the star to the observer and M_p and M_* are the mass of the planet and the star respectively.

From the equation we can see that α will be larger and thus easier to detect for

massive planets which orbit nearby stars on large orbits. Plugging numbers into the equation we see that a Jupiter mass planet orbiting a solar type star at a distance of 10 parsecs from us will have $\alpha = 500\mu$as. An Earth twin at 10 parsecs would have $\alpha = 0.3\mu$as.

Before Gaia, Hipparcos was the primary space mission which ran from 1989 to 1993 and measured the position of stars. It had a sensitivity for α of 1 mas (Perryman et al., 1997) which helps to explain given the figures in the previous paragraph why detection of exoplanets with astrometry has been so difficult.

In fact it was not until 2010 that an astrometric detection of an exoplanet was made (Muterspaugh et al., 2010). Only a handful of exoplanets have been detected to date using astrometry. This should change with the Gaia space mission which has a precision of 20-25 μas for stars down to 15th magnitude. The expectation is that over 20,000 high mass long period planets ere expected to be detected over its 5 year mission Gaia (Perryman et al., 2014).

2.2.3. The first exoplanets and the radial velocity method

The radial velocity (RV) exoplanet detection method involves measuring the Doppler shift of the spectrum of the star due to its motion about the barycentre caused by the gravitational tug from an exoplanet. The motion of the star around its barycentre is depicted in Figure 2.1. As the inclination of the orbit of the star cannot be determined from the RV method only a minimum mass for the planet can be determined. This method for detecting exoplanets had been considered since at least the 1950s (Struve, 1952) where it was conjectured that Jupiter mass planets which orbited close in to the star (0.05au) would have an RV amplitude of 0.2kms^{-1} which may be detectable using the spectrographs at that time. However it was not until the end of the 1980s that an object HD114762b (Latham et al., 1989) with minimum mass less than the 13 Jupiter mass brown dwarf limit was detected using the CORAVEL (Baranne et al., 1979) and the Centre for Astrophysics (Connes, 1985) echelle spectrographs. The minimum mass measured for the object was 11 Jupiter masses and the conclusion was that even though the object may be a giant planet it was more probable that it would be a brown dwarf. It has since been confirmed that HD114762b was a brown dwarf from Gaia data (Kiefer, 2019).

The first exoplanet orbiting a main sequence star detected by the radial velocity method was 51 Peg b from astronomers based at Geneva (Mayor & Queloz, 1995). The planet was on a very short period orbit of just over 4 days and also had a significant minimum mass of 0.47 Jupiter masses. The time series of the radial

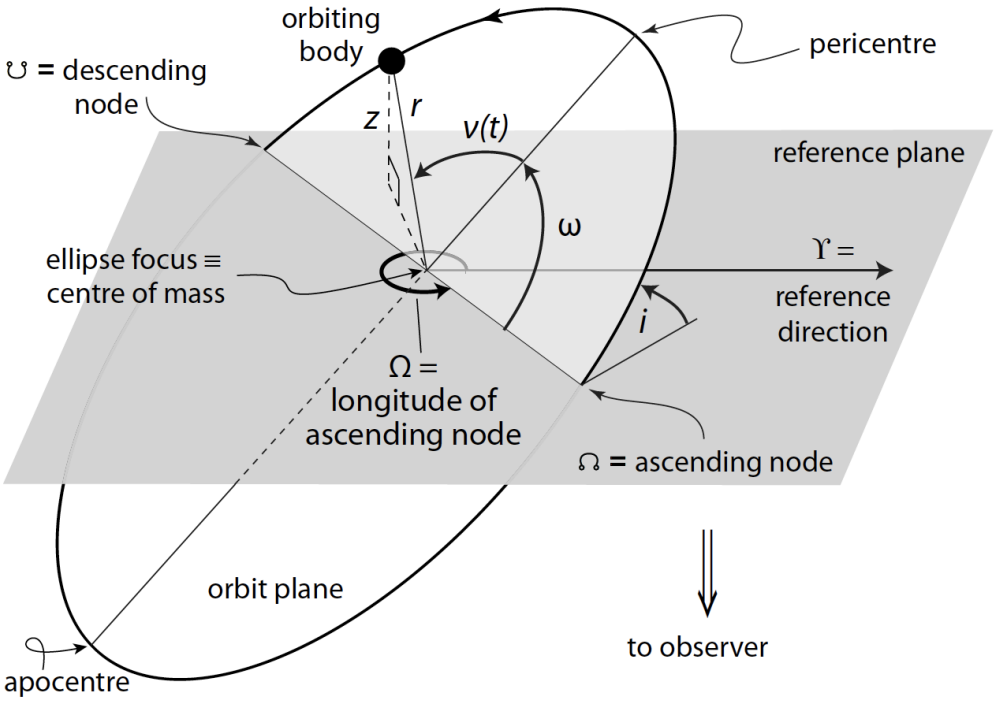

Figure 2.1.: The orbit of a body around the centre of mass taken from Perryman (2018). In the RV method the orbiting body is the star and the centre of mass is the barycentre for the system. The reference plane is the plane of the sky. The three angles defining the orientation of the orbit with respect to the plane of the sky: ω - the argument of pericentre, Ω - longitude of ascending node and I - inclination are shown.

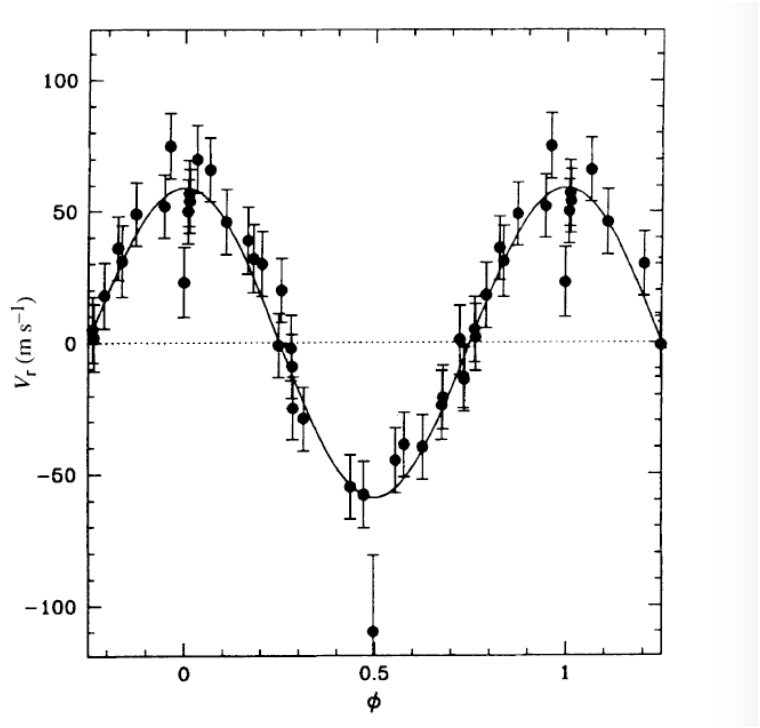

Figure 2.2.: The radial velocities of 51 Peg phase folded to the period of the planet taken from Mayor & Queloz (1995).

velocities phase folded to the period of the planet is shown in Figure 2.2. The detection caused great interest in the astronomy community not just because it was the first planet detected orbiting a main sequence star but because there was no analogue for this type of planet in our Solar System. This led to questions about how such a massive planet could be formed and end up in such a short period orbit to its parent star.

The detection of 51 Peg b was quickly confirmed by the Lick Observatory group (Marcy & Butler, 1995) and two other planets were reported by this group the following year orbiting 70 Viginius (Marcy & Butler, 1996) and 47 Ursae Majoris (Butler & Marcy, 1996) using the Hamilton echelle spectrograph.

The detection of the first exoplanets using the radial velocity method, along with the confirmation in particular of hot Jupiters using the transit method (see Section 2.2.4), gave impetus to the development and improvements in precision of high resolution spectrographs and in the increase of on-sky time dedicated to search for them. By 2010 several instruments were reaching the 1ms^{-1} precision level including: HIRES on the Keck 10 metre telescope (Vogt et al., 2000), HARPS on the ESO 3.6 metre telescope (Mayor et al., 2003) and PFS on the Magellan II 6.5 metre telescope (Crane et al., 2010). With higher precision spectrographs astronomers

were able to detect exoplanets with smaller minimum masses. The first Neptune mass planet GJ436b was detected using the Keck HIRES spectrograph in 2004. It had a minimum mass of 21 Earth masses making it the lowest mass planet then found (Butler et al., 2004). Gillon et al. (2007) identified that the planet transits and were able to confirm that as well as having a similar mass to Neptune the planet also had a size of 3.95 Earth radii similar to that of Neptune. The first super Earth mass planet (which has a mass in the range 2 - 10 Earth masses (Stevens & Gaudi, 2013), detected in 2005 was GJ 876d using the Keck HIRES spectrograph. It had a mass just under 7 Earth masses (Rivera et al., 2005). 55 Cnc e is another super Earth initially detected in 2004 wiith a mass of 14 Earth masses (McArthur et al., 2004). This mass was subsequently reduced to 8.3 Earth masses (Dawson & Fabrycky, 2010) which is within the super Earth range.

Section 2.4 shows that Earth mass planets orbiting in the habitable zone of M dwarfs have an RV amplitude of the order of $1ms^{-1}$ With precisions down to $1ms^{-1}$ for HARPS and approaching that for CARMENES (Quirrenbach et al. (2010) and Trifonov et al. (2018)) these spectrographs give an ideal opportunity to detect Earth mass planets orbiting M dwarfs. To date five exoplanets have been detected with minimum mass less than 1.2 Earth masses from these spectrographs: YZ Ceti b, c and d (Astudillo-Defru et al., 2017b) and Teegarden's star b and c (Zechmeister et al., 2019).

In 2016 a planet with a minimum mass of 1.27 Earth masses was found orbiting our nearest star Proxima Centauri (Anglada-Escudé et al., 2016) using the HARPS spectrograph.

The ESPRESSO (Echelle Spectrograph for Rocky Exoplanet and Stable Spectroscopic Observations) spectrograph González Hernández et al. (2018) has been in operation since 2018. On quiet stars it has already demonstrated RV precision of 25 cm^{-1} over a full night. This spectroscope and the next generation of spectroscopes to be installed on 30 metre telescopes in the next decade are expected to get to a precision at the 10 cms^{-1} level. This level is approaching the 9 cms^{-1} RV signal of Earth mass planets orbiting Sun like stars at approximately 1AU and will potentially give us the opportunity to detect these planets.

The successes of the RV method allowed astronomers to study the distribution of planets detected in terms of for instance their mass against period. Section 2.3 discusses this further.

2.2.4. The transit method

A transit occurs when an observer views a planet passing in front of its host star. The transit detection method relies on detecting the reduction in flux observed during the transit caused by the planet occluding some of the light from the star. This method had already been mentioned in papers as far back as the 1950s (Struve, 1952). The transit is periodic giving the period of the orbit of the planet. We define the transit depth ΔF as

$$\Delta F = \frac{F_* - F_T}{F_*} \tag{2.3}$$

where F_* is the flux of the star outside transit and F_T is its flux in transit. Given knowledge of the radius of the star R_*, the radius of the planet R_p can then be determined (Seager & Mallén-Ornelas, 2003)

$$R_p = \sqrt{R_*^2 \Delta F}. \tag{2.4}$$

In addition the orbital inclination of the planet can be determined from the shape of the light curve of the transit. The first reported exoplanet transit detection had to wait until 1999 when a partial transit (ingress) was reported for HD 209458 (Henry et al., 1999) and then for complete transits of it Charbonneau et al. (2000). The complete transits are shown in Figure 2.3.

Ground based surveys followed such as HAT (Hungarian Automated telescope project (Bakos et al., 2011)) and WASP (Wide-Angle search for planets (Pollacco et al., 2006)) and discovered 100s of transiting planets. However it is difficult for ground based photometry to get better precision than 0.1% due to variable atmospheric extinction and scintillation. Even current state of the art ground based surveys such as NGTS (Next Generation Telescope Survey) operate with a precision of 0.1% (Wheatley et al., 2018). This permits Neptune sized planets around Solar like stars to be detected but detecting transiting Earth sized planets around Solar like stars is currently not possible from the ground. The answer to get round this limitation was to go to space. There have been three major space missions which had a focus on capturing exoplanet transits. The first mission was CoRoT (Convection, Rotation and planetary Transits Auvergne et al. (2009)) and the survey ran from 2007 to 2013. Thirty-two planets were detected by CoRoT according to the extrasolar planets encyclopaedia (Schneider, 2011). Most notably CoRoT-7b the first rocky exoplanet was detected. This planet has a radius 1.58 times that of Earth and a mass of 7.42 Earth masses giving a mean density of $\rho = 10.4 \pm 1.8$ gm

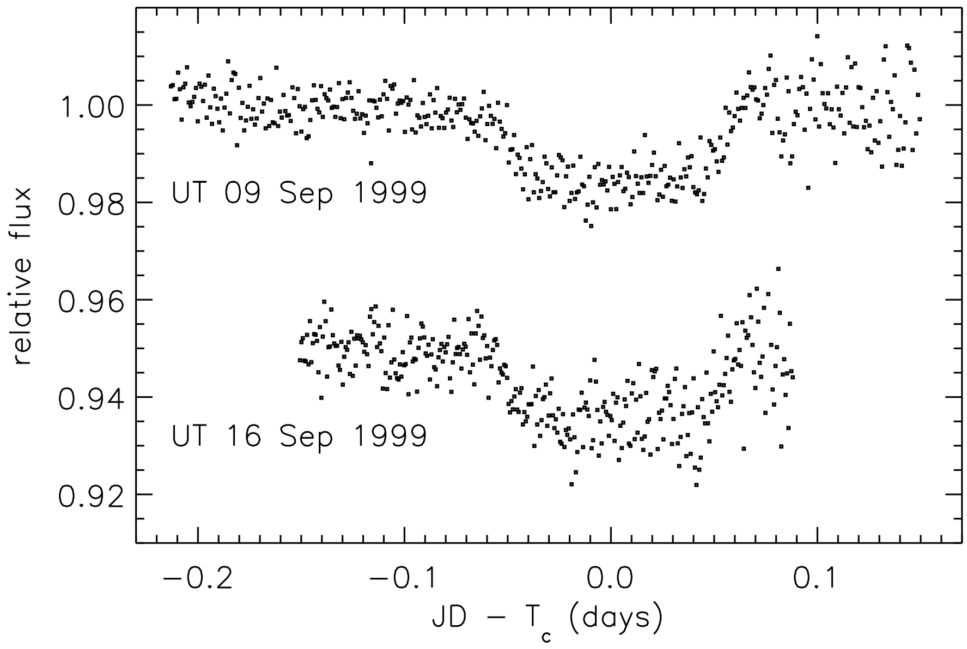

Figure 2.3.: The photometric time series of two transits of HD209458. The data from 16 Sep are offset by -.05 relative to those from 9 Sep (Charbonneau et al., 2000)

cm^3 which is almost twice that of the Earth.

The second space mission was Kepler (Borucki et al., 2010). Its main mission was to perform continuous monitoring of one region of the sky. The main mission ran from May 2009 to May 2013 until it suffered a hardware failure which affected its pointing abilities. A revised follow-on K2 mission (Howell et al., 2014) took place after the hardware failure and ran from May 2014 to Oct 2018 when it ran out of fuel. The main Kepler mission was a stunning success with 2316 confirmed planets detected on the the main mission and 104 on K2 according to the extrasolar planets encyclopaedia (Schneider, 2011). Just under 150 planets the size of the Earth or smaller were detected with the smallest planet Kepler-37b having less than a third of the radius of the Earth (Barclay et al., 2013). However, none of these were in the habitable zone. Additional successes of the Kepler mission included detecting planets on circumbinary orbits e.g. Doyle et al. (2011), resonant systems of planets e.g. Mills et al. (2016) and occurence rates (Batalha, 2014). For instance we now know that there are likely to be more planets than stars in the galaxy.

The third space mission is TESS (Transiting Exoplanet Survey Satellite (Ricker et al., 2009)). It is an all-sky 2 year survey with the aim of observing over two million bright stars in order to find transits. The two year mission started in April

2018 and so far has 29 confirmed planets and just under 1000 planet candidates according to the NASA TESS website. The TESS mission has been extended to 2022. TESS is expected to detect over 14,000 planets with 280 smaller than two Earth radii (Barclay et al., 2018a).

2.2.5. Direct imaging

Direct imaging appears at first instance to be the most straightforward method of detecting exoplanets. Take an image of the star and planet using a Charge Coupled Device (CCD) and then separate the light of the planet from that of the star in the pixels of the image.

But detecting planets using direct imaging is extremely challenging (Traub & Oppenheimer, 2010) due to

- the extremely small apparent angle subtended at the observer between the planet and the star making it difficult to separate the light from the planet and the star. For a Jupiter - Sun like system at 10 parsecs the angle is 0.5 arcsecs.
- the extremely small flux ratio between the planet and the star. Typical flux ratios in the optical range from 5×10^{-5} for close in large exoplanets called Hot Jupiters to 7×10^{-9} for a Jupiter like exoplanet or 5×10^{-10} for an Earth like exoplanet in a system similar to our Solar System (Martins et al., 2016);
- turbulence in the atmosphere for ground based observations causing distortions in the light.

Typical sensitivity for direct imaging from high contrast imaging systems such as SPHERE (Spectro-Polarimetric High-contrast Exoplanet REsearch) permit detections at a contrast of 7×10^{-7} at an angular separation of planet from star at 0.3 arcsecs (Mesa et al., 2015).

Despite the difficulties direct imaging has had some notable success to date with over 130 exoplanet candidates detected with masses up to 36 Jupiter masses (Schneider et al., 2011). Most are young, hot, self-illuminated planets which are still bright.

The direct imaging method is limited to systems where the planet is far enough away from its parent star in the plane of the sky so that the light from the parent star can be separated from the planet. Techniques used to suppress and help separate starlight from the planet signal include using coronographs to block the light from the star and adaptive optics to help correct for the distortions in the light due to

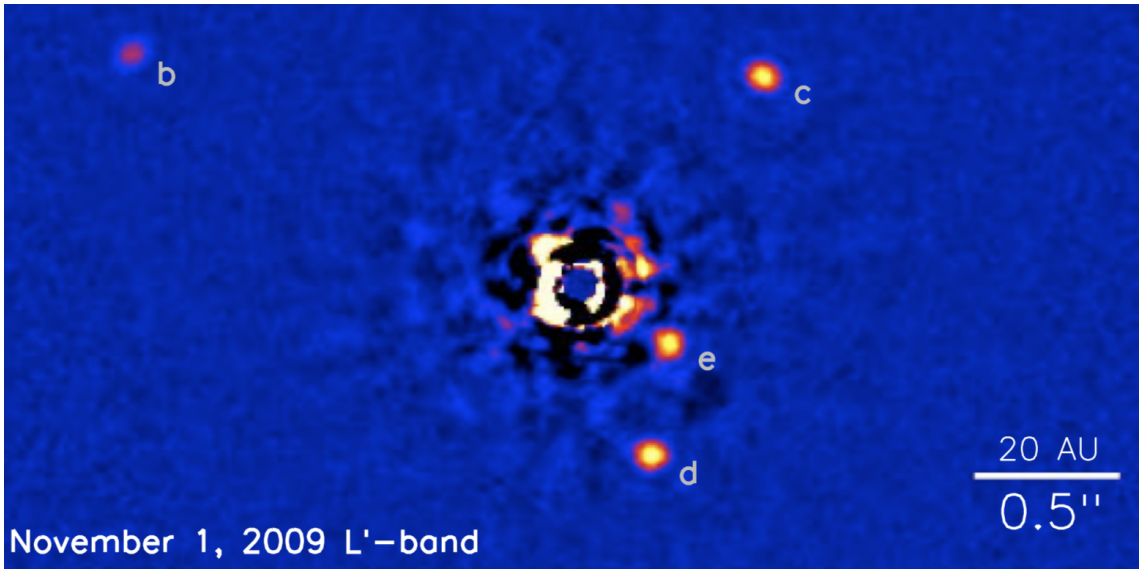

Figure 2.4.: Results of direct imaging of HR8799 (Marois et al., 2008) showing the four planets b, c, d and e. The parent star which has had most of its light suppressed bar some residual speckles is in the centre of the image.

the turbulence in the atmosphere of the Earth. Angular differential imaging (ADI) is also commonly used to remove artifacts caused by surface errors in the primary mirror and internal optics (Marois et al., 2006). These defects appear as bright speckles in the images. They can be differentiated from planet signals by taking a sequence of observations of the system whilst rotating the field. The speckles that do not move during the field rotation are instrinsic to the optics of the telescope and are removed. The first exoplanet detected using this method was 2M J1207. It is a 5 Jupiter mass planet orbiting the brown dwarf 2MASSWJ 1207334-393254 (Chauvin et al., 2004).

A significant system detected is HR8799 (Marois et al., 2008) which is shown in Figure 2.4. The system is young and the planets are hot and bright. The planets are all tens of astronomical units away from their parent star.

2.2.6. Microlensing

A consequence of general relativity is that a massive object distorts spacetime and this causes light to bend as it passes the object. The first detection of the bending of light by a massive object was by Sir Arthur Eddington who was able to detect the deflection of starlight from stars near the line of sight of the sun during the 1919 solar eclipse (Eddington, 1919).

Gravitational microlensing occurs when light from a distant star (the source)

comes in alignment with the lens (the planet and its host star) with respect to the observer. As the source approaches alignment its light is magnified and this can then be detected using photometry. The amount of magnification in the case of a binary lens (the planet and its host star) relies on the solution to a lens equation which does not have an analytic solution (Wright & Gaudi, 2012).

If there are no planets accompanying the star then for a lensing event the light curve shows a symmetric peak. If there is a planet then there will be a distortion on the symmetric light curve of the host star. The observables from microlensing include the mass ratio of the planet to its host star and the transverse distance between the planet and the host star.

Microlensing is different to all the other exoplanet detection methods in that it does not use light from the planet or the host star for the detection but only the light from the source star. The sensitivity of the method extends down to planets of size 0.1 Earth masses and microlensing is most sensitive to planets at orbital separations of 1.5-4AU (Bennett, 2008).

The first microlensing event reported in 2004 for an exooplanet was for the event OGLE 2003-BLG-235/MOA 2003-BLG-53 where a 2.6 Jupiter mass planet was detected with a planet to star separation of 4.3au (Bond et al., 2004). The light curve of the detection is given in Figure 2.5.

According to the Exoplanet Encyclopaedia there have been 99 planets detected with the microlensing method. Microlensing is a one off event and although it is sensitive enough to detect Earth mass planets these, objects are usually too far away and thus are generally too faint to perform detailed follow-up characterisation of the planet. (Boisse et al., 2015) performed a follow-up on OGLE-2011-BLG-0417 but were not able to confirm the microlensing results due to probably a blended lens.

A future space-based microlensing survey could provide a nearly complete statistical census of extrasolar planets with masses down to 0.1M Earth masses at all separations greater than 0.5au (Bennett, 2008).

2.3. Distribution of detected planets

Given that more than 4000 planets have been detected we can look at the population of this data to see trends in the sizes, masses and periods of the planets. All detection data in this section is taken from the exoplanet encyclopaedia (Schneider et al., 2011).

Figure 2.6 shows the radius against period for the transiting planets from Kepler.

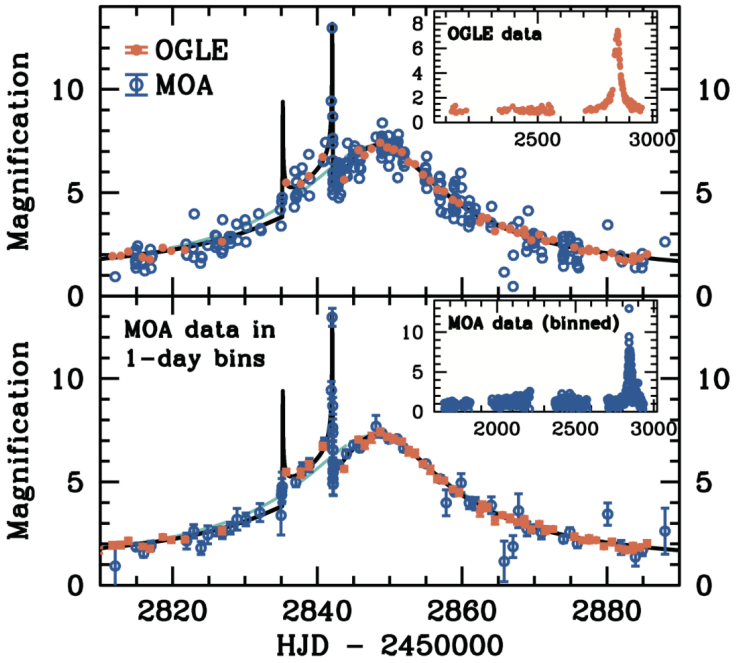

Figure 2.5.: Light curve with best-fitting and single-lens models of the microlensing exoplanet detection event O235/M53. The OGLE ((Optical Gravitational Lensing Experiment (Udalski et al., 1993)) and MOA (Microlensing Observations in Astrophysics (Muraki et al., 1999)) measurements are shown as red filled circles and open blue circles, respectively. The top panel presents the complete data set during 2003 (main panel) and the 20012003 OGLE data (inset). The bottom panel is the same as the top panel, but with the MOA data grouped in 1 day bins, except for the caustic crossing nights, and with the inset showing MOA photometry from 2000 to 2003. The binary- and single-lens fits are indicated by the solid black and cyan dashed curves, respectively. Figure from Bond et al. (2004)

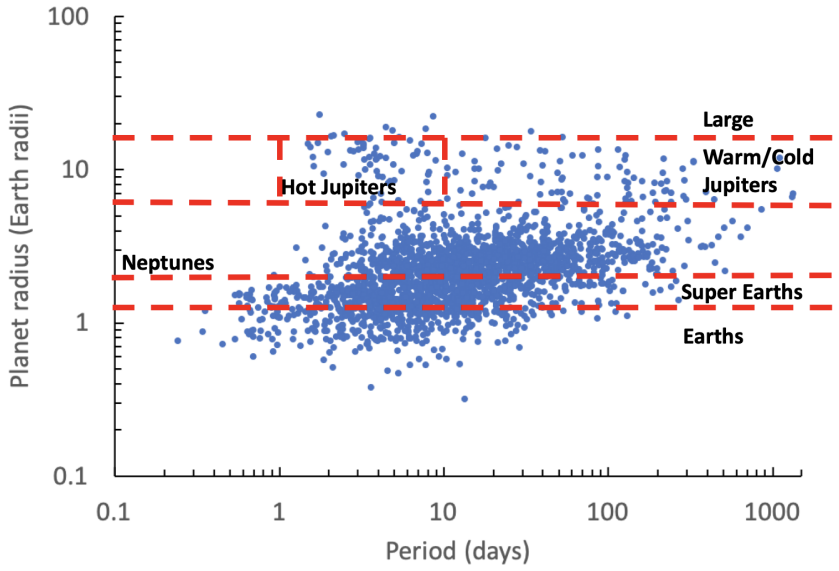

Figure 2.6.: Period against planet size for planets detected by the *Kepler* mission

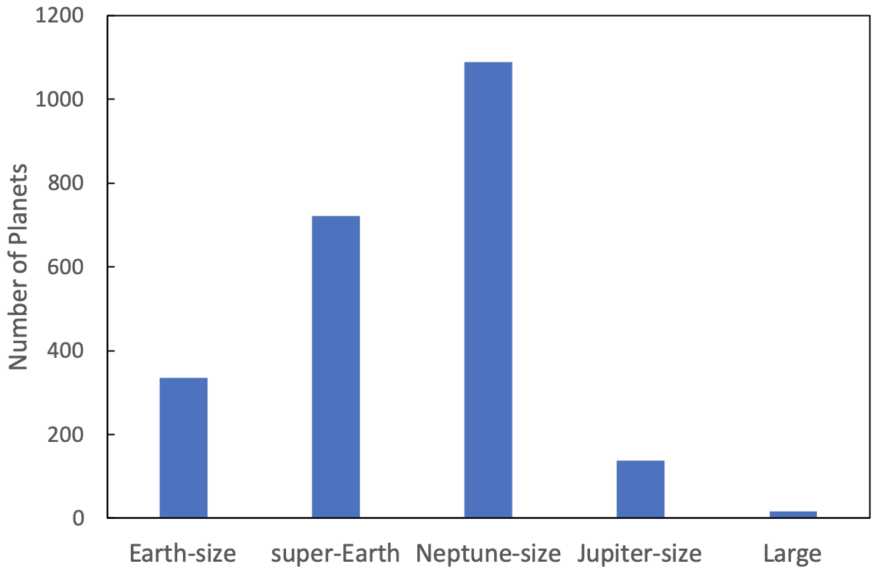

Figure 2.7.: Number of *Kepler* planets grouped by size followiing Borucki et al. (2011) classification. Earth-size less than 1.25 Earth radii. Super-Earth 1.25 to 2.0 Earth radii. Neptune size 2.0 to 6.0 Earth radii. Jupiter size 6 to 15 Earth radii. Large greater than 15 Earth radii.

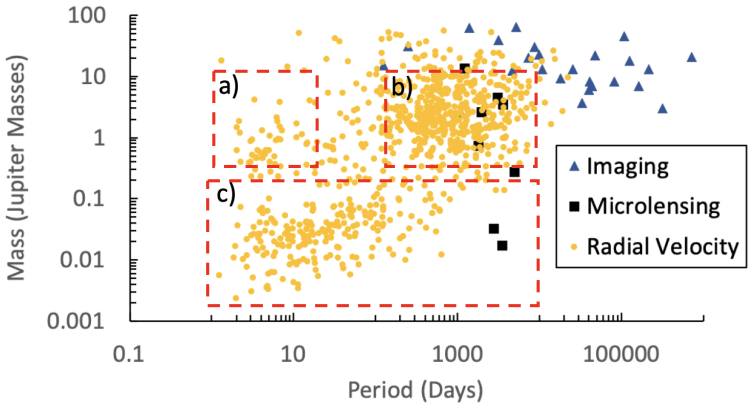

Figure 2.8.: Mass against period for planets detected with the RV, microlensing and direct imaging detection methods. Box a) is the grouping of hot Jupiters. Box b) is the grouping of longer period Jupiters. Box c) is the gouping of Earths, Super Earths and Neptunes.

Most of the Kepler planets have periods less than 100 days and size 0.9 to 6 Earth radii. Above this main group are the Jupiter sized planets. The cluster of hot Jupiters can be seen in the region with period between 1 and 10 days and size around 12 Earth radii. These planets are grouped by size in Figure 2.7 using the planet classifications given in Borucki et al. (2011). The super-Earths group (1.25-2 Earth radii) have no counterparts in the Solar System.

Figure 2.8 shows the mass against period for the planets detected by the radial velocity method. A cluster of large Jupiter mass planets can be seen centred on a period of around 1000 days. A small cluster of Hot Jupiters can also be seen between 3 and 10 days near to Jupiter mass. The cluster near the bottom left are super Earths. The blank regions at the bottom and right of the diagram are where the RV method is not yet sensitive enough to explore these regions of parameter space. This is due to the planets that may exist there either being too small and/or too far away from the parent star to cause a strong enough RV signal to be detected.

In Figure 2.8 we have also has plotted the microlensing and direct imaging planets with known masses. We can see that microlensing and direct imaging allows us to sample the parameter space beyond the radial velocity detections. In particular direct imaging allows us to detect massive planets (larger than Jupiter mass) beyond 10,000 days. The microlensing technique allows us to detect lower mass planets with periods beyond 1000 days and below the detection limits of radial velocity searches.

2.4. How to measure precise RVs

2.4.1. Precision required to detect exoplanets

The main challenge with the radial velocity detection method is the high level precision required of the RV measurements. The level of precision required can be determined from the two-body (star and planet) model. The radial velocity semi-amplitude K for the star is

$$K = (v_{max} - v_{min})/2, \tag{2.5}$$

where v_{max} is the maximum RV of the star due to its orbit around the barycentre of the system and v_{min} is the minimum. K in terms of practical units (Lovis & Fischer, 2010) is given by

$$K = \frac{28.4329 ms^{-1}}{\sqrt{1-e^2}} \frac{m_p \sin I}{M_{Jup}} \left(\frac{m_* + m_p}{M_{Sun}} \right)^{-1/2} \left(\frac{a}{1au} \right)^{-1/2}, \tag{2.6}$$

where e is eccentricity, I is the orbit inclination, a is the semi-major axis of the orbit and m_* and m_p are the masses of the star and planet respectively.

In terms of numbers this means for a hot Jupiter on a 0.1 au circular orbit with $vsinI = 1$ (orbit seen edge on by observer) and the host star is of solar mass then we have K = 89.8 ms^{-1}. For an Earth massed planet orbiting round a solar mass star at 0.1au and 1.0au we have K = 0.28 and 0.09 ms^{-1} respectively.

Less precision is required to find planets in the habitable zone around smaller stars such as M dwarfs. For an Earth mass planet around a 0.1 solar mass M dwarf at 0.1 au then K = 0.9 ms^{-1}.

2.4.2. Doppler information in spectra

The precision achievable in RV measurements depends on the Doppler information in the spectrum of the star and its signal to noise ratio (SNR). Connes (1985) and Butler et al. (1996) both determined the limit of RV measurements related to the Doppler information in the spectrum. Butler et al. (1996) found that the RV error was inversely proportion to the weighted sum of squares of the derivative of the intensity of each pixel of the spectrum with respect to velocity, namely

$$\sigma_{\overline{v}} = \frac{1}{\sqrt{\Sigma_i \left(\frac{dI_i/dV}{\epsilon_i} \right)^2}} \tag{2.7}$$

where $\sigma_{\overline{v}}$ is the velocity error over a spectrum of length $\overline{v}$, i is the pixel number, dI_i/dV is the derivative of the intensity at pixel i with respect to velocity v and ϵ_i is the uncertainty in the intensity at pixel i.

This implies that spectra with sharp lines and thus in general having larger gradients dI_i/dV will have a larger denominator in the above equation and thus a smaller error in the measured velocity. Thus means that there is more Doppler information in spectra with narrow lines as opposed to broader lines. The above equation also implies not surprisingly that the more lines in the spectrum there are the better the velocity precision.

Given the fact that hot stars ($>$ 10,000K) have very few lines in the optical and infra-red and cool stars ($<$ 3,500K) have broader blended lines (Lovis & Fischer, 2010) reported that the best spectral types to get the highest precision RV measurements are for spectral type F, G and K stars.

They reported that for M dwarfs the early to mid M dwarfs were better measured in the optical due to a lack of Doppler information in the near infra-red which would not be made up for by the additional flux in that region. For late M dwarfs the near infra-red (750 - 2500nm) would be better than the optical range (380-750nm) if NIR instruments could achieve the level of precision of optical ones. This is in agreement with Reiners et al. (2010) who reported that only when reaching spectral type M4 did RV measurements in the Y band (960-180nm) of the NIR become as precise as in the optical (given equally efficient instruments) and only for very late M spectral types did all bands in the NIR have an advantage.

2.4.3. Two techniques to obtain precision RV measurements

The two main techniques that have permitted RV measurements at the ms^{-1} level are the iodine cell technique and the simultaneous reference technique

Iodine Cell Technique

The possible improvement in radial velocity precision down to a level of 10 ms^{-1} by using telluric lines which are imprinted on the stellar lines as the starlight passes through the atmosphere of the Earth had been recognised by Griffin (1973). Using telluric lines for calibration in this way still had its problems in terms of line coverage and also the variability of the telluric lines depending on the changing volume of water and oxygen in the atmosphere and the altitude of the star in the sky. A better solution found was to put a cell containing low pressure Hydrogen Fluoride (HF) directly in front of the slit of the spectrograph (Campbell & Walker, 1979).

This method achieved an RV precision 15 ms^{-1}. However the HF cell was soon superceded by the iodine cell as it has better line coverage over 500 to 630nm where there were at least twenty lines per nm (HF only had coverage over 10nm in the 500 to 630nm range), it is non-lethal and is inexpensive (Marcy & Butler, 1992).

Precisions down to 3 ms^{-1} level are obtainable (Butler et al., 1996) because the iodine lines imprinted on the stellar spectrum have the same instrumental distortions as the stellar lines. In order to extract the Doppler shift a fit is performed between the observed spectrum of the star with the iodine lines imprinted on it $I_{obs}(\lambda)$ and a model spectrum. The model spectrum is the product of the intrinsic spectrum of the Iodine cell $T_{I2}(\lambda)$ with the Doppler shifted intrinsic high SNR template of the star $I_s(\lambda + \Delta\lambda)$ convolved with the instrumental profile (PSF)

$$I_{obs}(\lambda) = k[T_{I2}(\lambda)I_s(\lambda + \Delta\lambda)] * PSF. \tag{2.8}$$

The intrinsic spectrum of the iodine cell is obtained from a prior observation using a Fourier Transform Spectrograph which has a negligible instrument response as it operates at an extremely high resolution (1,000,000) and SNR is also very high (700). The intrinsic high SNR template of the star is obtained by deconvolving a high signal to noise observation of the star with the instrument profile. The instrumental profile is obtained from observing a fast rotating B star (a featureless spectrum) through the iodine lamp and then deconvolving this observation with the intrinsic spectrum of the iodine cell (Butler et al., 1996).

Since the PSF varies across the spectrum, the spectrum is broken into chunks and each chunk is fitted. The fit for each chunk involves 15 free parameters which include the Doppler shift $\Delta\lambda$, wavelength of first pixel, dispersion, continuum normalisation and the free parameters for the PSF which are modelled using a sum of Gaussians (Valenti et al., 1995). The precision of the Doppler measurement is the standard deviation of the velocities for each chunk.

Due to the large number of parameters involved, this technique is computationally very intensive. Obtaining a high resolution perfectly calibrated spectrum of the star is often not possible and obtaining an intrinsic template of the star is also difficult to achieve. Despite these difficulties RVs of ms^{-1} precision have been achieved using this technique. Another disadvantage with the technique is that the iodine gas cell absorbs a large fraction of the flux from the star.

Simultaneous reference technique

The other leading technique to obtain precision radial velocity measurements, the simultaneous reference technique, relies on building a very stable spectrograph which is fiber-fed and is calibrated externally typically using emission lamps. This technique was pioneered by a group from Geneva led by M. Mayor. Examples of this type of spectrograph include ELODIE (Baranne et al., 1996), HARPS and ESPRESSO. ELODIE and HARPS use Thorium-Argon lamps for calibration (Lovis & Pepe, 2007) and HARPS is able to get down to an RV precision of 1ms^{-1}. ESPRESSO (Pepe et al., 2013) uses a laser frequency comb (LFC) for improved calibration as it provides more regularly spaced calibration lines. In its ultra high resolution mode (R=134,000) and improved temperature and pressure stability it is expected to be able to attain significantly less than 1 ms^{-1} precision.

Typically there are two side-by-side fibres in these spectroscopes which follow the same optical path (Baranne et al., 1996). One fibre for collecting the starlight - the science fibre - and the other for the calibration source but it can also be used on the sky.

This simultaneous reference technique allows the tackling of the three problems of instrument profile, wavelength calibration and measuring the Doppler shift of the star to be carried out separately giving it the advantage of greater spectral range and no contamination from calibration lamps on the stellar spectrum.

First, because the instrument is stable and image scramblers are coupled to the fibres to scramble the light from the star the instrument profile is stable.

Secondly, the wavelength calibration is performed by collecting calibration spectra during the night using the calibration fibre. This allows the determination of any velocity shifts due to the instrument during the night. Also, any velocity offsets between the two fibres can be determined by taking a Thorium Argon lamp calibration of both fibres at the start of the night and comparing them.

Thirdly, high precision RV measurements can be made using the calibrated spectra. Here we describe three methods and detail some of their strengths and limitations.

The first method to measure RV measurements to the ms^{-1} level is by the use of cross correlation functions (CCFs). In this method the observed stellar spectrum is cross correlated with a mask (Figure 2.9). The mask has binary values (ones or zeroes) and has value one at the position of the absorption lines for the star of the given type. Elsewhere the mask is zero (Baranne et al. (1979) and Baranne et al. (1996)). A modification to apply weights to the mask corresponding to the strength

of the line of the star was made as that gave improved results Pepe et al. (2002). The CCF, which typically looks like a single absorption line, has the benefit of increasing the signal to noise of a factor of the square route of the number of lines assuming the counts of the flux recorded follow a Poisson distribution. The radial velocity of the CCF is the position of the minimum of the CCF. To achieve better precision the RV is obtained by fitting a Gaussian to the CCF and using the centroid position of the Gaussian.

The CCF technique although extremely successful has a small number of limitations:

1. The reliance on a mask of a given spectral type may have some inaccuracies. The lines in the star may have different strengths to those indicated in the mask due to metallicity or other physical properties of the star which were different to the one that was used as reference in the creation of the template.

2. The CCF method runs into difficulties when the spectral lines of the star are blended. It is difficult to identify the central position of each line if the lines are blended. Even if the line positions are identified correctly then carrying out the cross-correlation process will cause inaccuracies. This is due to including contributions from the same line more than once in the correlation process where it overlaps with another line. Ignoring the blended lines is one way forward but this may not be practical to do with later type stars due to the large numbers of molecular lines. For example the ExoMol line list for TiO has approximately 60,000,000 transitions and many of the lines from these transitions will be blended. (McKemmish et al., 2019).

The second method to measure precision RVs is a differential method. It is called a differential method as the RVs are determined only from spectra of the star and do not use line lists or masks. This differential method was introduced by Anglada-Escudé & Butler (2012) and is called HARPS-TERRA. HARPS-TERRA uses the wavelength calibrated spectra from HARPS. It creates a high signal to noise template built from the individual spectra. The template is built iteratively from the observations. The template is initially the observed spectrum with the highest signal to noise. This template is then fitted to each spectra using least squares where the velocity is one of the free parameters in the fit. Once fitted a new template is created by combining all the observed spectra after moving them to be at the velocity of the original template. This process is repeated iteratively until there is

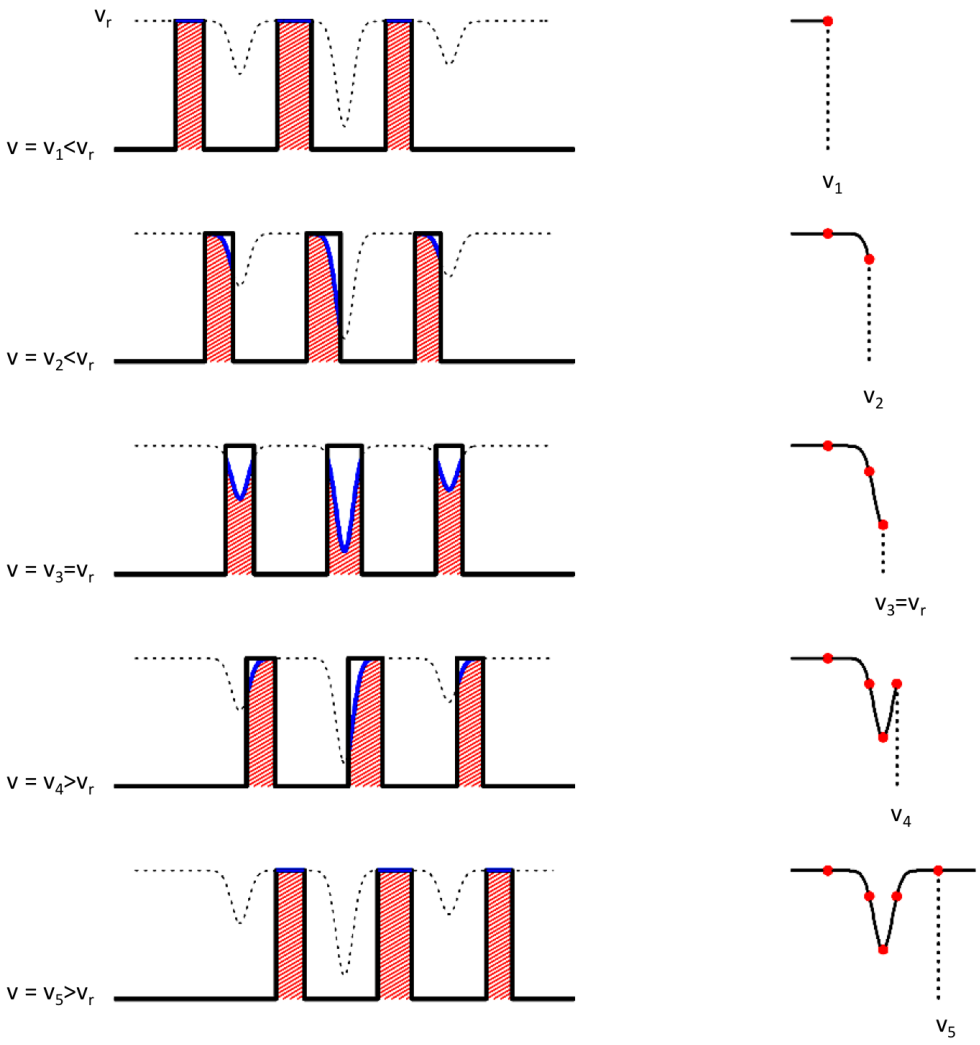

Figure 2.9.: Depiction of the creation of the CCF at five different velocities v_1 to v_5. On the left the dotted line is the spectrum of the star which is at a velocity v_r. and the mask is the solid line black line. The CCF at each point is calculated from the area of the mask (in red hatch) that overlaps with the spectrum and is depicted on the right. Adapted from Eggenberger & Udry (2010).

no significant statistical improvement in the fit. The errors in the fit for each radial velocity come from the error matrix in the least squares fit.

This method has performed as well as or better than the CCF method though there are still some limitations with this differential method:

1. The template as it is built from observations will have a finite SNR and as such the template can never be a perfect replica of the star.

2. Dumusque (2018) stated that for earlier type stars there are parts of the spectrum which have no absorption lines and only have a relatively flat continuum. In these regions there is no Doppler velocity information. The differential method by default would still compare these regions and these regions would only add noise to the velocity estimate. A simple way to avoid this is to mask out the regions of the continuum so that the contributions from these regions are ignored in a similar way to functionality in HARPS-TERRA that can currently mask out active regions of stars e.g. hydrogen alpha, Ca H and K lines.

(Dumusque, 2018) have developed a third method determining precision RVs. This method determines the RV of the star by first determining the RV of each of the individual lines of the spectrum. This method requires creating a high signal to noise template of the spectrum of the star which each individual spectrum is then compared against. A weighted average of the velocities of the lines is then calculated to give the overall radial velocity. It was shown that this method had the same precision as the CCF method used for HARPS.

An advantage with this method is that analysis of the RVs of each line can be performed to look for outliers which may be caused by stellar activity or may be due to the instrument such as errors in the HARPS detector stitchings (Coffinet et al., 2019). This method has the disadvantage like the CCF method of being difficult to use for late type stars which have the majority of their lines blended.

2.4.4. Stellar noise

An additional limitation on the level of RV precision that can be reached is activity on the star. Physical processes taking place on the star cause distortions and shifts in the stellar lines observed with a spectrograph. These distortions and shifts are commonly called astrophysical noise or jitter and can seriously undermine our attempts to measure the RV of the star about its barycentre.

The stellar activity has been separated into four groups for G and K type dwarfs (Dumusque, 2016):

- Stellar oscillations on timescales of a few minutes for solar-like stars. These oscillations are caused by pressure waves and propagate to the surface of the star and cause contraction and expansion which result in RV signatures of 0.1 to 4 ms^{-1} depending on the type of star and its age. For the sun the period of the oscillation is 5 minutes.

- Stellar granulation on timescales of a few minutes to 48 h. Granulation occurs due to convection and has an RV signature of approximately 1 ms^{-1}.

- Short-term stellar activity on the timescale of the stellar rotation period. The activity is induced by rotation in the presence of surface magnetic inhomogeneities which characterise themselves on the surface of the star as mainly dark spots or bright plages. The RV signature of this activity can be quite large ranging from 1 to 50 ms $^{-1}$ for G stars.

- Long-term stellar activity on timescales of several years, which is induced by stellar magnetic cycles. The sun has an 11 year solar cycle and as it approaches its peak of activity the number and area of spots on the sun is at its largest. This has an impact on RV measurements as convection is inhibited in active areas and the convective blue shift in those areas (see Figure 2.10) is decreased causing the RV of the star to be red shifted. Shifts of the orders of 10 ms^{-1} can be seen in the sun and other stars (Dumusque et al., 2011b).

M dwarfs are also known to have short-term and long-term activity cycles (Suárez Mascareño et al., 2018) and (Hosey et al., 2015) and are expected also to have very small oscillations but to date no oscillations have been detected (Rodríguez et al., 2016).

Several methods have been used to treat stellar noise when attempting to detect exoplanets.

For the stellar oscillations (Chaplin et al., 2015), the most straightforward way of dealing with them is to have observations with integration times that will average out the effect of the oscillations. For instance Collier Cameron et al. (2019) used 5 minute integration times on the Sun which has whose period of oscillation is 5 minutes. RV surveys of stars often choose a long 15 minute integration time to average out the effect of the oscillations ((Dumusque et al., 2011a).

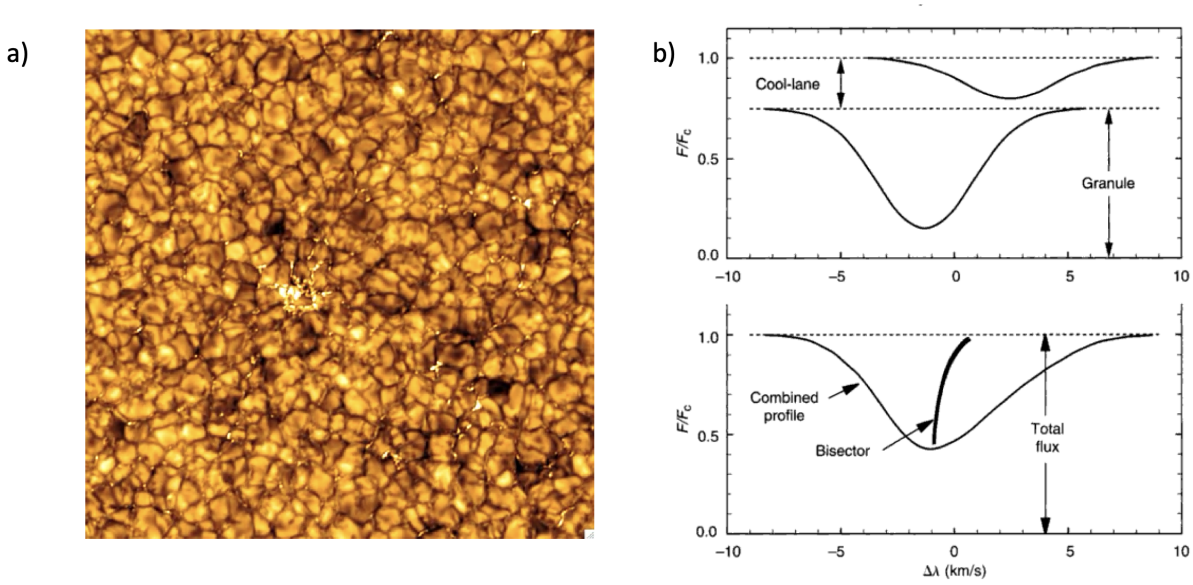

Figure 2.10.: Convective blueshift in a spectral line. Panel a) shows granulation in the sun. The light granules are blobs of hot gas rising. The granules are surrounded by small dark intergranular cool lanes which are composed of gas sinking. Panel b) shows a spectral line for the cool lanes (red shifted due to the gas sinking and for the granules which is blue shifted due to the gas rising. What the observer sees for a distant star is a combination of these which is the convective blue shiifted line at the botttom. Adapted from Gray (2005).

For granulation taking several observations per night and then binning the observations (Dumusque et al., 2011a) over a given time period helps to reduce the stellar noise but does not remove it completely.

For short-term stellar activity a large number of methods have been used:

- fitting sine waves at the known rotation period of the star and to its harmonics (Boisse et al., 2011),
- using correlated noise models to fit the data (e.g.Feroz & Hobson (2014), Gregory (2011) and Tuomi & Anglada-Escudé (2013)),
- using the FF′ method if contemporaneous photometry exists (Aigrain et al., 2012),
- modelling activity-induced signals in RVs with Gaussian process regression, whose covariance properties are shared either with the stars photometric variations (Haywood et al. (2014); Grunblatt et al. (2015); (Aigrain et al., 2016)) or a combination of several spectroscopic indicators (Rajpaul et al. (2015)), or determined from the RVs themselves (Faria et al. (2016)),
- using linear correlations between different observables, i.e., RV, bisector span (BIS SPAN (Queloz et al., 2001) see Figure 2.11) and full width at half maximum (FWHM) of the cross correlation function (CCF, Baranne et al. (1996); Pepe et al. (2002)), photometry (Robertson et al. (2015); Boisse et al. (2009); Queloz et al. (2001)), and magnetic field strength (Hébrard et al. (2014)),
- identifying activity due to it being wavelength dependent (Tuomi et al. (2013) and Feng et al. (2017)).

In this thesis I develop a differential method which looks to treat short term activity due to rotation. This method is based on Doppler imaging. Doppler imaging is described in Section 2.5 and the full details of the differential method are given in Chapter 4.

For long-term stellar activity, the calcium chromospheric activity indicator correlates well with the RVs (Dumusque et al., 2012).

2.5. Doppler imaging (DI) of stars

The previous section discussed short term activity due to rotation. Here we look at a technique which maps the surface of stars from this activity.

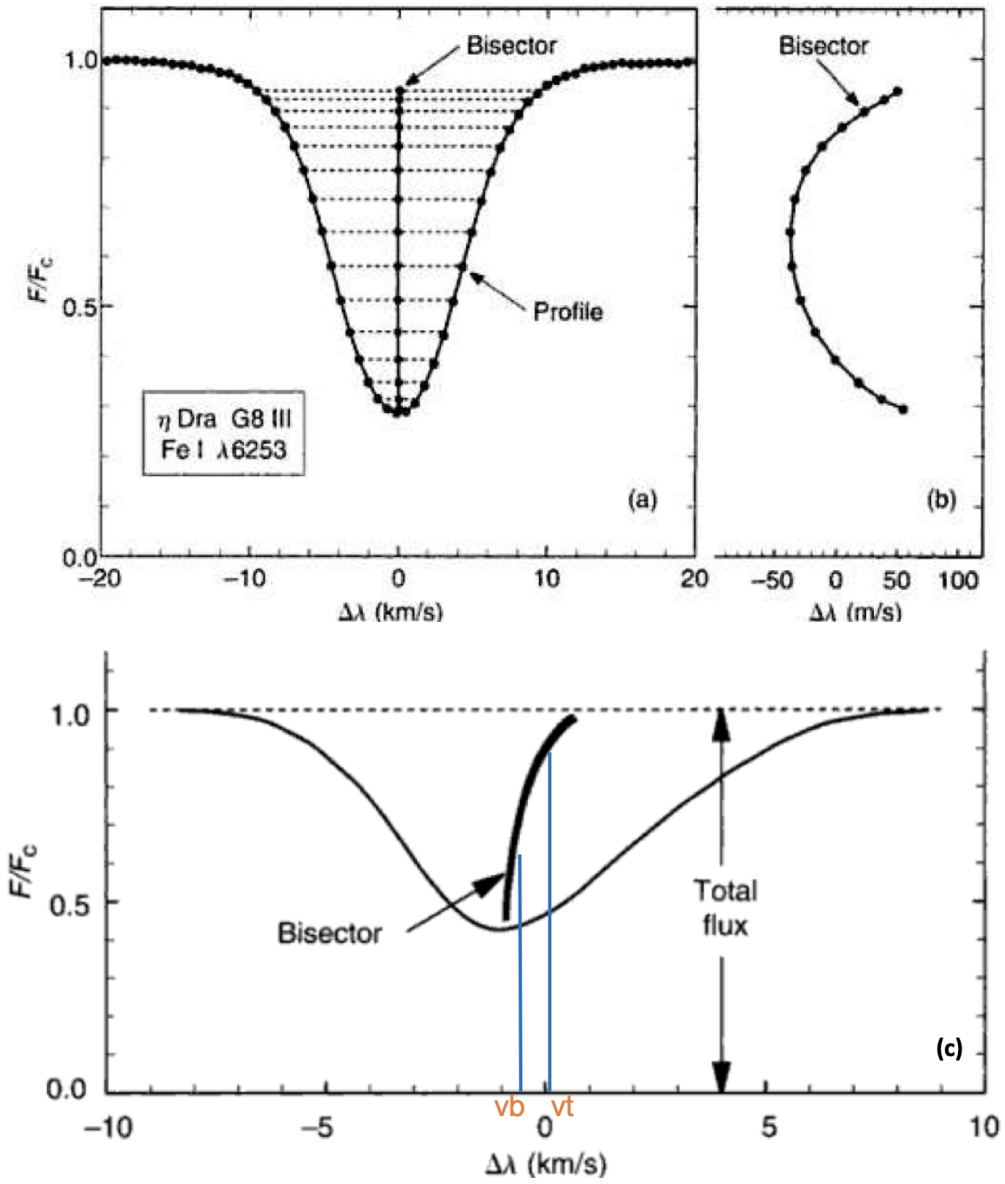

Figure 2.11.: Panel (a) shows an absorption line along with its line bisector for a solar type star. The line bisector is determined by measuring the midpoint of the line at different values of flux. Panel (b) shows the line bisector with the velocity axis now in ms^{-1} where the line bisector appears as C shape. Panel c) shows where the bisector inverse span is calculated from. The bisector inverse span equals vt - vb, where vt is the mean bisector velocity between 10-40% of the line depth (top), and vb is that between 55-90% (bottom). Figure adapted from Gray (2005).

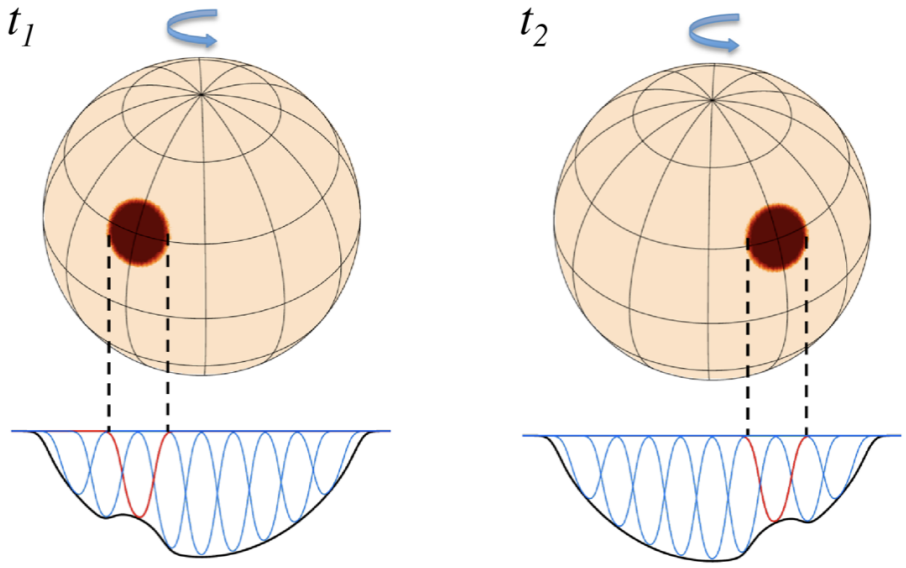

Figure 2.12.: Surface of a rotating star with a dark spot at two times t_1 and t_2. Below image of star depiction of spectral absorption line containing the bump caused by the darkenss of the spot as it moves across the star. Adapted from (Kochukhov, 2016) .

Star spots are created by magnetic fields on the surface of stars in the same way as sun spots. Most stars which have convective outer layers or are fully-convective are expected to have spots. The number of stars which have spots can be estimated from the number of stars on the cool side of the granulation boundary. This number is around 200 billion in the galaxy (Strassmeier, 2009). This is important as spots are likely to have an impact on the RV measurements (see Section 2.4.4) of many stars and this will be detrimental to the detection of exoplanets using the RV method.

The description below of the technique of using time series of spectra to produce a surface map of the spots of the star commonly known as Doppler imaging (Vogt & Penrod, 1983) is largely based on Kochukhov (2016)

Spots cause distortions on the spectral lines from the star. For spots with long term stability, in terms of size and lifetime, the variability of the distortion of the spectral lines is only caused by the observer's changing view of the spot as the star rotates. For a dark spot the distortion is a small positive bump moves which moves across the spectral line as the spot moves across the star. The longitude of the spot can be determined from the Doppler shift of the bump with respect to the centre of the spectral line (Figure 2.12).

Spots located at different latitudes have bumps that move across the absorption

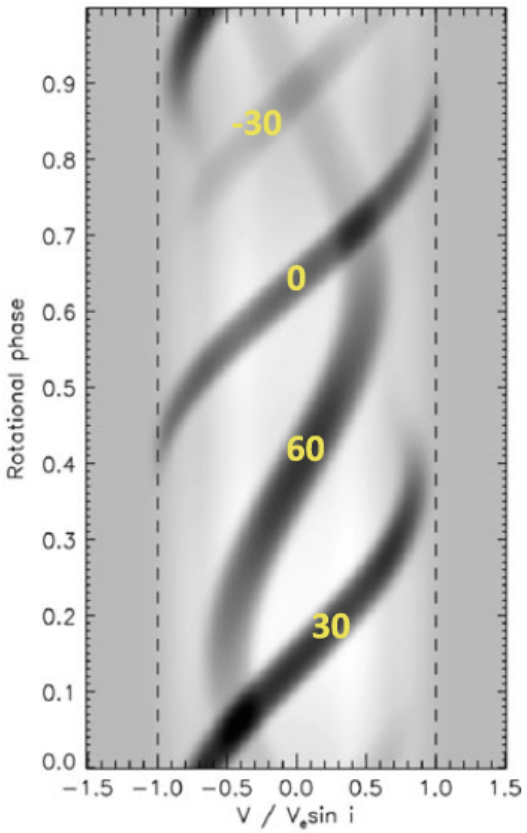

Figure 2.13.: As the star rotates the spot signature moves across the line profile from blue to red. The rectangular panel shows the dynamic difference spectrum (absorption line of star without spots subtracted from absorption line of star with spots) as a function of the rotational phase. In this case, the stellar surface has four small spots at latitudes 30, 0, -30, and 60 degrees. This plot demonstrates how temporal variation of the spot signatures depends on their latitude position. Adapted from Kochukhov (2016).

lines in different ways. A spot near the stellar rotational equator has a bump on the absorption lines that is visible during half of the rotation period and moves quickly across the absorption line. Spots close to a rotational pole that is visible to the observer have bumps on the absorption lines that are visible during a larger fraction of the rotational cycle and the bump is constrained to move more slowly near the centre of the line (Figure 2.13).

A key question to consider is the spatial resolution we expect to get from DI. This clearly depends on the projected rotational velocity (vsinI) of the star as this puts a limit on how far the bump can move along the spectral line and the resolution of the spectrograph. The size of a resolvable velocity element v_R in the spectrum of a spectrograph is given by

$$v_R = \frac{c}{R}, \tag{2.9}$$

where R=$\frac{\lambda}{\Delta\lambda}$ is the resolution of the spectroscope and c is the speed of light. The angular size of the resolution element at the equator Δl in degrees is given by:

$$\Delta l = 90\ \frac{v_R}{v \sin I} \tag{2.10}$$

.

For the HARPS spectroscope (R = 115000) for a star with vsinI = 10kms^{-1} we have $\Delta l = 23.5°$. This is for a single spectrum and in order to characterise a spot in terms of its size and shape the spot would need to be of a size of several of these resolution elements. However with DI we work with a time series of spectra and significant additional resolution is achievable from using the rotational modulation information in the spectra.

Early attempts to obtain the position and size of spots on the surface of the star ran into numerical problems as this inverse problem was ill-posed. There were too many solutions that could fit the data set. The breakthrough came when Goncharskii et al. (1977) used regularisation methods to ensure uniqueness of the DI solution. Regularisation is an additional penalty term which is added to the χ^2 accuracy term which we want to minimise

$$\sum_i [S_{obs}(v_i) - S_{syn}(v_i)]/\sigma_i^2 + \kappa R(\mathbf{v}). \tag{2.11}$$

Here S_{obs} is the observed spectrum, S_{syn} is the synthetic spectrum which we derive from our current guess of where the spots are and v_i is the velocity of the pixel element in the spectrum. κ is the regularisation parameter that can be set by trial and error or using one of the many methods that are available and documented in Hansen (2010). R is the regularisation function. Goncharskii et al. (1977) used the standard Tikhonov regularisation function (Tikhonov, 1977). A common alternative regularisation function used is the maximum entropy function (Vogt et al., 1987).

A key to performing successful DI is for the spectra to have a high enough signal to noise ratio (SNR) in order to be able to see the bumps in the spectra above the noise. Often it is not possible to get individual high resolution spectra with a high enough SNR. In order to overcome this problem least squares deconvolution (LSD) has been used (see Section 2.7 for a description of LSD) to produce high SNR line profiles which can then be used as the input to DI (Collier Cameron et al., 2002b).

DI has successfully identified spots for hundreds of stars (Strassmeier, 2009) and

for all spectral types of cool stars which have convection.

2.6. Exoplanet characterisation with precision spectroscopy

Detection of an exoplanet is just the beginning. Once detected we can then move on and attempt to characterise it by determining some of its properties. These properties include the basic orbital properties of the planet with respect to its parent star and its basic physical properties e.g. mass, size and temperature. At a more detailed level of characterisation is determination of the likely structure of the planet e.g. the core, mantle, crust and atmosphere. In addition to this we can try to determine what these components of the planet are composed of and their physical properties. We now look at methods of characterisation which are applicable to transiting planets only and then those applicable to both transiting and non-transiting planets.

2.6.1. Methods for transiting planets

Exoplanet Densities

If a planet is detected by both the radial velocity and transit methods then more can be known about the planet. First as the orbital inclination and minimum mass is known we know the actual mass of the planet. In addition as the size of the planet and mass is now known the planet density can be determined and estimates of its composition can be made. It should be noted that with only a mass and radius measurement an exact interior composition cannot be inferred for an exoplanet because the problem is highly underconstrained. However, quantitative ranges of plausible compositions can be found (Rogers & Seager, 2010). Figure 2.14 shows the mass-radius diagram of planets whose masses and radii are known along with mass and radii of planets whose composition is primarily water, magnesium silicate and iron respectively.

Rossiter-McLaughlin effect

Transits can be observed using high resolution spectroscopy. Stars rotate. When the planet passes in front of the rotating star the light observed will be red shifted or blue shifted depending on whether the planet is obscuring light from the side of the planet rotating towards or away from the observer. This velocity shift is known as the Rossiter-McLaughlin (RM) effect and is named after the two astronomers

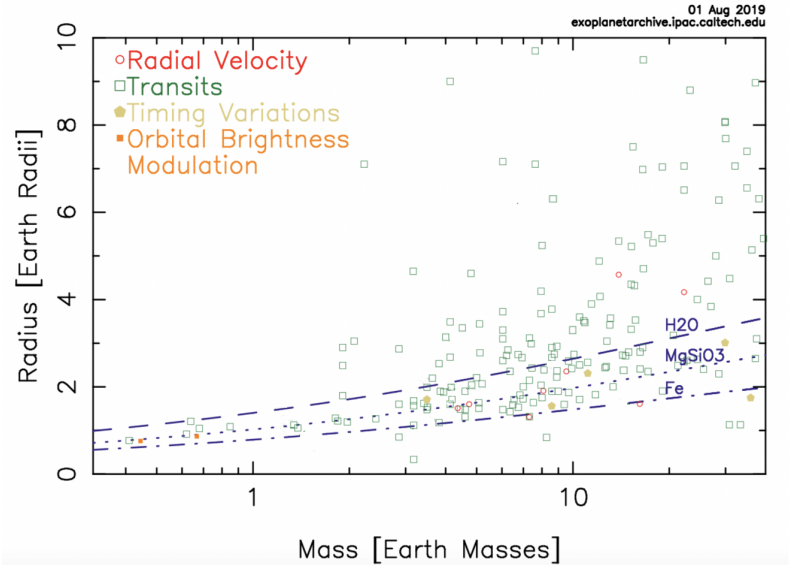

Figure 2.14.: Mass to radius relation for exoplanets less than 35 Earth masses whose mass and radius is known. Data extracted from the NASA Exoplanet Archive.

who discovered the effect for eclipsing binary stars (Rossiter (1924) and McLaughlin (1924)). The maximum semi-amplitude of this velocity shift in the case of a planet transiting an exoplanet is

$$\Delta A_{\mathrm{RM}} = \sqrt{1-b^2}\frac{R_p^2}{R_*^2} v_{eq} \sin I, \tag{2.12}$$

where b is the impact parameter of the planet (the closest projected distance in plane of sky between the planet and the centre of the star), $v_{eq} \sin I$ is the projected equatorial velocity at the surface of the star , R_* is the radius of the star and R_p is the radius of the planet (Winn, 2010). This effect is readily detectable for Jupiters orbiting solar like stars $\Delta A_{\mathrm{RM}} = 16$ ms^{-1} but is still out of reach for all spectroscopes bar ESPRESSO for an Earth orbiting a solar like star $\Delta A_{\mathrm{RM}} = 16$ cms^{-1}

In terms of further characterisation of the system spectroscopic analysis of the transit allows us to determine the projected rotation of the star (vsinI) and also λ the projected spin-orbit misalignment of the system (Figure 3.1). The misalignment angle can give insights into the systems dynamical history.

The first detection of the RM effect for an exoplanet transiting its parent star was for HD204958 (Queloz et al., 2000). The projected misalignment angle and projected equatorial velocity of the star were determined by comparing the velocities of the spectra to the velocities determined from a model.

Many observations of the RM effect have now been made and according to the TEPCAT database (Southworth, 2011) 226 measurements of the projected misalign-

ment angle have been made on 145 stars.

Instead of comparing velocities Collier Cameron et al. (2010) used a form of line tomography where they compared the CCFs from the spectra to model CCFs. Both the model CCFs for the star out of transit and the spectral line distortion (the bump) caused by the transit were modelled as Gaussians. A Markov Chain Monte Carlo analysis was performed to determine the projected misalignment angle and projected equatorial velocity

Cegla et al. (2016) also used the method of CCFs in the analysis of the Doppler effect for HD189733. CCFs were created for their time series of spectra. However in their case they assumed no specific shape for the CCF. A master CCF template representing the star out of transit (CCF_{out}) was created by combining a set of CCFs which were taken from spectra observed when the star was out of transit. The CCFs of the star in transit were then subtracted from the template to leave CCF residuals which contained the bump. The velocities of these CCF residuals which correspond to the velocity of the stellar surface behind the star were measured and then these velocities were fitted to their model. Their model identified differential rotation on the star which allowed them to determine the inclination of the rotation axis of the star.

Transmission spectrophotometry and spectroscopy

Further characterisation of transiting exoplanets has taken place using the techniques of transmission spectrophotometry and spectroscopy, often space based using *Hubble*, and through low and also high resolution spectroscopy from the ground.

In transmission spectrophotometry the flux from the star during a transit is captured using filters at several wavelength bandpasses (Charbonneau et al., 2002). Transmission spectroscopy captures the flux from the star during a transit using low or high resolution spectroscopy (Snellen et al., 2008). If the planet has an atmosphere then flux from the star arriving at the atmosphere may be absorbed or pass through it depending on the composition and properties of the atmosphere. The part of the atmosphere observed is at the day to night terminator of the planet. If the opacity of the atmosphere is different at the different wavelengths then the flux observed will be different and the apparent size of this planet will change.

The transmission flux is defined to be the ratio of the flux observed for the star in transit $F_{*,IT}$ to the flux observed for the star out of transit $F_{*,OOT}$ The transmission flux is wavelength dependent and is given by

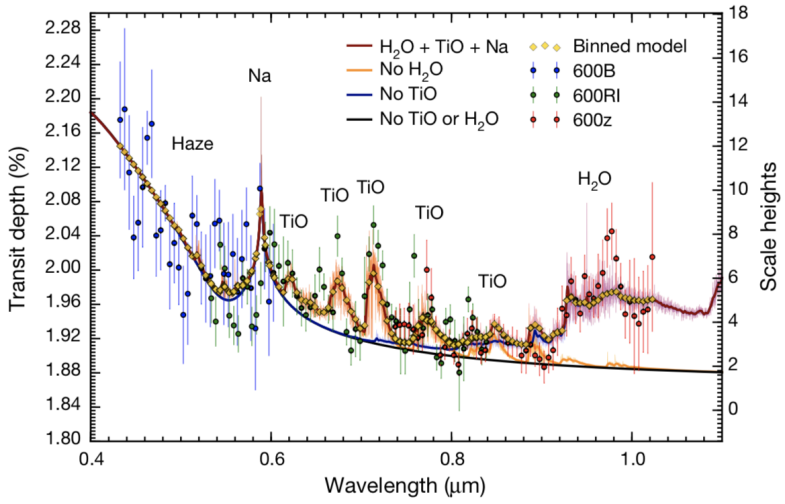

Figure 2.15.: Transmission spectrum of WASP-19b showing the identification of TiO molecules in the atmosphere of the planet (Sedaghati et al., 2017).

$$\frac{F_{*,IT}}{F_{*,OOT}} \approx \frac{2R_P A_H}{R_*^2}; \tag{2.13}$$

where R_P and R_* are the radius of the part of the star which is dark at all wavelengths and the radius of the star respectively. A_H is the additional radial extent of the planet atmosphere in units of R_P .

The transit depth normalised in units of the out of transit flux of the star is just one minus the transmission flux. The observational results showing changes in the transmission flux (or transit deptth) can then be fitted to models of planetary atmospheres in order to determine existence of molecules in the atmosphere and other physical properties of the atmosphere. Figure 2.15 shows a low resolution transmission spectrum of the hot Jupiter WASP-19b and identification of TiO molecules in the atmosphere of the planet (Sedaghati et al., 2017).

Successful characterisation of exoplanets using transmission spectroscopy of exoplanets is challenging due to the small changes in the size of the planet that are being measured. These changes are typically of the order of 10 to 100 ppm (parts per million) of that of the star. Also, if there are clouds in the atmosphere of the planet then they tend to flatten the transmission spectrum of the exoplanet causing properties of the atmosphere to be more difficult to detect. For example exoplanet GJ1412b has a flat transmission spectrum (Berta et al., 2012).

Further characterisation can be performed with analysis of the secondary transit. The secondary transit is where the planet goes behind the star with respect to the observer. When this occurs the flux observed reduces as light emitted from the

planet is blocked. During the secondary transit the flux reduces by the fraction (Seager, 2010)

$$\frac{F_p}{F_*} = \left(\frac{R_P}{R_*}^2\right)\frac{T_{eff,P}}{T_{eff,*}} \tag{2.14}$$

assuming the planet and star emit thermally as block bodies and we ignore starlight reflected from the planet. F_P and F_* are the fluxes from the planet and the star, R_P and R_* are the planet and stellar radii and $T_{eff,P}$ and $T_{eff,*}$ are the effective temperatures of the planet and star.

The Bond albedo A_B can then be determined fom the planet equilibrium equation

$$T_{eq,p} = T_{eff,*}\left(\frac{R_*}{a}\right)^{1/2}(1-A_B)^{1/4} \tag{2.15}$$

by equating the planet effectiive temperature with the equilibium temperature $T_{eq,p}$.

For a 2000 K hot Jupiter-size planet, the typical dip in flux during secondary transit is approximately 200 ppm at 2μm in the near-infrared and is readily detectable. Charbonneau et al. (2005) were able to estimate the Bond albedo (the fraction of incident flux from the star that is emitted by the planet) for the planet TrES-1 of 0.31 $\pm$ 0.14. Angerhausen et al. (2015) showed that in general the albedo of hot Jupiters (all less than 0.35) tend to be significantly lower than that of Jupiter which has an albedo of 0.52.

High resolution spectroscopy from the ground has also been used to characterise exoplanet atmospheres during transits and in particular can identify winds in the atmosphere and specific species of molecules. During the transit light from the star passes through the atmosphere of the planet and absorption lines of molecules in the atmosphere are imprinted on the starlight. The first molecule detected using this method was carbon monoxide for the the hot Jupiter HD209458b using the CRIRES near-infrared spectroscope on the VLT (Snellen et al., 2010). It was also found that there was a 2 km sec^{-1} blueshift of the carbon monoxide signal with respect to the systemic velocity of the host star suggesting the presence of a strong wind flowing from the irradiated dayside to the non-irradiated nightside of the planet.

2.6.2. Methods applicable to all planets

Properties and composition of the atmosphere of the exoplanet can also be determined for non-transiting planets using high resolution spectroscopy. Fig 2.16 shows how the flux of a solar like star changes according to wavelength along with the planets of our solar system and a putative spectrum of a hot Jupiter. In all the

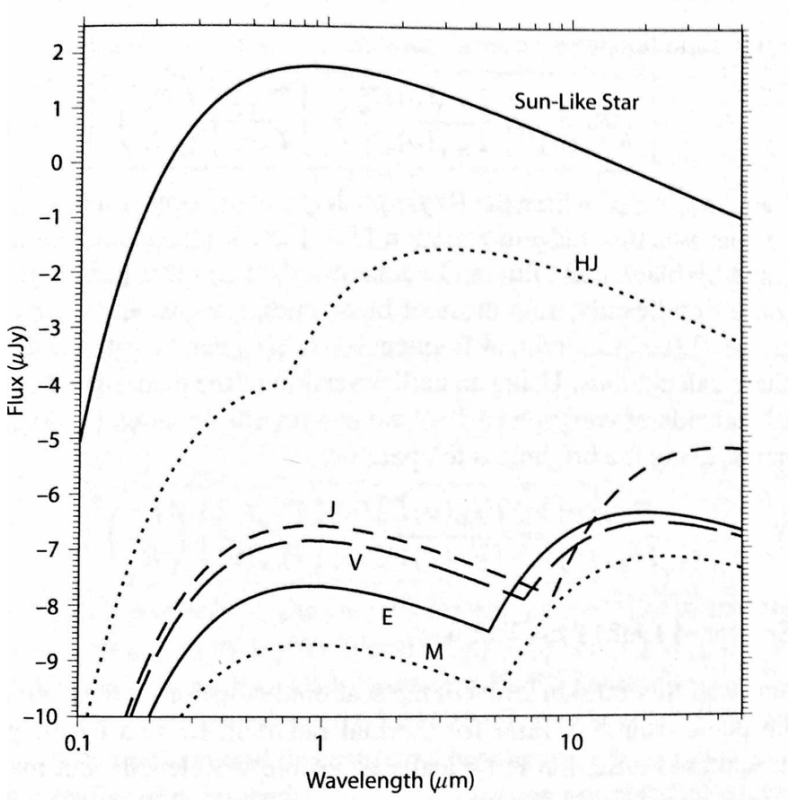

Figure 2.16.: Solar system blackbody thermal emission spectra and reflected light spectra at 10pc, for a Sun-like star, a putative hot Jupiter (HJ), Jupiter(J), Venus (V), Earth (E) and Mars (M). All the planetary spectra have two peaks: one in the optical where scattered starlight from the star peaks and the other in the near infra-red where the thermal emission from the planet dominates (Seager, 2010).

planets there are two peaks one in the near infra-red and the other in the optical. The infra-red peak corresponds to the maximum thermal emission from the planet and is depends on the effective temperature of the planet. The peak in the optical is where the light reflected from the planet is at a maximum and depends on the effective temperature of the star and the albedo and phase of the planet. Searches for molecules in the infra-red and for reflected light have been performed using ground based high resolution spectroscopy.

When dealing with distant exoplanets where the light from the star and planet cannot be spatially resolved our analysis of the spectroscopic observations has to be able to separate the light coming from the planet from the light from the star.

Emission

In the infra-red molecular lines from the planet spectrum can be separated from the stellar spectrum due to the large difference in RVs of the planet and the star. For a hot Jupiter, like 51 Peg b, the velocity semi amplitude of the planet is 133kms^{-1} compared to the velocity semi-amplitude of the star which is 55ms^{-1} (Birkby et al., 2017). Telluric contamination is removed and a template of the model spectrum of the molecule is then cross-correlated with each spectrum. The resulting cross-correlated spectra are then moved to the planet frame using a known or assumed inclination for the orbit of the planet and co-added to hopefully reveal a signal corresponding to the existence of the given molecule in the atmosphere. The detection of the molecule confirms the inclination of the planet and thus the mass of the planet can be determined. The first detections of a molecule in the atmosphere of a non-transiting planet was for CO in τ Boo b (Brogi et al., 2012) and (Rodler et al., 2012). According to the extrasolar planets encyclopaedia (Schneider, 2011) there are 20 non-transiting planets which have molecules detected for them. Some of these include CO and H_20 in 51 Peg b (Birkby et al., 2017), H_20 in τ Boo b (Lockwood et al., 2014), CO in β Pictoris b (Snellen et al., 2014), H_20 in HD 88133 b (Piskorz et al., 2016), H_20 and CO in GQ Lupi b (Schwarz et al., 2016)

Reflected Light

Before discussing the detection of reflected light using high resolution spectroscopy we look at evidence for reflected light in photometry. From observations using photometry we have a time series of measurements which can be phase folded into the orbital phase of the planet. From the phase folded data we can fit a curve to it, commonly called a light curve. These light curves as well as showing the transit if the planet transits also provide evidence for reflected light from the planet. Figure 2.17 shows the light curve for HAT-P-7b (Borucki et al., 2009). As the transiting planet orbits its parent star the light we receive from the planet varies according to the orbital phase of the planet. At time of transit (phase = 0) the planet has its non-illuminated side facing the observer and we have a minimum of flux in the curve. As the planet exits the transit light reflected from it in its crescent phase reaches us and the light in the phase curve increases until we get to the time just before secondary transit when we have effectively the whole hemisphere of the planet facing the observer illuminated. During secondary transit we have a dip due to the light from the planet being occluded from the observer by the star being in the line of sight. After the secondary transit the flux returns to the same level as immediately

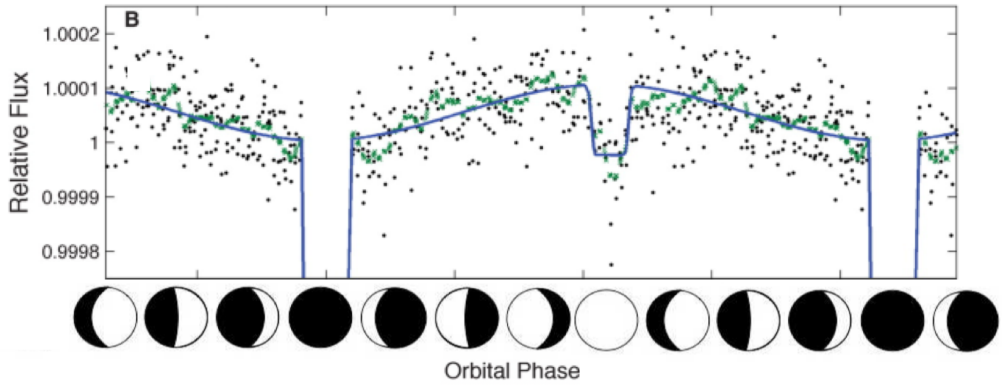

Figure 2.17.: Photometric light curve of HAT-P-7 b along with the phases of the planet adapted from Borucki et al. (2009).

before the transit and then gradually decreases as it goes from full to gibbous, to half (phase = 3/4) and then crescent until we reach the time of primary transit again.

As mentioned previously, ground based spectroscopy can also be used to detect reflected light. It is normally assumed that the spectrum of the reflected light is the same as that from the star. The light from the planet can be separated from that of the star due to the large difference in radial velocity between the planet and the star. The main difficulty with this technique is to overcome the small planet to star flux ratio which is of the order of a few parts in 10^{-5} for hot Jupiters. Successful detections of reflected light (Martins et al., 2015a) and (Borra & Deschatelets, 2018) have been claimed by creating a cross correlation function (CCF) or an autocorrelation function (ACF) for each spectrum. This has the effect of adding each of the spectral lines together to produce one high signal to noise spectral line for each spectrum (see Section 2.4.3). The CCFs and ACFs are moved into the frame of the star and are coadded to form a stellar template. This template is then subtracted from each of the CCFs (or (ACFs) to produce reesidual CCFs (or ACFs). These residuals are then shifted into the frame of the planet and are co-added and should contain the signal of the reflected light. The results for 51 Peg b give a consistent value for the velocity semi-amplitude of the planet as determined by the identification of molecules in the atmosphere and give a consistent value for the inclination as well.

2.7. Differential methods for high resolution spectroscopy

In this section I give an outline of differential methods for high resolution spectroscopy and give examples to where they can be applied to help determine properties of exoplanets and/or stars.

In astronomical high resolution spectroscopy we often have a time series of spectra which change over time due to some physical process relating to the star and/or planet e.g. Doppler shift due to orbit of star and planet around their barycentre, line profile distortion due to planet blocking light from the star during a transit.

Now we could compare spectra directly one element with the other but this is usually not practical as the SNR in each spectral element is so low that comparing them would just give us a noisy signal.

Traditionally the method to get around this problem would be to use a line list which represents the star or more accurately the position of the lines in the star and their amplitude. This line list would then be cross-correlated or used in a deconvolution operation with the individual spectra. There are a number of limitations with this method:

- The line list may not be accurate. Often line lists are derived from spectra of other stars with a similar spectral type thus there is bound to be inaccuracies. Sometimes the line lists are built from atomic and molecular line lists and these line lists are usually incomplete due to the huge number of molecular lines that there are in the spectrum of especially cooler stars.

- A lot of information is lost if we just use a line list to represent the star. We only have the position and amplitude of the lines of the spectrum of the star and no information is kept relating to the wings of the lines and any asymmetries in them.

- Blended lines are not catered for. This causes systematic errors in creating a line list from a stellar spectrum where blended lines may not be recognised. Systematic errors also occur in the cross-correlation or deconvolution process where blended portions of lines are erroneously double counted.

In order to overcome these limitations the differential method relies on building a high signal to noise stellar template which is made by combining the available spectra together. This template can then be used to search for differences with the individual spectra.

The stellar template relies on no line lists so does not suffer from any inaccuracies from it. It also has the advantage of using all the information from the stellar spectrum and not just line positions and line amplitudes. The problem with blended lines also disappears as the differential method does not involve any processes which try to identify individual lines.

I have developed a differential method of LSD (Donati et al., 1997) called differential Least Squares Deconvolution (dLSD). The original LSD relied on an atomic line list. In dLSD I use a high signal-to-noise template spectrum of the star. The stellar template I use comes from HARPS-TERRA which was described in Section 2.4.3.

In dLSD I compare this stellar template T(v) to a given spectrum of the star O(v) via a convolution operator * as follows

$$O(v) = T(v) * K(v), \tag{2.16}$$

where K(v) is the dLSD line profile also known as the kernel and v is velocity.

Figure 2.18 gives a simple example of how dLSD would work in the case of an exoplanet transit. The full details of the implementation of dLSD and how the deconvolution is performed is given in Chapter 3.

Application areas for dLSD in high resolution spectroscopy

From the overview of exoplanet science given earlier in this chapter it is clear that there are a number of areas where dLSD can be applied, namely where CCFs and LSD have already been applied. I now go through these in turn, identifying any research I have performed in the thesis in these areas.

- High resolution spectroscopy of transits and the Rossiter McLaughlin effect. In Section 2.6.1 I discussed previous work performed which determined the projected spin-orbit misalignment angle and the projected equatorial velocity from spectra of the star taken during a transit. Some of the methods included the use of CCFs to identify the distortion in the line profile from the light blocked by the planet. I have used dLSD instead of using CCFs and this research is reported in Chapter 3.

- Short term activity using Doppler imaging. In Section 2.5 I discussed previous work performed on Doppler imaging and how it produces a map of the surface of the star with features such as spots on it. One of the methods discussed in that section used LSD to produce high SNR line profiles to perform the

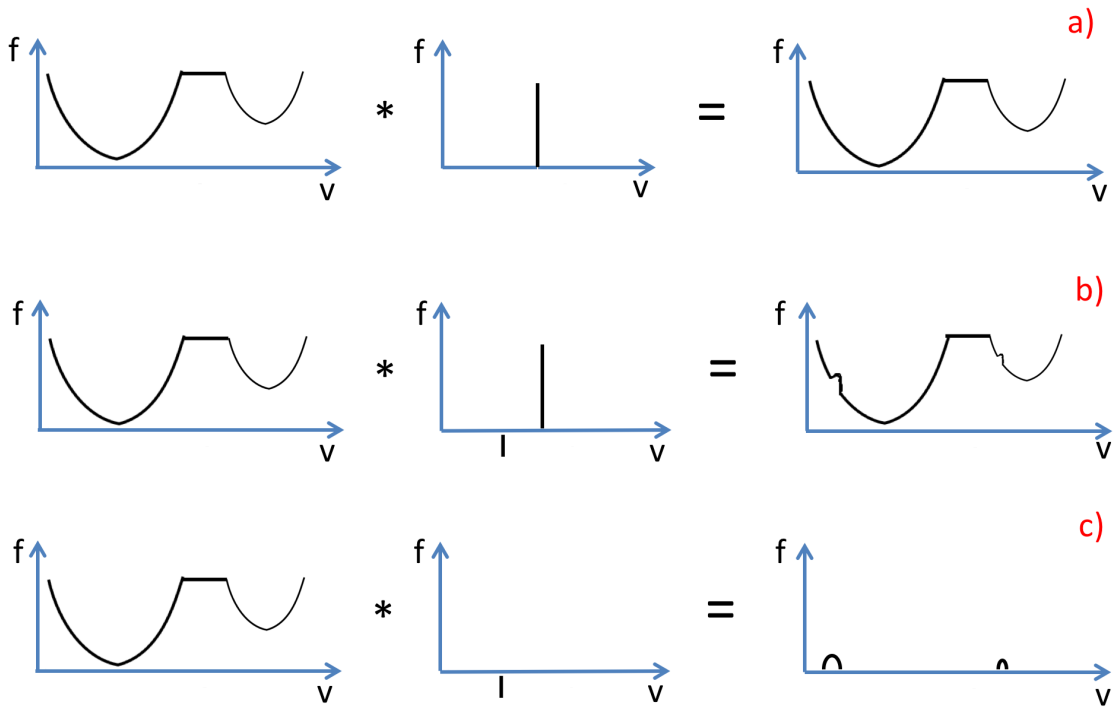

Figure 2.18.: Cartoon depicting dLSD. For all three tabs the left hand spectrum depicts the template, the right hand spectrum depicts the observation and the central spectrum depicts the dLSD spectral line profile. The * operator represents the convolution operator. Tab a) shows for an observation out of transit that the corresponding dLSD line profile is a delta function corresponding to the signal from the star. Tab b) shows for an observation in transit that the corresponding dLSD line profile has two delta functions corresponding to the star and the bump in the spectrum from the transit. In practice we remove the signal from the star with dLSD leaving the dLSD spectral line profile shown in tab c).

Doppler imaging on. I have used dLSD instead of LSD and developed my own version of Doppler imaging which permits me to produce a map of the spots on the surface of the star. I then use this information to determine the velocity shift caused by the spots and detrend these from the radial velocities measured for the star. The detrended velocities are then used to search for planets orbiting the star. This research is reported in Chapter 4.

- Detection of reflected light. In Section 2.6.2 I discussed methods to detect starlight reflected from an exoplanet. One of the methods discussed used CCF thus it is natural to assume that we could use dLSD in place of this. Instead of directly implementing this I became concerned with the level of broadening detected on the 51 Peg b (Martins et al., 2015a) reflected light CCF. I performed research examining the broadening and Doppler shifts that take place due to the starlight being reflected.. The result of this work is given in Chapter 5.

- Detection of molecules in the atmospheres of exoplanets. Methods to detect molecules in the atmosphere of the planet were discussed in Section 2.6. Where the molecule has a number of lines in the spectrum a cross-correlation is performed based on a line list. dLSD could be adapted and used instead of the cross-correlation.

3. Deconvolution method for high precision spectroscopy of stars and exoplanets I. Application to obliquity measurements of HARPS observations of HD189733b

This contents of this chapter are based on the paper Strachan & Anglada-Escudé (2017).

Abstract

High precision measurements of stellar spectroscopic line profiles and their changes over time contain very valuable information about the physics of the stellar photosphere (stellar activity) and can be used to characterize extrasolar planets via the Rossiter-McLaughlin effect or from reflected light from the planet.

In this paper we present a new method for measuring small changes in the mean line profile of a spectrum by performing what we call differential Least Squares Deconvolution (dLSD). The method consists in finding the convolution function (or kernel) required to transform a high signal-to-noise ratio template of the star into each observed spectrum. Compared to similar techniques, the method presented here does not require any assumptions on the template spectrum (e.g. no line-list or cross-correlation mask required).

We show that our implementation of dLSD is able to perform -at least- as good as other techniques by applying it to star-planet obliquity measurements of exoplanet HD183799 during its transit. Among other things, the method should enable model

independent detection of light reflected by an exoplanet.

3.1. Introduction

The Doppler detection method indirectly infers the existence of an exoplanet from the radial velocity (RV) shifts in the spectra of the parent star caused by the reflex motion of the star due to the gravitational pull on it from the exoplanet.

Several high resolution spectrometers used for Doppler velocity measurements such as HARPS (Pepe et al., 2000) operate in the visible wavelength range. More recently spectrometers such as CARMENES (Quirrenbach et al., 2010) have been built to operate in the near infra-red as well as the visible wavelength range and are in the process of carrying out radial velocity surveys on M dwarf stars in the solar neighbourhood.

If an exoplanet happens to transit its parent star then the Rossiter-McLaughlin (RM) effect, (Rossiter (1924) and McLaughlin (1924)) can be observed from high resolution spectra. The RM effect was initially observed in spectra of eclipsing binary stars. As the eclipsing star passed in front of the other rotating star the spectral lines were shifted due to asymmetry in blue shifted or red shifted light of the eclipsed star being blocked. The first RM effect observed for an exoplanet was observed over fifteen years ago for HD204958 (Bundy & Marcy (2000) and Queloz et al. (2000)).

The RM effect depends on the projected spin-orbit misalignment angle of the system and the projected rotational velocity of the star. The spin-orbit misalignment angle λ is the angle projected on the sky between the rotation axis of the star and the normal to the orbital plane of the transiting exoplanet. The angle $\beta = -\lambda$ has also been used to represent the misalignment angle (Triaud et al., 2009). Three different techniques have been used to determine these parameters for transiting exoplanet systems using high-resolution spectroscopy.

The first method relies on retrieving these parameters based on the radial velocity measurements e.g., Bundy & Marcy (2000), Queloz et al. (2000), Triaud et al. (2009) and (Albrecht et al., 2012). Systematic errors can occur in this method arising from the time-variable asymmetry of the stellar spectral lines during transit and solutions identified can be degenerate (Collier Cameron et al., 2010) however results from Triaud et al. (2009) were the same as by other methods.

Least Squares Deconvolution (LSD) was introduced by Donati et al. (1997) in order to detect magnetic fields in stars using spectropolarimetric observations. Ob-

serving the magnetic field signature in the spectropolarimetric observations was not possible to do directly due to the low signal to noise ratio (SNR) of the observation. LSD which involved deconvolving the observation with a template based on an atomic line list enabled the signal in each spectral line to be added and the resulting SNR to be increased by a factor of approximately the square route of the number of lines in an observation. The disadvantages with this technique is that the list of atomic lines in the template has to be complete and their weight have to be known.

Collier Cameron et al. (2010) introduced the use of the Cross Correlation Function (CCF) in order to track the shadow of the transiting exoplanet HD189733b as it passed across its parent star. The CCF is produced as described in Baranne et al. (1996) and Pepe et al. (2002) using a template for the spectral type of the star which has a set of box-shaped emission lines corresponding to the lines in the spectrum of the star. The template is then correlated with the spectrum for the star resulting in the CCF which is a single high SNR spectral line which can be fitted to a Gaussian. As the exoplanet passes in front of the star the bump corresponding to the light blocked by the exoplanet can be seen moving across the CCF. An alternative method using CCFs described in Cegla et al. (2016) has the advantage that it does not assume a particular Gaussian function for the CCF due to the subtraction of out and in-transit CCFs. Again disadvantages with these techniques include ensuring all lines are correctly identified in the template and also catering for blended lines both of which are problems for late type stars.

In order to cater for the limitations here of the above techniques a new method called differential Least Squares Deconvolution (dLSD) has been developed. Instead of building templates by identifying lines from atomic linelists or from the star itself this method uses a high SNR template which is just a combination of out of transit spectra from the star. The spectra chosen to build the template are from those that are out of transit A large enough sample are chosen so that signals from spots etc will be averaged out. The template comes from the one that is built by the HARPS-TERRA radial velocity tool. Anglada-Escudé & Butler (2012) contains a description of how this template is built as well as HARPS-TERRA.

The method consists in finding the convolution kernel that needs to match the template to the observation in a least squares sense. As the light blocked by the exoplanet as it passes in front of the star is to first order the same as the spectra of the star though, Doppler shifted and inverted, the Kernel function will contain a sharply peaked function representing the blocked light. The Kernel function can then be fitted to a forward model.

The fitting procedure consists of 1) generating the expected spectrum using the

template and a parameterized physical model, 2) applying the deconvolution procedure to generate a synthetic kernel, and 3) apply the same deconvolution procedure to the observed spectrum to generate the kernel of the observation and 4) compare the two using a Bayesian procedure. The parameterized physical model includes among other things a limb darkening function, planet-star radius ratio on the obliquity of the orbit and the impact parameter (distance in plane of sky of closest approach of the exoplanet to the centre of the parent star). In this paper, we will only assume two free parameters (projected spin-orbit misalignment angle λ and projected stellar rotational velocity $v_{eq}sini$) for simplicity because these are the only ones that cannot be determined with photometry.

We describe in Section 3.2 the details of the dLSD algorithm and the forward model used to retrieve the projected spin-orbit misalignment angle and projected rotational velocity parameters for a given system. In Section 3.3 we report on the performance of the dLSD algorithm based on test data and then for HARPS observations for HD189733. Finally the conclusions for the paper are given in Section 3.4.

3.2. Description of the dLSD algorithm

High resolution spectra from systems such as HARPS are first processed using the HARPS-TERRA software (Anglada-Escudé & Butler, 2012) and the option to remove the blaze from the spectra is selected. The HARPS-TERRA software creates a high signal to noise (SNR) template spectrum T and provides the observation spectra O which have been velocity shifted to take account of the earth's rotation and also the measured Doppler shift of the star.

Each spectrum is itself composed of a number of diffraction orders N. Thus for instance T = $\{T_1, T_2, .T_r, .., T_N\}$ where T_r represents the rth diffraction order.

The observations and template are interpolated using bicubic splines so that they have the same sampling and are moved to velocity space where v_i represents the velocity of the ith sampled element.

The spectra are processed order by order. For the rth order the residuals R_r to be fitted using least squares are obtained by subtracting the convolved spectrum C_r from the observation:

$$R_r(v_i) = O_r(v_i) - C_r(v_i), \tag{3.1}$$

where the convolved spectrum is the convolution of our kernel with the template:

$$C_r(v_i) = K_r * T_r(v_i). \tag{3.2}$$

In order to obtain K_r a deconvolution has to be performed. Firstly we approximate K_r to be a linear combination of n basis functions θ_j representing the signal due to the transiting exoplanet plus a Dirac delta function which represents the signal from the star:

$$K_r(v_i) \approx \sum_{j=1}^{n} \alpha_j \theta_j(v_i) + \delta(v_i), \tag{3.3}$$

where α_j are free parameters to be fitted. Top hat functions are used for the basis functions which have the property $\theta_j(v_i)$ is 1 when i=j and 0 otherwise.

We define a set of basis spectrum functions $b_j(v_i)$ to be the convolution of the jth basis function with the template:

$$b_j(v_i) = \theta_j * T_r(v_i) = \sum_{k=1}^{s} \theta_j(v_k) T_r(v_i - v_k), \tag{3.4}$$

where s is the number of velocity elements in the template.

The residuals can now be expressed in terms of the observation and template spectra and the spectrum basis functions as:

$$R_r(v_i) = O_r(v_i) - T_r(v_i) - \sum_{j=0}^{n} \alpha_j b_j(v_i). \tag{3.5}$$

Normally the number of velocity elements in the template (s) is significantly greater than the number of elements in the kernel (n) and we have an over-determined system which we fit using the least squares χ^2 method:

$$\chi^2(\alpha_0, ..., \alpha_{n-1}) = \sum_{i=1}^{s} \frac{R(v_i)^2}{\sigma_i^2}, \tag{3.6}$$

where σ_i is the error/weight for each velocity element. The weight we use assuming Poisson statistics is:

$$\sigma_i = \sqrt{T_r(v_i)}. \tag{3.7}$$

The template value is used as opposed to the observation value due to the template not containing outliers from noise and thus producing more reliable weight estimates.

To minimise the χ^2 we differentiate it with respect to each α_j and set the resulting terms equal to zero. Rearranging the resulting equations we get a set of n

simultaneous equations which in matrix form is:

$$AK_r = u, \tag{3.8}$$

where $K_r = \{\alpha_1, \alpha_2, ..., \alpha_n\}$ are our kernel coefficients and where each element in the n-column vector u is:

$$u[m] = \sum_{i=1}^{s} \frac{b_m(v_i)R_r(v_i)}{\sigma_i^2}, \tag{3.9}$$

and each element in the n×n matrix A is:

$$A[m][j] = \sum_{i=1}^{s} \frac{b_m(v_i)b_j(v_i)}{\sigma_i^2}, \tag{3.10}$$

Deconvolution is an example of a Fredholm integral equation of the first kind and the solution to these equations are well known to often be ill-conditioned (Groetsch, 2007). In addition our matrix A will be rank-deficient as we would expect that the majority of the elements in K will be effectively 0 (within the noise level). In order to deal with these issues we use Tikhonov regularisation (Tikhonov (1977)) where the solution to the set of simultaneous equations is taken to be the minimisation of the following functional composed of an accuracy term and a penalty term:

$$M(u, \kappa) = inf_{K_r \in F}\{||AK_r - u||^2 + \kappa||IK_r||^2\}, \tag{3.11}$$

where I is the identify matrix, F is the domain of K_r and κ is a free parameter commonly called the Tikhonov parameter expressing the relative weight of the penalty term to the accuracy term. The Tikhonov parameter has to be carefully chosen as picking a value too large will result in over-smoothing of the solution and if its too small then the noise will end up swamping the signal

There are several methods which can be used to select the value of the Tikhonov parameter including: Discrepancy principle, L-Curve criterion, General Cross Validation (GCV) and Normalized Cumulative Periodogram (NCP) (Hansen, 2010). An implementation of these methods is available in Regtools (Hansen, 1994) and were tested. The NCP was selected as it worked well and did not have the disadvantages inherent in the other methods. The Discrepancy Method required manual selection of a safety parameter and as such is not ideal to use for automated software. The choice of this parameter was also sensitive to the resulting value determined for the Tikhonov parameter. The L-Curve criterion resulted in a dramatic over-smoothed solution due to the cross-over between dominance of the accuracy term and penalty

term not being sharp. The GCV suffered from a known issue of sometimes under-smoothing the solution.

Once solutions for the kernel for all N differential orders of the residuals have been determined we then combine these kernels using a simple mean:

$$K(v_i) = \sum_{r=1}^{N} \frac{K_r(v_i)}{N}. \tag{3.12}$$

An additional detail to the algorithm was that a mask M(v_i) was used to identify velocity elements v_i which were to be included in the calculation of the χ^2 statistic (having value 1) or not (having value 0). The mask was initialised so all its elements had value 1. After calculating the residual spectrum R(v_i) in equation (3.1) clipping is performed to a user configurable level. All clipped velocity elements have their corresponding mask entry set to 0. In order to avoid problems with telluric contamination a telluric mask $T_M(v_i)$ was used and Doppler shifted to move it to the same frame as the observations. Any velocity elements v_i coinciding with the position of telluric lines in the mask had their entry in mask M(v_i) set to 0.

3.2.1. Forward model

Our aim is to determine whether the projected spin-orbit angle of the system is aligned or not and to determine the projected rotational velocity of the star. In order to do this these two parameters are free parameters in our forward model. The forward model uses these free parameters along with a number of system parameters derived from photometry to derive a model kernel. This model kernel can then be compared to the kernel obtained from the in transit observations in order to confirm the validity of the values of the free parameters used. The rest of this section describes how the forward model enables us to produce the model kernel. In order to keep the forward model as simple as possible (signal from ingress/egress greatly dependent on limb darkening and also signal not as strong due to only part of light from planet blocked) our model does not cover the time when the exoplanet is partially transiting the star - we only model from the time of second point of contact to the time of third point of contact during the transit.

We assume the star follows a standard quadratic limb darkening law:

$$I(\mu) = I(0)(1 - \epsilon_1(1 - \mu) - \epsilon_2(1 - \mu)^2), \tag{3.13}$$

where ϵ_1 and ϵ_2 are the limb darkening coefficients and μ is the cosine of the angle

between the direction of the centre of the star to the observer and the centre of the star to the transiting exoplanet. ϵ_1 and ϵ_2 are fixed value input parameters to our forward model.

Following Hartman et al. (2015) we take the spectrum of the star out of transit to be:

$$S_{ROOT}(v) = S * G(v), \tag{3.14}$$

where S is the spectrum of the star which has not been broadened due to the rotation of the star and G is the rotationally broadening profile of the star.

During the transit the spectrum of the star is given by:

$$S_{RIT}(v) = S * (G - D)(v) \tag{3.15}$$

where D represents the light (which is not rotationally broadened) blocked by the planet. Assuming quadratic limb darkening the analytical functions for G and D are given in the appendix of Hartman et al. (2015) and are not repeated here except to say that G = G(u,ϵ_1,ϵ_2) and D = D(u,ϵ_1,ϵ_2, x_p, y_p) where u is the relative velocity shift the broadening kernel is measured at and x_p, y_p is the current position of the planet in the plane of the sky.

The projected spin-orbit misalignment angle λ defined in Ohta et al. (2005), the angle between the angular momentum vector of the exoplanet and the axis of rotation vector of the star and the projected rotational velocity of the star v_{eq}sinI where v_{eq} is the equatorial velocity of the star and I is the inclination of the spin axis with respect to the observer are the two free parameters in our forward model.

Here we specify two forward models to determine x_p, y_p and u from the free parameters specified in the previous paragraph and a number of fixed parameters derived from observables.

For the first model we assume that we do not rely on the orbital parameters for the system. This can occur when only have old or partial radial velocity data for the orbit. In this case we rely on parameters derived from photometry including the second and third times of contact t_2 and t_3, the ratio of the exoplanet radius to that of the star R_P/R_* and impact parameter b. There are four points of contact with corresponding contact times in a transit. t_1 corresponds to first point of contact at start of ingress, t_2 is at end of ingress. Third point of contact occurs at time t_3 at start of egress and fourth point of contact t_4 at end of egress when the planet no longer occludes any light from the star. The impact parameter is the minimum distance in the plane of the sky from the exoplanet to the centre of the star in units

of stellar radius. For a transiting exoplanet b has a value between 0 and 1.

For this case we assume circular motion of the exoplanet is valid and the exoplanet moves across the star in a straight line at a constant velocity v_{planet}. The position of the exoplanet in the plane of the sky at any point in time is given by coordinate pair (x_p, y_p) as detailed in Figure 3.1 Both of the axis are scaled so that $R_* = 1$.

Given the assumptions above and values for the projected spin-orbit misalignment angle λ and impact parameter b the path of the planet across the star is on the line with $y_p = \mathrm{b}$. The distance between the second and third points of contact d in units of stellar radius (see Figure 3.2) is given by:

$$d = 2\sqrt{(1 - R_P/R_*)^2 - b^2}. \tag{3.16}$$

Providing we know the times of second and third point of contact t_2 and t_3 from observations then we have that the velocity of the planet is:

$$v_{planet} = \frac{d}{t_3 - t_2} = \frac{2\sqrt{(1 - R_P/R_*)^2 - b^2}}{t_3 - t_2}. \tag{3.17}$$

Thus the projected on the sky x-coordinate for the planet at time t is:

$$x_p(t) = v_{planet}(t - t_2) - \sqrt{(1 - R_P/R_*)^2 - b^2}. \tag{3.18}$$

The shortest distance from the spin axis to the planet s_p again scaled in units of R_* expressed in terms of x_p and y_p is using simple geometry from Figure 3.1 :

$$s_p(t) = x_p \cos\lambda - y_p \sin\lambda. \tag{3.19}$$

The Doppler shift velocity u is:

$$u(t) = s_p v_{eq} \sin I, \tag{3.20}$$

where v_{eq} is the observed equatorial rotation velocity of the planet and I is the angle the rotation axis is inclined with respect to the observer.

For the case of the forward model if the orbit of the planet is known then the on sky coordinates are given by:

$$x_p = r \sin(\nu + \omega - \pi/2), \tag{3.21}$$

$$y_p = r \cos(\nu + \omega - \pi/2) \cos i, \tag{3.22}$$

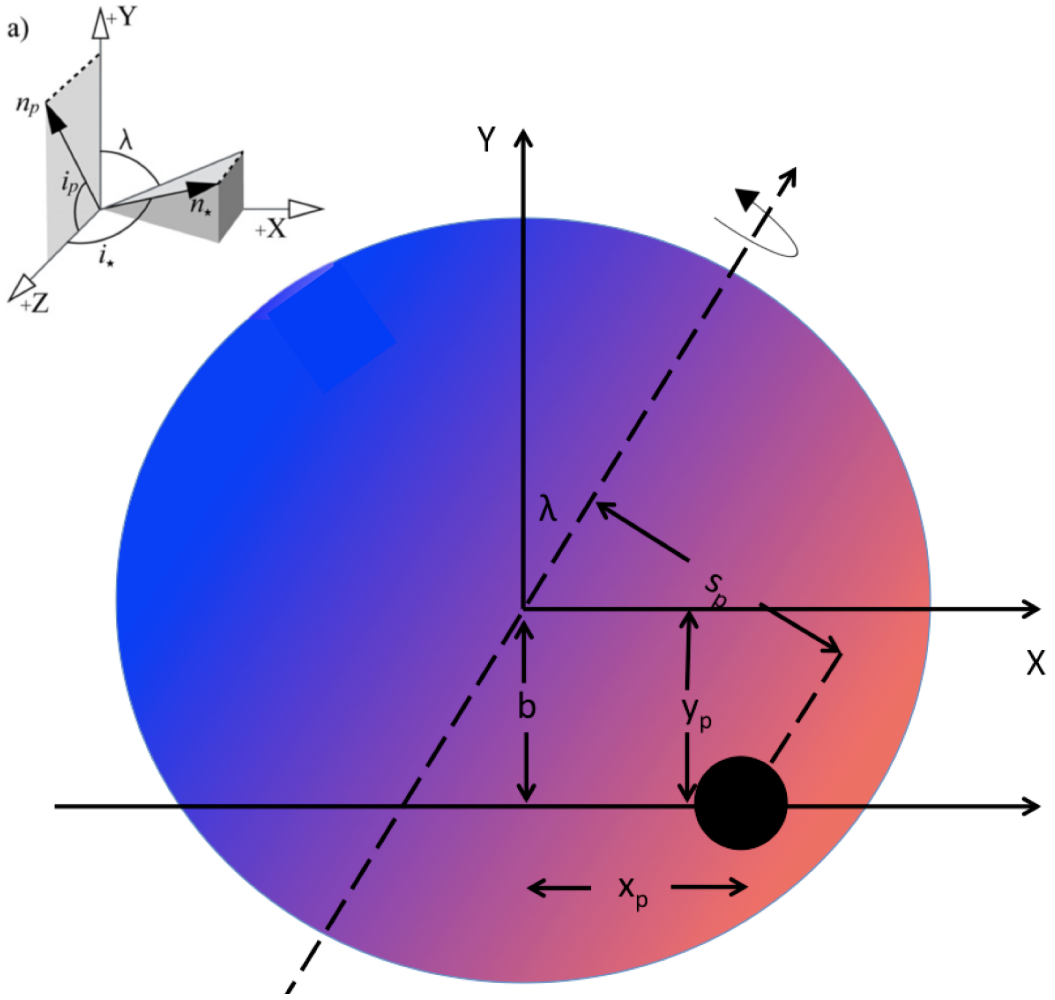

Figure 3.1.: Planet during transit in the plane of the sky showing the spin-orbit misalignment angle λ and impact parameter b. The path of the planet is also shown along with the axis used to locate the position (x_p, y_p) of the planet. Inset a) shows the projected obliquity in relation to the orbital inclination (i_p), stellar inclination (i_*), and the normals to the orbital plane (n_p) and stellar rotation (n_*).

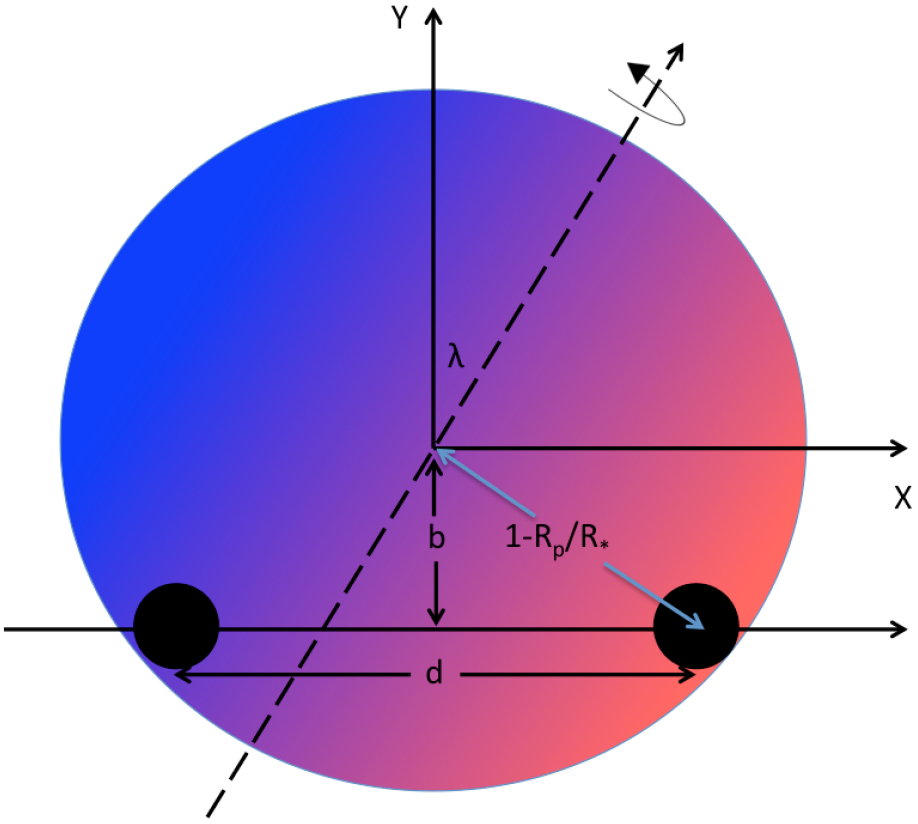

Figure 3.2.: Plane of sky showing position of planet transiting at second and third points of contact and the distance d between them.

where ν is the true anomaly, ω is the argument of pericentre and i is the inclination of the orbit to the line of sight of the observer. We can then use equations 3.19 and 3.20 to calculate the Doppler shift u.

For the purposes of the forward model we determine the non-rotationally broadened spectrum of the star S from equation 3.14 by deconvolving the high SNR template T we have for the star with the rotational broadening profile G:

$$S_{ROOT,r}(v) = T_r = S_r * G(v), \tag{3.23}$$

where the suffixes r are present as we perform the deconvolution order by order.

Having determined S_r we can then determine $S_{RIT,r}$(v) from equation 3.15 by performing a convolution for each order r:

$$S_{RIT,r}(v) = S_r * (G - D)(v), \tag{3.24}$$

We can now determine the forward model kernel profile M_r as specified in equation 3.11 using dLSD taking the template T_r in equation 3.1 as S_r and the observations O_r in equation 3.2 as $S_{RIT,r}$(v).

3.2.2. Bayesian model for parameter selection

Bayes equation is used to determine the posterior probability distributions $P(\theta|D)$ of the free parameters θ in the forward model based on the data D:

$$P(\theta|D) = \frac{P(D|\theta)P(\theta)}{P(D)} \propto P(D|\theta)P(\theta), \tag{3.25}$$

where $P(D|\theta)$ is the likelihood of the data given the parameters θ, P(θ) is the prior probability distribution of the free parameters and P(D) is the normalization constant which we do not calculate here as only the value proportional to P(θ|D) is required to be determined.

Running dLSD on the spectroscopic data and the forward model synthetic data results in two files to be compared. We have the processed data file (D) and the forward model file (M) which depends on the free parameters θ. Both files have the same format with each row containing a Kernel k calculated for one of the spectra. Each row contains several elements e which contains the value of the Kernel function at the velocity denoted by the element. Assuming Gaussian distributions for the uncertainties in the measurements the likelihood function L = P(D—θ) is given by:

$$L = \prod_{k=1}^{N} \prod_{e=1}^{n} \frac{1}{\sqrt{2\pi(\sigma_k^2 + \sigma_{ke}^2)}} exp\Big(- \frac{1}{2} \frac{(D[k,e] - M[k,e])^2}{\sigma_k^2 + \sigma_{ke}^2} \Big), \tag{3.26}$$

where N is the number of kernels, n is number of elements in a kernel, σ_k and σ_{ke} are the errors in the kernel and the kernel element respectively, and D[k,e] and M[k,e] correspond to the value of the eth element in the kth kernel for the data file and the model file respectively. In order to avoid correlations between kernel element the kernels were sampled at the resolution of the spectroscope which for HARPS is 2.5kms^{-1}. We tested that the noise in the kernel was Gaussian using test generated data samples with the Smirnof-Kolmogorov test.

We measured the noise for the kernel elements using the standard deviation of the kernel elements in the wings of the kernel where there is no signal.

There are two parameters in the model: the observed rotation velocity of the star v_{eq}sinI and the projected spin-orbit misalignment angle λ. We use flat priors for both of these parameters:

$$P(v_{eq}sinI) = \frac{1}{(v_{eq}sinI)_{max} - (v_{eq}sinI)_{min}}, \tag{3.27}$$

where $v_{eq}sinI \in \{(v_{eq}sinI)_{min}, ..., (v_{eq}sinI)_{max}\}$.

$$P(\lambda) = \frac{1}{4\pi},\ where \lambda \in \{-2\pi, ..., 2\pi\}, \tag{3.28}$$

and where $(v_{eq}sinI)_{min}$ and $(v_{eq}sinI)_{max}$ represents the extremes in the range of values for $v_{eq}sinI$ and depends on the star.

In practice logarithms of values are calculated numerically so from Bayes equation the posterior probability of the free parameters θ becomes:

$$lnP(\theta|D) \propto lnL + lnP(\theta), \tag{3.29}$$

where logarithm of the likelihood lnL is:

$$lnL = nNln\big(\frac{1}{\sqrt{2\pi}}\big) + \sum_{k=1}^{N} \sum_{e=1}^{n} ln\left(\frac{1}{\sqrt{(\sigma_k^2 + \sigma_{ke}^2)}} \right) - \sum_{k=1}^{N} \sum_{e=1}^{n} \frac{1}{2} \frac{(D[k,e] - M[k,e])^2}{(\sigma_k^2 + \sigma_{ke}^2)}. \tag{3.30}$$

Markov Chain Monte Carlo (MCMC) based on Metropolis-Hastings algorithm,

Metropolis et al. (1953) and Hastings (1970), is used to calculate the posterior probabilities. The chain is started using an initial set of free parameter values θ_0 and lnLP(θ_0) is calculated.

A trial set of parameter is then calculated:

$$\theta_{i+1} = \theta_i + step * \mathcal{N}(0,1), \tag{3.31}$$

where $\mathcal{N}$(0,1) is a Gaussian distribution with mean 0 and variance 1. The step number is adjusted so that 20% of the trial set of parameters are accepted. The trial set parameters are accepted if:

$$lnLP(\theta_{i+1}) - lnLP(\theta_i) > 0, \tag{3.32}$$

and if this condition is not met then the trial set of parameters can also be accepted if:

$$Random[0,1] < exp[lnLP(\theta_{i+1}) - lnLP(\theta_i)]. \tag{3.33}$$

The chains are normally allowed a burn in of 100 accepted proposals and are then allowed to run for 1000 accepted proposals.

3.3. Performance

3.3.1. Testing by injecting simulated data

Testing of the algorithm was carried out using out of transit data from HARPS high resolution spectroscopic data for HD189733. A high SNR template was created from the spectra captured the night of 8th of September 2006 and then the algorithm dLSD was run against seven out of transit spectra. The resulting kernels are shown in Figure 3.3 showing a signal comprising of black and white vertical bends around the 0 velocity point of the kernel and which eventually disappears away from it. As flux is conserved in convolution operations the scale for the values of the kernel are such that if we had a kernel with all elements 0 bar one element with value -0.1 then this would correspond to the signal caused by the transiting planet having exactly the same spectrum as that of the star out of transit but with -1/10th of the amplitude.

This signal could be due to a number or reasons including correction for the blaze not being accurate enough and high frequency components in the spectra causing the

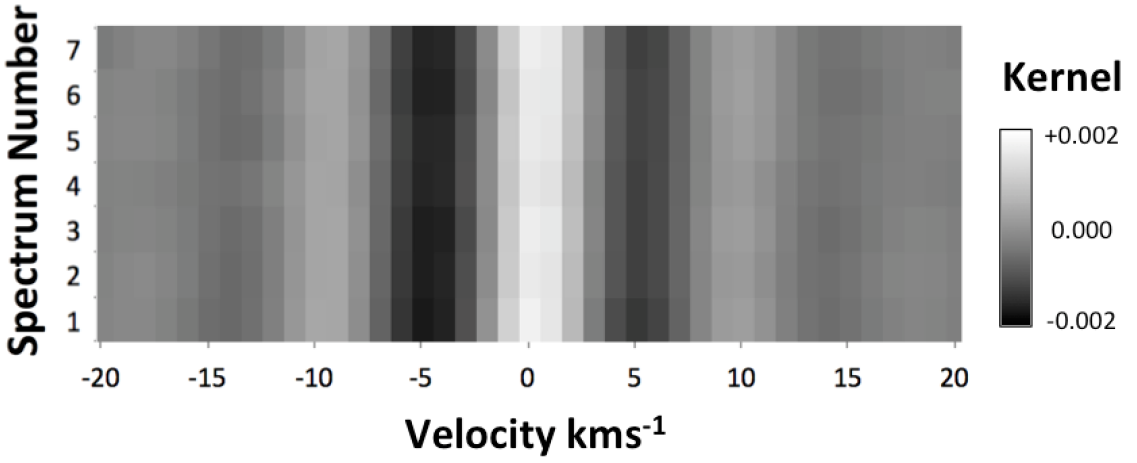

Figure 3.3.: Greyscale of kernel function for seven out of transit spectra for HD189733 showing vertical striped bands near to the central velocities of the kernel.

banding due to aliasing from the deconvolution. As the signal is constant across the different Kernels it can be removed by averaging and then subtracting the average from each Kernel.

The same seven spectra were used and then injected with a signal to simulate the effect of the planet transiting the star which took the form of adding a copy of the template spectrum whose amplitude was multiplied by a factor of -0.05 and whose velocity was shifted from -6 to +6 kms^{-1} in steps of 2 kms^{-1}. The kernels for the seven spectra are shown in Figure 3.4 and show clearly the synthetic signal for the transiting planet - the black diagonal line moving from left to right. In addition there is ringing. The ringing has maximum amplitude of approximately 16% of the amplitude of the main signal. The ringing is due to the Gibbs effect (Wilbraham (1848)) which is well known to be present with Tikhonov regularisation where the kernel function is discontinuous or has sharp edges. The maximum amplitude of the signal in the kernel has magnitude significantly less than -0.05. This is because the regularisation spreads out the signal in velocity space. If you integrate the signal across the velocity space then you recover the -0.05.

In the above the seven observation spectra were not normalised which will be the case for synthetic data. Normalizing these spectra gives the results for the kernel in Figure 3.5 where at mid-transit the signal is weaker and is stronger towards the start and end of the transit.

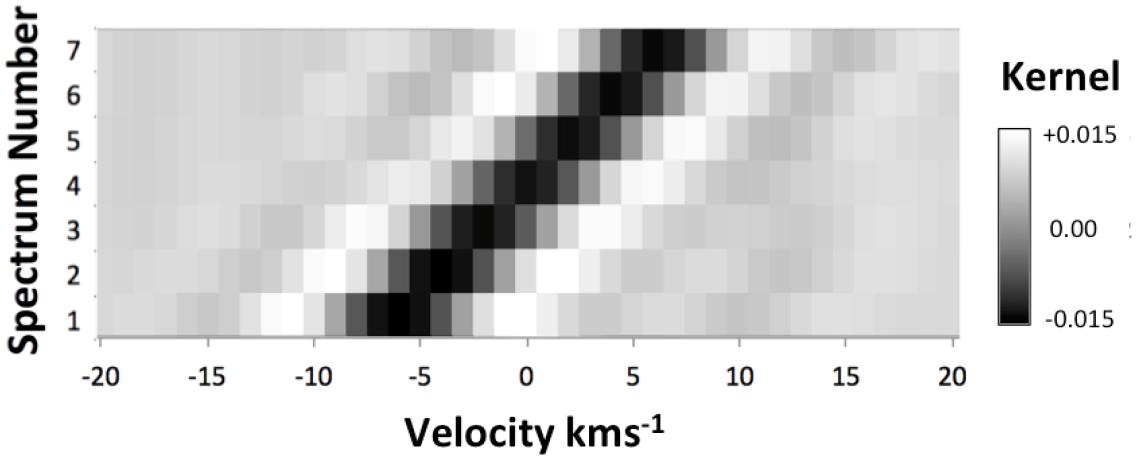

Figure 3.4.: Greyscale of kernel functions for seven out of transit spectra for HD189733 with injected signal from -6 to +6 kms^{-1} in steps of 2kms^{-1}. Black diagonal line shows the presence of the signal along with alternative white and black banding caused by Gibbs effect.

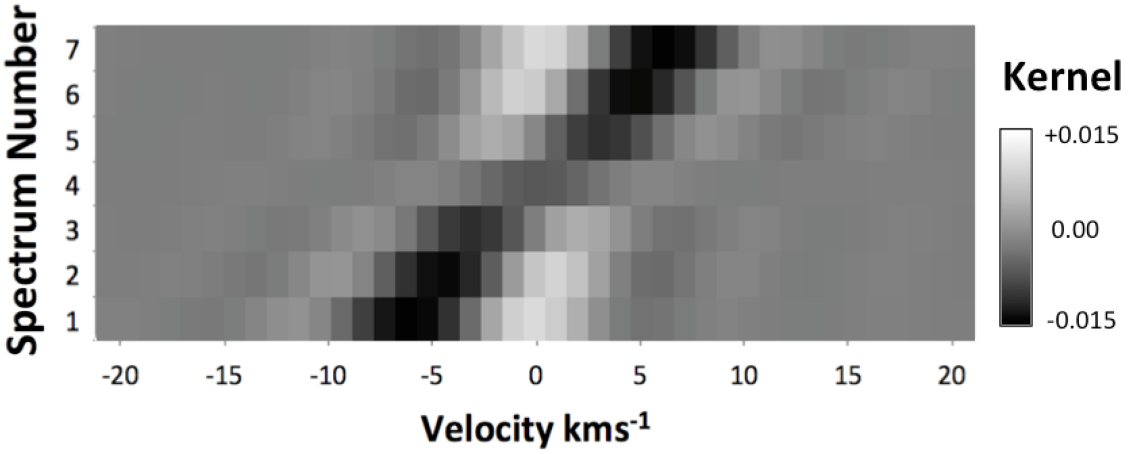

Figure 3.5.: Greyscale of kernel function for seven out of transit spectra for HD189733 with injected signal from -6 to +6 kms^{-1} in steps of 2kms^{-1} which has been normalised.

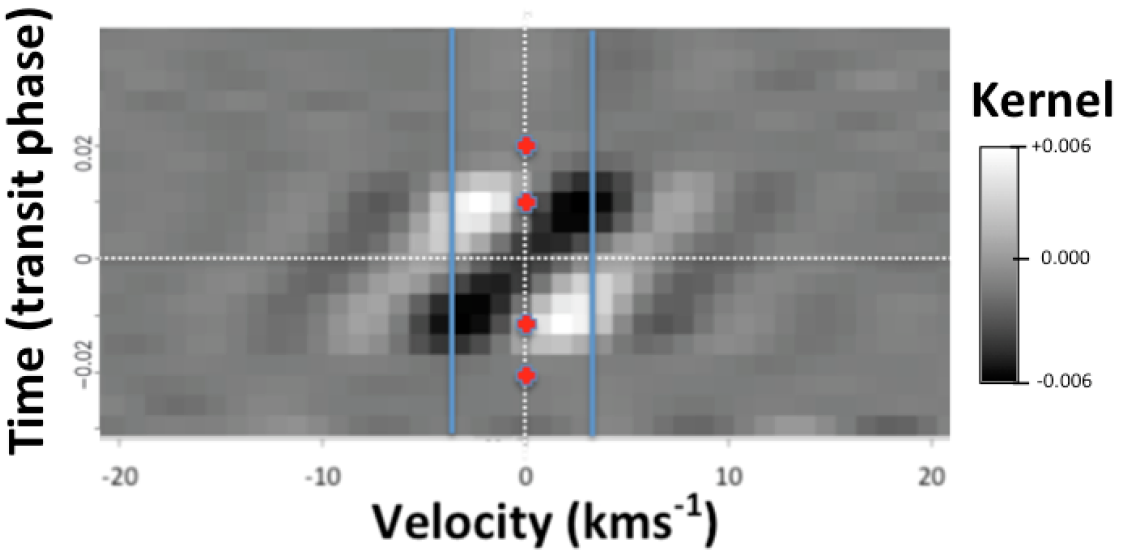

Figure 3.6.: Greyscale of kernel function for the 20 spectra of HD189733 on the night of 9th August 2006. The lines in blue represent v_{eq}sinI determined for the star and the red dots represent the four points of contact during the transit.

Table 3.1.: Parameters used from previous studies of HD189733b.

Parameter	Value	Units	Reference
T_C	2453988.80339	BJD	Triaud et al. (2009)
T_4 - T_1	1.827	hours	Winn et al. (2007)
T_2 - T_1	24.6	mins	Winn et al. (2007)
b	0.687	R_*	Triaud et al. (2009)
R_p/R_*	0.1581		Triaud et al. (2009)

3.3.2. HD189733b

HD189733b is a hot Jupiter transiting its parent star (Bouchy et al., 2005) and is one of the most studied exoplanets. High resolution spectra of HD189733 were obtained using HARPS (High Accuracy Radial velocity Planet Searcher) at the 3.6 metre telescope in La Silla, Chile over four nights: July 30th, August 4th and September 8th 2006, and August 29th 2007 under the allocated programme 079.C-0828(A). These spectra are publically available and were obtained by us from the ESO archive.

The spectra were processed using HARPS-TERRA and then the dLSD software and the kernel for the spectra for the night of August 4th 2006 are shown in Figure 3.6.

We used the simple forward model not relying on all the orbital parameters to determine the projected spin-orbit misalignment angle and rotation of the star. This was due to the radial velocities (RVs) available from HARPS not having good

Table 3.2.: Mean and one sigma errors for the fitted parameters for the 7th September 2006 HD189733 data for differing values of the limb darkening parameters ϵ.

Parameter	Value	Error	units
$\epsilon_1 = 0.7$, $\epsilon_2 = 0.0$			
λ	-0.374	0.475	degrees
$v_{eq}sinI$	2.988	0.015	kms^{-1}
$\epsilon_1 = 0.8$, $\epsilon_2 = 0.0$			
λ	-0.108	0.376	degrees
$v_{eq}sinI$	2.998	0.040	kms^{-1}
$\epsilon_2 = 0.9$, $\epsilon_2 = 0.0$			
λ	0.007	0.416	degrees
$v_{eq}sinI$	3.021	0.043	kms^{-1}
LDTK: $\epsilon_1 = 0.7676$, $\epsilon_2 = 0.0028$			
λ	-0.069	0.437	degrees
$v_{eq}sinI$	2.977	0.037	kms^{-1}

coverage of the complete orbit as the data came mainly from around the transit times.

HARPS-TERRA was used to derive the RVs from the HARPS data and a straight line was fitted to the out of transit measurements in order to determine the RVs of the star in transit.

The values we used for all the fixed parameters are detailed in Table 3.1 with references to the literature where the values came from. There were two main sources for the data. The paper from Triaud et al. (2009) who derived the parameters from both spectroscopic and photometric data. This paper had all the fixed parameters required for the forward model bar times for the second third and contacts. In order to obtain these times we took photometrically derived data from Winn et al. (2007).

In order to fit the model kernel to the kernel derived from the observations with our free parameters we use Markov Chain Monte Carlo (MCMC) with the Metropolis Hastings algorithm (Metropolis et al. (1953)) The standard χ^2 statistic was used to measure the fit. We allowed a burn of 100 accepted proposals before capturing a chain of 1000 accepted proposals. Several runs of the MCMC were carried out with different initial free parameter values to ensure that we had found the most likely solution. A correlation diagram for the probability distributions of the two free parameters λ and $v_{eq}sinI$ is shown in Figure 3.7. This figure shows no significant correlation between the parameters.

We produced chains for three different fixed values of the limb darkening parameter $\epsilon_1 = 0.7, 0.8$ and 0.9 with ϵ_2 held at 0 and the results are presented in Table 3.2. ϵ_1 and ϵ_2 were held fixed for each run due to correlations between it and the other

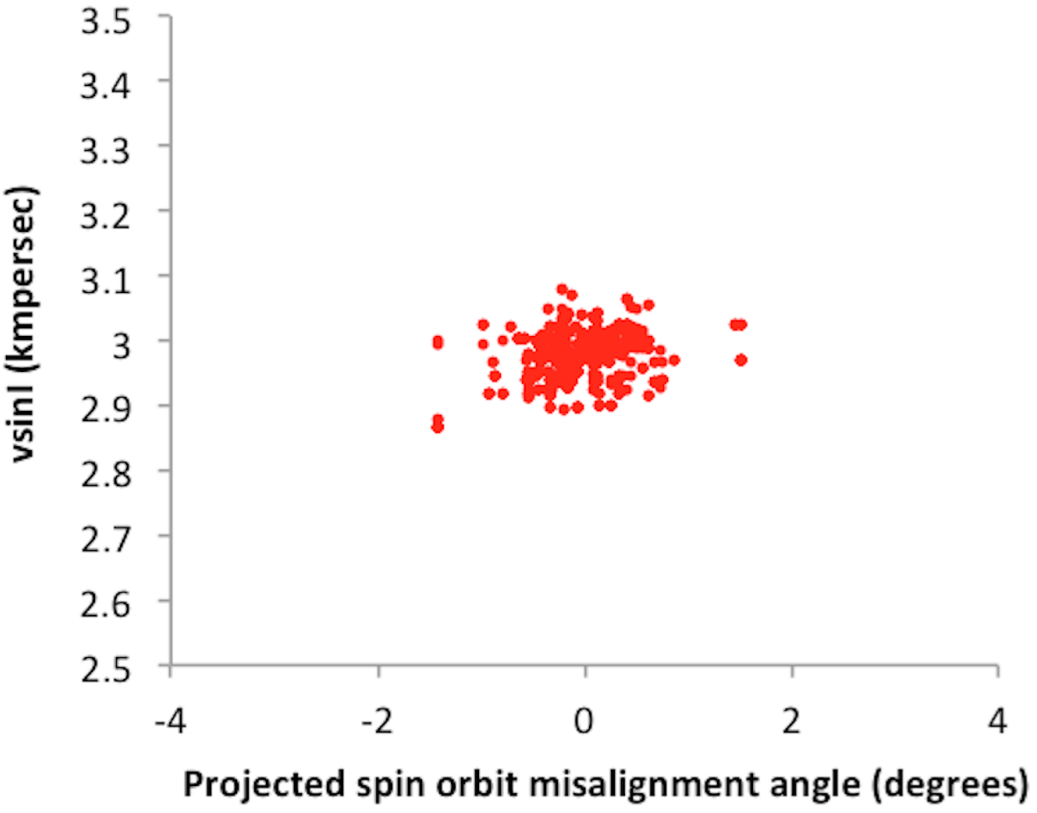

Figure 3.7.: Correlation diagram showing the probability distributions for the parameters λ and v_{eq}sinI for the transit of 8th September 2008 of HD189733.

free parameters (Collier Cameron et al., 2010). The results show a small amount of correlation between the limb darkening parameter. and the projected spin-orbit misalignment angle.

We also calculated quadratic limb darkening parameters using the Limb Darkening Toolkit (LDTK) (Parviainen & Aigrain, 2015) which uses the PHOENIX synthetic atmospheres and stellar spectra library (Husser et al., 2013). As inputs to the LDTK we used the HD189733 stellar parameters: effective temperature 4875 ± 43K, logg 4.56 ±0.03 and metallicity z = -0.03 ± 0.08 from Boyajian et al. (2015). The results of running dLSD against these limb darkening parameters are given in Table 3.2.

We also ran Markov chains where instead of processing the spectra produced from the forward model with dLSD and comparing it with the dLSD output from the observation spectra we just compared the observation spectra directly with spectra generated from the forward model. We used equation 3.30 for the comparison but now denoting D[k,e] as the flux at velocity element e of spectrum k and M[k,e] as the flux at velocity element e of spectrum k of the forward model. The values of the forward model M[k,e] come from S_{ROOT} and S_{RIT} in equations 3.23 and 3.24. The Markov chains did not converge due to the lack of signal to noise in the RM effect using this method.

3.4. Discussion and Conclusions

We have developed and implemented the dLSD technique. The spin-orbit misalignment we calculated is within one σ of perfect alignment and is not far from previous published results such as the work of Triaud et al. (2009) who calculated $\lambda = -0.87^{+0.32}_{-0.28}$ degrees and Cegla et al. (2016) who calculated $\lambda = -0.4 \pm 0.2$ degrees. The projected rotational velocity is in broad agreement with previous results whose values range from 2.9 to 3.2 kms^{-1} apart from one of the models in Triaud et al. (2009) which gave an over estimated vsinI of 3.32kms^{-1}.

The rotation period of the star carried out photometrically by Henry & Winn (2008) is 11.953± 0.009 days which if we assume the rotation angle is aligned with us gives sinI is 1 and using an average of the three values we obtained for v_{eq}sinI gives us a radius of 0.714$R_\odot$. This value is significantly smaller than the values calculated by Triaud et al. (2009) of R_*=0.766$\pm^{+0.007}_{-0.013} R_\odot$ and of the R_*=0.805±0.016$R_\odot$ value using interferometry from Boyajian et al. (2015). However the discrepancy may be due to the differential rotation of the star as explained in Collier Cameron et al. (2010).

Although the results for HD189733 are similar to other methods the advantage of the method should be seen for late type stars which have line blending.

One current drawback with the dLSD approach is the amount of computer time to perform the calculation in the forward model.

For the analysis of HD189733 to calculate one step in the MCMC chain takes 5 minutes on a laptop with a 2.3GHz I7 processor. This uses significantly more processing than other methods e.g. Triaud et al. (2009).

Given that only 20% of the steps are accepted the time taken to perform all the accepted steps including the burn in is just over 5 days. However there is significant room to decrease the time of the individual steps by introducing parallel processing into the algorithm so that each of the spectral orders could be processed separately.

In future work the authors expect to be able to draw quantitative comparisons between the different methods CCFs, LSD and dLSD discussed here for different types of stars.

In conclusion we have shown that we have been able to build the dLSD algorithm which can successfully be used to detect the path of an exoplanet as it transits its parent star using high resolution spectroscopy. In particular we have shown that the only template we need to use is one which is just built directly from the spectra of the star itself and from this we have been able to estimate the spin-orbit angle for the HD189733 system.

Acknowledgements

We are grateful to the HARPS team at Observatoire de Genéve, Observatoire de Haute-Provence, Laboratoire dAstrophysique de Marseille, Service 'Aéronomie du CNRS, Physikalisches Institut de Universitat Bern, ESO La Silla, and ESO Garching, who built and maintained the HARPS instrument, and were generous enough to make the data public.

4. A differential Least Squares Deconvolution method for high precision spectroscopy of stars and exoplanets II. Tracking and removing spot-induced activity on Ross 154

This contents of this chapter are based on the draft paper Strachan et al. (2020).

Abstract

We present the results of the Red Dots photometric and spectroscopic campaign along with CARMENES Guaranteed Time Observations and *Kepler* K2 archive photometry of the nearby M dwarf Ross 154. The main aims were to identify exoplanet candidates and to better understand activity on the star.

Periodogram analysis of the photometry from the campaign showed periodic behaviour between 2.85 and 2.87 days. In addition archive K2 photometry showed periodic data at half this period (the first harmonic). Periodograms of the radial velocity (RV) measurements derived from spectra from the campaign show three significant signals with periods of 1.43, 2.87 and 18.5 days with false alarm probability of less than 0.001%.

We used the differential Least Squares Deconvolution (dLSD) method which enables us to measure small changes in the line profile of spectra to analyse stellar activity. Periodic behaviour was found corresponding to the 2.87 day period and its first harmonic in the second and third moments of the dLSD profiles confirming these signals were due to activity on the star.

We fitted a spot forward model to the dLSD profiles assuming a stellar rotational period of 2.87 days. The best fit was for a large polar spot but we still observed significant periodic behaviour with RVs which had been detrended due to the effect of the spot. However a two spot (large polar spot and smaller lower latitude spot) fit using the rotational period from the K2 data gave a superior fit and any residual periodic behaviour from the detrended RVs was not found to be statistically significant.

4.1. Introduction

Since the first exoplanet orbiting a main sequence star 51 Peg (Mayor & Queloz, 1995) was detected there have been over 4000 confirmed exoplanet detections according to the Extrasolar Planet Encyclopedia (Schneider et al., 2011). The majority of exoplanets were detected using the transit method and are not in the local stellar neighbourhood (within 15 light years of the Sun).

The Red Dots campaign is the follow-up to the successful Pale Red Dot campaign which reported an exoplanet in the temperate zone of the Sun's closest stellar neighbour Proxima Centauri (Anglada-Escudé et al., 2016). The Red Dots Campaign comprised photometric and spectroscopic observations of three of the nearest M dwarf stars: Proxima Centauri, Barnard's star and Ross 154. The observing strategy, nightly spectroscopic observations over three months, was chosen to maximise the probability of identifying further exoplanet candidates in the temperate zone and to learn more about the activity of the stars. In particular Ross 154, a well known flaring, active M dwarf (Johns-Krull & Valenti (1996),Wargelin et al. (2008)) was selected to be observed in order to characterise the activity and to determine whether any planetary signals were present.

The CARMENES (Calar Alto high-Resolution search for M dwarfs with Exo-earths with Near-infrared and optical Echelle Spectrographs) survey of 300 M dwarfs (Quirrenbach et al., 2010) has been assigned 600 nights on the 3.5m telescope at the Calar Alto observatory in order to search for small terrestial exoplanets.

We report on the results of the analysis of the observations of Ross 154 (GJ 729, HIP92403) from the Red Dots campaign as well as the spectroscopic observations of Ross 154 from the CARMENES survey. Ross 154 was initially excluded from the CARMENES survey due to its declination being slightly less than the minimum declination in the star selection criteria for the survey (Alonso-Floriano et al., 2015). However it was reinstated so that a direct comparison could be made between the

CARMENES and Red Dots spectroscopic observations.

Ross 154 is the 7th nearest star system to the Earth and a brief summary of the previously known properties of the star from the literature are given in Section 4.2. In Section 4.3 we report on the photometric and spectroscopic observations from the Red Dots campaign and CARMENES survey. We also report on the *Kepler* K2 historic photometric observations which have been used in our analysis. In Section 4.4 we give the results of time series analysis of the photometric data and from the activity indices, radial velocities and dLSD line profiles which have been derived from the spectroscopic data.

In Section 4.5 we give the results of modelling of spots on Ross 154 using dLSD analysis of the spectra (Strachan & Anglada-Escudé, 2017). High precision measurements of stellar spectroscopic line profiles and their changes over time contain very valuable information about the physics of the stellar photosphere (stellar activity). The dLSD method consists in finding the convolution function (the dLSD line profile) required to transform a high signal-to-noise ratio template of the star into each observed spectrum. The time series of these dLSD line profiles are capable of showing active regions of the star e.g. (spots) moving across the surface of the star. We report on the results of a fit of a spot forward model to the dLSD line profile in order to estimate their size and location on the star. From the fitted spots we are able to determine the radial velocity shifts that they would generate on the star and also the expected shape of the stellar photometry phase curves. We report on the results of these fits here and in particular on the results of a periodogram analysis of the detrended RVs where the RV signals due to the spot forward model have been removed from the measured RVs of the spectra. If statistically significant signals are still present in the detrended RVs then this may indicate the presence of exoplanet candidates.

In Section 4.6 we provide a brief summary and discussion of the results and present some conclusions.

In Appendix A.1 we detail the forward model we use to model spots on the star and Appendix A.2 contains the data tables referred to in the body of the paper.

4.2. Ross 154

Ross 154 (GJ729, HIP92403, J18498-238) is a type M3.5Ve (Davison et al., 2015) star where e in the classification stands for Hα observed in emission. It resides in the solar neighbourhood at a distance of 2.9751 $\pm$ 0.0006 parsecs (Gaia Collab-

Table 4.1.: Stellar properties of Ross 154.

Stellar Parameters	Values	Reference
Spectral Type	M3.5Ve	Davison et al. (2015)
V[mag]	10.495	Koen et al. (2010)
Distance	2.97 parsecs	Gaia Collaboration (2018)
$M_*/M_\odot$	0.28	Reiners et al. (2018)
$R_*/R_\odot$	0.284	Reiners et al. (2018)
Effective Temperature	3548K	Maldonado et al. (2015)
vsini	$3 kms^{-1}$	Reiners et al. (2018)
Rotational Period	2.87 days	Kiraga & Stepien (2007)
inclination	37^o	Reiners et al. (2018)

oration, 2018), magnitude V=10.495 (Koen et al., 2010) and mass $0.28 M_\odot$. The properties of the star are given in Table 4.1. No evidence exists in the literature for companions to Ross 154. In particular the M dwarfs in Multiples (MINMS) survey (Ward-Duong et al., 2015) which analysed infrared adaptive optics (AO) data from the Very Large Telescope, Subaru Telescope, Canada-France-Hawaii Telescope, and MMT Observatory in order to detect close companions at 1 to 100 au and digitized wide-field archival plates to detect wide companions at 100 to 10 000 au found no companions.

Doppler broadening due to rotation for this star has been reported with a vsini of 3 ± 1.5 kms^{-1} (Reiners et al., 2018) and photometric data gives a relatively fast photometric rotation period for the star of 2.87 days (Kiraga & Stepien, 2007). An inclination i of the star is recorded as 37 ± 18 degrees (Reiners et al., 2018). This gives an estimated equatorial velocity for the star of $5 kms^{-1}$. Due to the relatively fast rotation of the star its age is estimated to be less than 1 Gyr (Wargelin et al., 2008).

Significant X-ray flares having been observed with Chandra with luminosity L_X =1.8x10^{30} ergs s^{-1} which is more than 100 times the quiescent bolometric X-ray luminosity $L_X = 6 \times 10^{27}$ergs s^{-1} (Wargelin et al., 2008). The flares also have a visible component and during the photometric observations of the campaign a very significant flare which resulted in a V band magnitude increase of 0.84 was observed.

Additional activity indicators derived from the spectrum for the star also provide evidence of its activity. The Hα line for the star is in emission and its activity indicator Log $L_{H\alpha}/L_{bol}$ has value -3.99 (Reiners et al., 2018) and chromospheric activity in the Calcium H and K lines gives a log(R'$_{HK}$) index of -4.428 (Astudillo-Defru et al., 2017a).

In addition to the 2.87 day rotational period, the photometric analysis of the

all sky survey ASAS (Pojmanski, 1997) has revealed two long term superimposed cycles. One of 7.1 ± 0.1 yr and a shorter cycle of 2.1 ± 0.1 yr (Suárez Mascareño et al., 2016).

Measurements of the magnetic field on the surface of the star have been carried out by Johns-Krull & Valenti (1996) using the Zeeman broadening on the Fe I line at 8468.4Å. They determined that 50 ±13% of the photosphere is covered by 2.6 ± 0.3kG fields which is about twice as strong as the magnetic fields measured in G and K stars. Reiners & Basri (2007) measured a slightly smaller magnetic flux of 2.2 ± 0.1kG which was in the intermediate class of magnetic flux strengths for the M dwarfs using a linear interpolation method between spectral features of two reference stars whose magnetic field strengths were known.

Shulyak et al. (2014) measured the magnetic field using the FeH lines and found for both their radial dominant (RC) and meridional (MC) dominant models that the magnetic field is made up of three components. For the RC model the field strengths for the three components are weak 1-1.5 kG, moderate 2.5-3 kG, and strong 5.5 kG intensities. For the MC model there is a strong (filling factor f =0.4) zero component as well as a 2kG component of similar strength (filling factor). The mean magnetic fields for the two models are 2.3 kG and 2.1 kG respectively.

In all the studies active regions (spots) are expected with large filling factors.

4.3. Data

Both photometric and spectroscopic data was used for the analysis.

Photometric data from the Red Dots campaign originated from three main sources. The Astrograph for the South Hemisphere II (ASH2) telescope (Pojmański, 2004) which captured data with R and V photometric filters and the Hα, O3 and S2 narrow band filters. The Las Cumbres Observatory Global Telescope (LCOGT) network with the 0.4-m telescopes located in Siding Spring Observatory Australia and the Haleakala Observatory, Hawaii and captured data in Johnson B, V band and I band filters. The American Association of Variable Star Observers (AAVSO) had eight observers based in USA, Belgium, Australia and Spain providing observations. Their data is publicly available at the AAVSO website (https://www.aavso.org).

In addition to the photometry from the Red Dots campaign, historical data was also used in the analysis. Four thousand and forty-three publicly available *Kepler* K2 photometric observations of Ross 154 from 4th October to 24th December 2015 were downloaded from the Mikulski Archive for Space Telescopes (MAST) (Vanderburg

& Johnson, 2014).

Spectroscopic data from two high resolution spectroscopes: the High Accuracy Radial velocity Planet Searcher - HARPS (Pepe et al., 2000) and CARMENES (Quirrenbach et al., 2010) were obtained during the Red Dots campaign.

The HARPS spectroscope is at the 3.6 metre telescope at La Silla, Chile. The spectroscope has a resolution of 120,000 in the wavelength range 380 to 680 nm. The HARPS spectra were extracted and calibrated with the standard ESO Data Reduction Software, and radial velocities were calculated using the HARPS-TERRA software (Anglada-Escudé & Butler, 2012). Sixty-nine spectra were captured between 13 July 2017 and 8 Oct 2018 one of which was not processed due to its short integration time (118 seconds). The remaining sixty-eight spectra had an integration time of 15 minutes and an average signal to noise ratio (SNR) of 39 at order 50 and 48 at the longest wavelength order 72. The median RV precision of the HARPS spectra are $\sigma_{HARPS,RD} = 2.2\text{ms}^{-1}$.

The CARMENES spectroscope is at the 3.5 metre telescope at the Centro Astronómico Hispano-Alemán de Calar Alto (CAHA, Almería, Spain). We analyzed data from the CARMENES VIS channel. The CARMENES instrument consists of two channels: the VIS channel obtains spectra at a resolution of R = 94,600 in the wavelength range 520 to 960 nm and the NIR channel yields spectra of R = 80,400 covering 960 to 1710 nm. Thirty-seven spectra were captured between 17th July 2017 and 6th October 2017. All CARMENES spectra were extracted using CARACEL (Caballero et al., 2016) and radial velocities calculated using SERVAL (Zechmeister et al., 2018). In the VIS channel there are 42 orders with middle order 21 having an average SNR of 66. The median RV precision of the CARMENES VIS channel spectra are $\sigma_{VIS} = 2.9\text{ms}^{-1}$. Due to the low median RV precision of $\sigma_{NIR} = 11.7\text{ms}^{-1}$ in the CARMENES NIR channel the NIR spectra were not included in the analysis.

Tables containing the radial velocities derived from all the spectra are given in Appendix A.2.

4.4. Time Series Analysis

4.4.1. Data analysis tools & model

We are mostly interested in detecting variability related to rotation, planets and/or activity cycles. In the case of radial velocity Doppler measurements, the signals can be interpreted as planets or other things. For simplicity in all the discussions,

we refer to a signal as something that is approximately well described by a single function like:

$$s(t; A, B, \nu) = A \sin(2\pi\nu t) + B \cos(2\pi\nu t) \tag{4.1}$$

where t is the time (independent variable), and the free parameters of the model are : ν (frequency of the signal in days^{-1}, and equal to 1/Period), and A and B are the amplitudes of the sin and cos terms in the signal (the semi-amplitude would be $K = \sqrt{A^2 + B^2}$).

As a general rule we model series or collection of time series as

$$m(t, set) = \gamma_{set} + \sum_n s_n(t, A_n, B_n, \nu_n) \tag{4.2}$$

Where γ_{set} depends on each instrument (can be different zero-point radial velocity in each spectrograph, or offset in different photometric instruments or systems) and n is the number of signals. Deciding whether there is a new periodic signal then consist on testing uniformly sampled frequencies between 0 to 2 days^{-1} (infinite period, to 0.5 day periods) and plotting the test frequency (x axis) against the improvement in the log-likelihood statistic (y axis). We call these plots log-likelihood periodograms (or simply periodograms hereafter), and they can then be used to estimate the statistical significance of each signal (so called p-value or false alarm probability) using the recipes given in Baluev (2009) and Baluev (2013). Once a signal is found, we include that signal in the new model and perform the search again optimizing all the free parameters of the model at the signal search level. We stop the search when there is nothing left with a false alarm probability under 0.1%. In usual planet searches, $s(t)$ would include a fully Keplerian model, but we don't use these models in our analyses here as we are mostly interested in identifying periodicities and possible harmonics (i.e. equivalent to obtaining a Fourier transform but for unevenly sampled data).

4.4.2. Radial Velocity Analysis

RVs derived from the available CARMENES and HARPS spectra from the Red Dots campaign were searched for potential planetary signals on circular orbits using recursive Log-likelihood periodograms (Anglada-Escudé et al., 2013). Three significant signals were identified with False Alarm Probability less than 0.001%. The

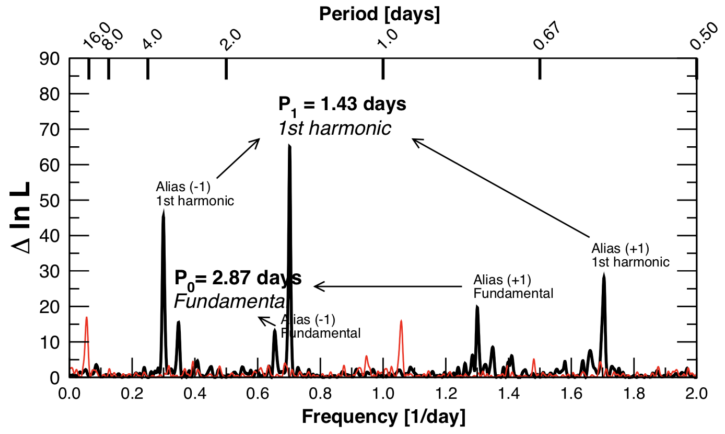

Figure 4.1.: First periodogram search of the combined radial velocity measurements of CARMENES and HARPS is shown in black. The rotation period found in the photometry and its first harmonic show prominently, with their corresponding aliases. The aliases are found at +/- integer times the frequency of the sampling cadence (1 day^{-1}), which is what is indicated in parenthesis. The third periodogram is also shown in red with the signals from the fundamental and first harmonic removed. The strongest signal here is the 18.5 day signal.

periodogram is presented in Figure 4.1 (only the periodogram for the first signal is shown for brevity). The first two correspond to the suspected rotation period at $\sim$ 2.87 days (fundamental period hereafter) and its first harmonic at $\sim$1.43 days (at half the fundamental period). As will be amply discussed later, these are rotation related signals. The third signal has a period of 18.5 days. The properties of these three signals are given in Table 4.2 including the Period, amplitude and increase in log-likelihood of detection of each one.

Concerning the first two signals, Boisse et al. (2011) reported that activity due to spots lead to signals in periodograms at the rotation period and its harmonics. The third significant signal at 18.5 days is not a harmonic of the photometric rotational period (although it is close to an alias of the third harmonic of the rotation period) and does not have a corresponding peak in the window function so could potentially be a planet. We will look into this possibility further in Section 4.5.2. In the following subsections, we will perform the standard diagnostics on additional indicators that are often applied to planet searches so the current dataset is understood on the same grounds as other putative planet candidates, and then build-on more detailed techniques to try to disentangle (or 'clean' true Doppler signals from the activity induced ones).

Table 4.2.: The three significant signals (FAP<0.1%) identified from the recursive log-likelihood periodogram for the CARMENES and HARPS radial velocity measurements including the improvement in log-likelihood Δ ln L, the period P, and the amplitude of each signal.

n	Δln L	P(days)	Ampl.(ms^{-1})
1	66.5	1.43	15.68
2	82.05	2.87	10.72
3	16.92	18.5	4.12

Table 4.3.: Summary of photometric observations.

Observatory	Band	No of Obs	Data Location
Kepler K2		3931	https://archive.stsci.edu/kepler/
AAVSO	V	12096	https://www.aavso.org/data-download
ASH2	Ha	210	request from author
ASH2	O3	197	request from author
ASH2	S2	200	request from author
ASH2	R	3801	request from author
ASH2	V	3844	request from author
LCOGT	B	1142	request from author
LCOGT	V	4471	request from author

4.4.3. Photometric Analysis

All photometric datasets were first sigma clipped to remove outliers. For the Red Dots data sets, this was done by first estimating the standard deviation of each time series taking the 80% central percentile, and removing points deviating 5 times more than this standard deviation. All the time series were then revised by eye and some obviously anomalous data-points where removed by hand. For the K2 set, the photon noise is so small that the variance of the data is dominated by intrinsic rotation (See fig. 4.2). In this case we applied 3-sigma clip procedure, which removed most deviant points.

All the photometric data sets from the Red Dots Campaign were binned into 0.1 day bins. These include AAVSO, ASH2 and LCO. For this analysis the non-simultaneously obtained K2 data was binned to 0.2 day intervals to reduce the amount of datapoints ($\sim$4000) to something more manageable (400). This bin size also smoothes out variability caused by flares, which is omnipresent throughout the K2 observation season (4-5 flares per day causing a maximum increase of flux on the star between 1% and 5%). The photometric measurements are briefly summarized in Table 4.3.

The periodogram searches for the first signal in all the combined Red Dots photometric sets, and the K2 set are shown in Figure 4.2. Because the K2 data is sampled

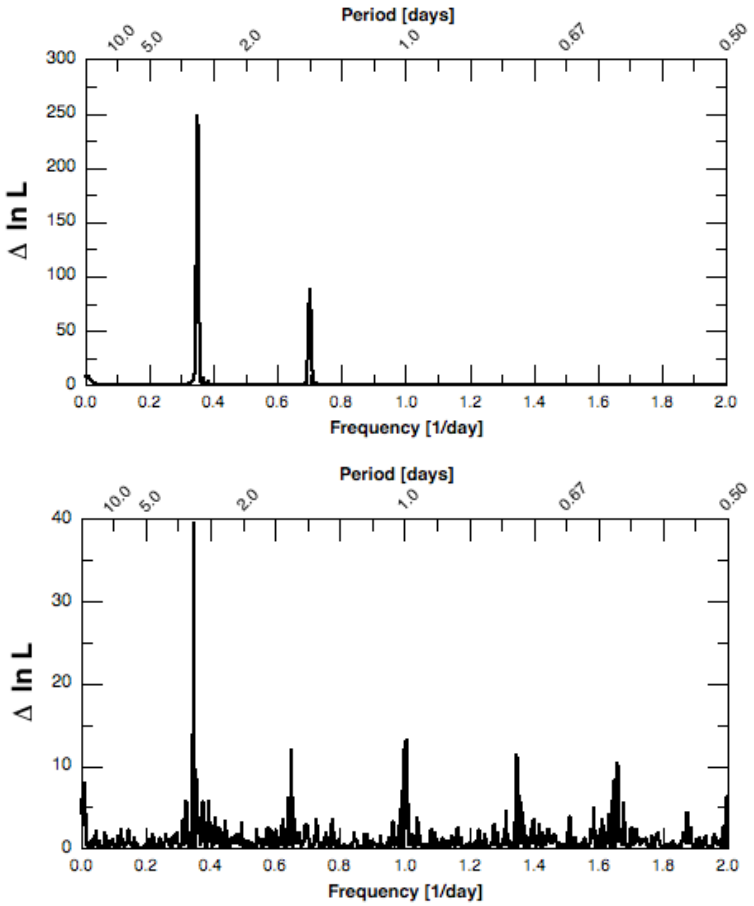

Figure 4.2.: Periodograms of the simultaneous ground based Red Dots photometry (bottom), and the non-simultaneous K2 photometry (top). Both sets show a strong signal near to 2.8 days, but the periods are not an exact match (Red Dots 2.87 days, K2 2.854 days). The much more precise K2 photometry, also shows overwhelming evidence of the first harmonic of the rotation period at a frequency of 1.427 days^{-1}. Because of the much more regular and higher cadence, the K2 periodograms are essentially free of aliases in this frequency range. On the other hand, the Red Dots photometry shows strong aliased signals.

uniformly, the frequencies are well spaced and free of aliases so the two peaks directly correspond to signals in the data. On the other hand, the periodograms of all the Red Dots photometry (and all other ground based data) contains strong aliasing issues due to the quasi daily sampling. The analysis of the photometry shows in all cases a strong peak at ∼2.8 to 2.9 days, which is the mostly likely value for the rotation period of the star (see later additional diagnostics). The K2 photometry also reveals a very strong signal at one half of this period (∼1.4 days). The Red Dots data also shows evidence for some long term modulation, but the baseline is insufficient to confirm periodicity or rule out instrumental systematic effects. The Red Dots data does not show strong evidence of the first harmonic at ∼1.4 days signal which was initially surprising given how strong it is detected in K2 data. We suspect that the reason for the absence of this first harmonic in the ground based photometry has to do with the variable nature of the spot distribution over time, the overlap of the signals of the two spots, their relative changes over time and the lower precision of ground based measurements.

4.4.4. Chomospheric indices

For this work, we obtained measurements of the equivalent width changes in H-alpha (656.28 nm air wavelengths, same as in Berdiñas et al. (2015), HARPS and CARMENES), and the S-index (following Anglada-Escudé & Butler (2012), HARPS only; 396.847 and 393.366 nm of the Ca H+K lines respectively). The value of the indicators for the spectra are in Table A.1.

Both Hα and the Ca H+K lines are in emission, indicating a bright and active chromosphere. The periodogram analysis of these lines, however, did not detect any significant signals, even after aggressive clipping and hand removal of some of suspicious values (outliers caused by background light, cosmic ray hits, etc). We suspect that most of the variability we observe for this star in this chromospheric indices is caused by constant micro flaring activity, which is essentially random. This is supported by the residuals to the fits of the K2 photometry, on which flare like events seem to be continuously overlapping to each other (see similar behaviour on GJ 1245A+B in Lurie et al. (2015)). The measurements are included in the on-line data table, but plots are not shown here for brevity.

4.4.5. Chromatic index (CARMENES only)

Spots have different temperatures than the rest of the photosphere. Therefore, one could expect colour dependent Doppler shifts when these are caused by spots. This could also be used to rule out candidate planets as the Doppler shift due to a planet do not have a colour dependent Doppler shift. The visual arm of the CARMENES spectroscope allows us to compute the Doppler shifts at wavelengths ranging from 500nm to 1 micron. As described in Zechmeister et al. (2018), the SERVAL pipeline provides a quantitative measure of the colour dependence of Doppler shifts via the so-called Chromatic index (CRX). The chromatic indices for the CARMENES spectra are in Table A.2.

We also analysed the time-series of this index in the same way as all the others. We did not find any significant periodicity in this index. While this might seem contradictory, this is actually consistent with the finding in Tal-Or et al. (2018), where only the most RV variable objects (RMS>30 m/s, the RMS of the RV measurements of Ross 154 is around 15 m/s) would show strong correlation of the RVs with this chromatic index. While some wavelength dependence of the spot induced signals would be expected, a more refined version of the CRX would be needed, for moderately active stars (this one) and less active stars.

4.4.6. Line profile moments

We use the procedure given in Strachan & Anglada-Escudé (2017) to produce differential least-square deconvolution (dLSD) spectral line profiles of all the observations. These are formally equivalent to the so called cross-correlation function (CCF) profiles of HARPS, once the average CCF profile is subtracted from the data. Given that the differential profiles are the residuals to the average line profile, the relative changes of the moments of the differential profiles must be the same as the real changes in the line profiles, given that the first three central moments of a distribution are additive (the moments are also the cumulants of the distribution). The approach of using the first three central moments instead of the CCF measurements provided by the automatic HARPS Data Reduction Software (DRS) was already shown to be equivalent in Berdiñas et al. (2015) and Berdiñas et al. (2017), and were also used in Anglada-Escudé et al. (2016), where the second moment was found to correlate quite well with the photometry (i.e. both photometric variability and changes in the line profile come from a dark spot). This procedure uses the star to generate an average template. It has the advantage that it is a purely differential procedure and does not depend on line-lists. Accuracy of the measurement is

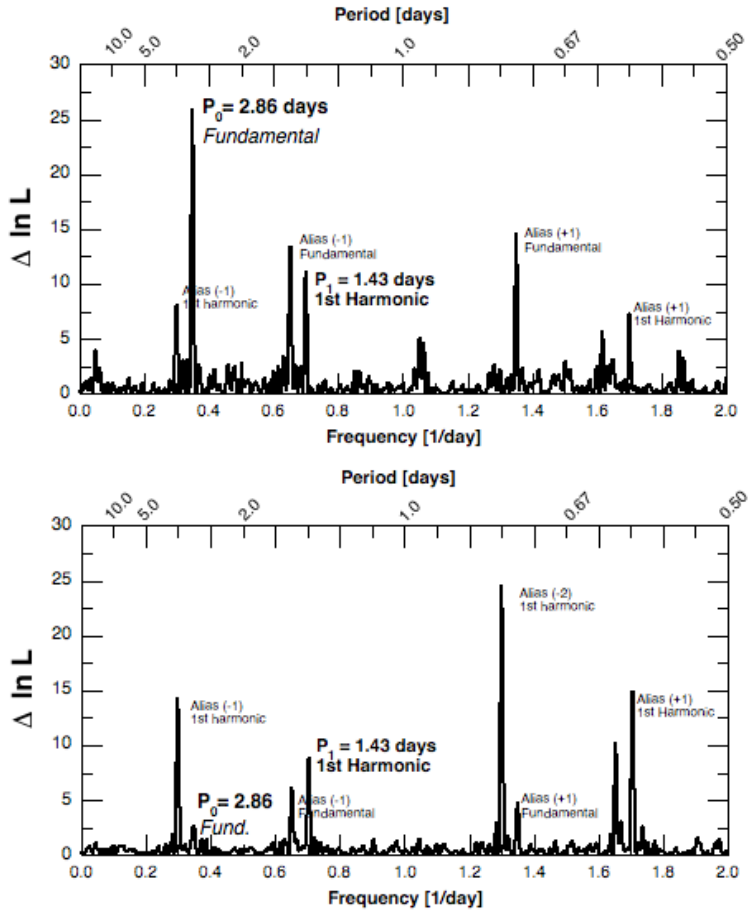

Figure 4.3.: Periodograms of the second (top) and third (bottom) moments of the HARPS dLSD profiles. Both show signals at the likely rotational period of the star at 2.86 days and its first harmonic at 1.43 days. Several other aliases to these signals are also present.

preserved even in the presence of blended lines.

The three moments m_1, m_2 and m_3 as we measure them are

$$m_1 = \sum_{i=1}^{n} v_i K(v_i), \tag{4.3}$$

$$m_2 = \sum_{i=1}^{n} (v_i - m_1)^2 K(v_i), \tag{4.4}$$

$$m_3 = \sum_{i=1}^{n} (v_i - m_1)^3 K(v_i), \tag{4.5}$$

where n is the number of elements in the dLSD profile and K(v_i) is the dLSD profile element at velocity v_i. The first moment m_1 is equivalent to the Doppler shift and will not be discussed here, m_2 represents a change in the width of the line (i.e. changes in the variance of a normal distribution), and m_3 represents a change in the symmetry of the line (changes in the symmetry of the line that cannot be explained by a pure Doppler shift). Any true Doppler shift will have m_2 and m_3 = constant over time (in the same way as CCF-FWHM and CCF-BIS from HARPS are constant for true Doppler signals, Boisse et al. (2011)). On the other hand, Doppler shifts caused by spots will have non-null m_2 and m_3 moments that will follow the changes in width and symmetry of the average spectral line. The m_2 and m_3 moments are given in Tables A.3 and A.4.

The analysis of the m_2 and m_3 time-series is illustrated in Figures 4.3. m_2 shows signals at 2.86 and 1.43 days, which correspond to the same signals in the photometry, especially the more precise K2 dataset and also shows several aliases to these signals. m_3 shows again signals at 1.43 days and 2.86 days, but this time the first harmonic is stronger. The different strengths of the harmonic components of spots is known and has been discussed in other works (Boisse et al., 2011). Later in this paper, we go to a more detailed modeling of the dLSD profiles. However, we add this analysis here as these are standard diagnostics in Doppler search programmes. The signals in both m_2 and m_3, are fully consistent with the picture emerging from the photometry. That is, that the observed variability in the different observables, mostly comes from one or two spots (or regions).

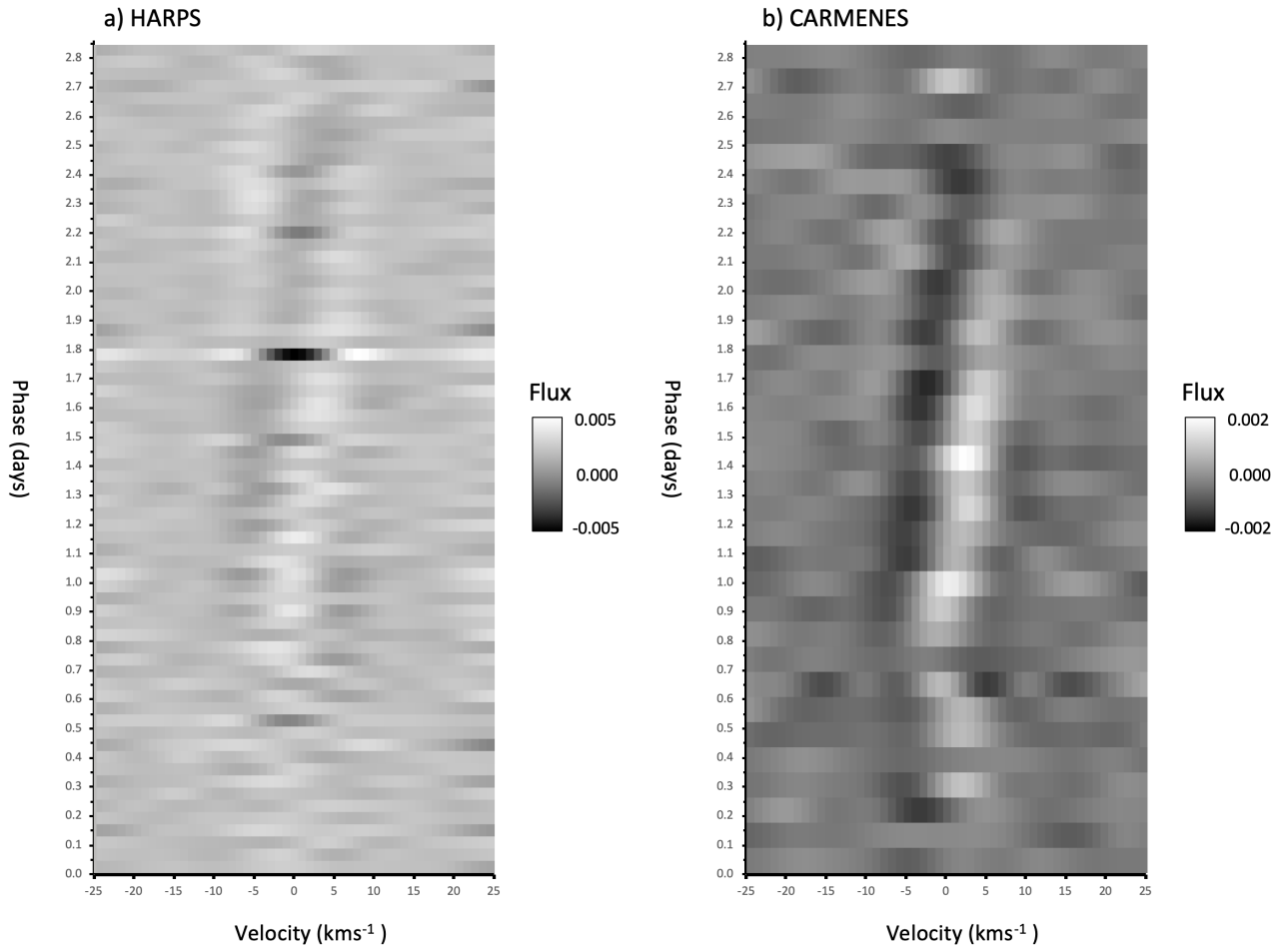

Figure 4.4.: dLSD spectral line profiles from tab a) the HARPS Red Dots spectra (orders 50 and above) and tab b) CARMENES spectra. All kernels have been ordered by phase 0 to 2.87 days. In tab a) the dark signal at phase 1.7-1.8 is due to a flare.

4.5. Modelling the Spots using dLSD

Due to the relatively low signal to noise of the spectra and the small amplitude of the distortion in the spectral lines due to stellar activity (spots) it is not possible to observe these distortions directly from an individual spectral line. dLSD is able to consolidate the information from the distortions in all the spectral lines in a spectrum and thus detect the stellar activity (spot).

dLSD uses a high signal to noise spectral template of the star T which is subtracted from each observed spectrum O_i of the star to form a residual spectrum R_i. The index i here is used to denote the ith observed spectrum of the star The dLSD spectral line profiles K_i are then determined by deconvolving the template T with R_i using the equation

$$R_i = T * K_i. \tag{4.6}$$

If there is activity/spots moving across the star then dLSD will detect this feature and produce a signal corresponding to the activity/spots centred at the velocity of the feature as it passes across the disk of the star. If the activity/spots are long enough lived then by phasing the dLSD spectral line profiles according to the estimated rotational period of the star then we should be able to detect the activity/spots moving across the star.

The forward model permits us to produce synthetic spectra and from that synthetic dLSD spectral line profiles for rotating stars which have spots. These synthetic dLSD spectral profile lines can then be fitted to the dLSD spectral line profiles derived from the HARPS/CARMENES spectra using parameter selection via a Bayesian analysis which uses a Markov Chain Monte Carlo (MCMC) method using the Metropolis-Hastings algorithm (Metropolis et al 1953). Full details of the forward model are given in Appendix A.1 and here we provide a brief summary.

The spectrum of the rotating star without spots is modelled by the following convolution

$$S_{R,no\ spot}(v) = S * \frac{G'}{\int_{-\infty}^{\infty} G' dv}, \tag{4.7}$$

where S is the rotationally unbroadened spectra of the star and G' is the rotational broadening kernel for the star. The integral in the denominator is to ensure that the convolution is normalised to conserve flux. The rotational broadening kernel incorporates a standard quadratic limb darkening model for the star (equation A.6). The limb darkening parameters for the model are determined using the Limb Darkening

Toolkit (Parviainen & Aigrain, 2015) and the values used and the photospheric parameters from which they are derived are given in Table A.5. For the rotation we use the 3kms^{-1} vsinI taken from Reiners et al. (2018).

In the forward model we use the high signal to noise template T(v) as $S_{R,no\ spot}(v)$ and we can then determine S by a deconvolution with G′.

The spectrum of a star with a spot on it is modelled as

$$S_{R,spot}(v) = \frac{1}{\int_{-\infty}^{\infty} G'(v')dv'} S * (G' - (1-\Gamma)D)(v), \tag{4.8}$$

where D corresponds to the flux blocked by the spot if it was black (it lets no flux through). As well as being a function of velocity D is also a function of the 4 free parameters in the model: t_{cm} - time of central meridian passing of the spot, R_s - the radius of spot, L_P - value of y-cood in plane of sky of the spot when it passes the meridian where origin of y-axis is centre of star and the y-axis corresponds to the projected axis of rotation of the star and I - inclination of the stellar spin axis relative to the line of sight.

In addition to the free parameters in the model there are a number of fixed system parameters whose values are given in Table A.5.

Γ is the fourth power of the ratio of spot temperature to the effective temperature of the star. In our analysis we assume that the spot is "black" with Γ having a value of 0.

dLSD is then carried out to determine the model dLSD spectral line profiles K_m from the following

$$S_{R,spot} - S_{R,nospot} = K_m * S_{R,nospot}. \tag{4.9}$$

A Bayesian analysis can then be performed in order to determine the posterior probability distributions of the four free parameters in the spot forward model using the kernel residuals derived from the HARPS/CARMENES spectra.

We can also use our forward model to predict observables from photometry. The photometry is relative and both the model and the observed data are normalised to the maximum of the light curve.

From the forward model (see Appendix A.1) we define the flux at time t as

$$F_m(t) = \int_{-\infty}^{\infty} G'(v)dv - \int_{-\infty}^{\infty} (1-\Gamma)Ddv, \tag{4.10}$$

where the suffix m stands for a flux derived from the forward model. We use the derived values for D and G' from the best fit to the HARPS dLSD spectral line

profiles.

We then define the standard flux value as

$$F_{m,standard} = max\{F_m(t) : t \in T\}, \tag{4.11}$$

where T is the set of observation times from the photometry.

Finally we define the normalised model flux as:

$$\hat{F}_m(t) = \frac{F_m(t)}{F_{m,standard}} \tag{4.12}$$

Actual photometric observations of the star are given in terms of number of counts (F_*) which is proportional to the number of photons received (assuming the data reduction has been performed to remove dark current etc). The data is fitted to a 5th order polynomial and the maximum from that curve is used to normalise the data. The observables can then be compared with the output from the forward model.

4.5.1. Results from dLSD and Comparing with the Forward Model

Initial attempts were made to identify spots with dLSD for the HARPS spectra using all the orders. This did not provide a clear signal of a spot (or group of spots) due to perhaps either the low SNR of the lower orders or lack of a periodic signal in the lower order. Evidence of a spot (or spot group) were found with orders 50 (at 553 nm) and above. Tab a) of Figure 4.4 shows the dLSD spectral line profiles for orders 50 and above for the HARPS spectra where the kernels are ordered by phase assuming the spot has a period of 2.87 days. It can clearly be seen that there is a feature/spot/group of spots moving across the star as a diagonal line going from left to right as the phase increases. This is analogous to the Rossiter McLaughlin effect for transiting exoplanets as shown in the previous paper using dLSD (Strachan & Anglada-Escudé, 2017). The dark line indicates that the spot is darker and this is confirmed as the part of the 2.87 day phase where the spot is present occurs when the photometry measurements have a low flux/magnitude (see Section 4.4.3).

The dLSD spectral line profiles for the CARMENES spectra were also produced and ordered by the 2.87 day phase (Tab b of Figure 4.4). The dLSD spectral line profiles showed the spot moving across the star as for the HARPS data.

We carried out the Bayesian analysis with the dLSD spectral line profiles from the HARPS Red Dots spectra assuming a black spot (we did not fit Γ due to its

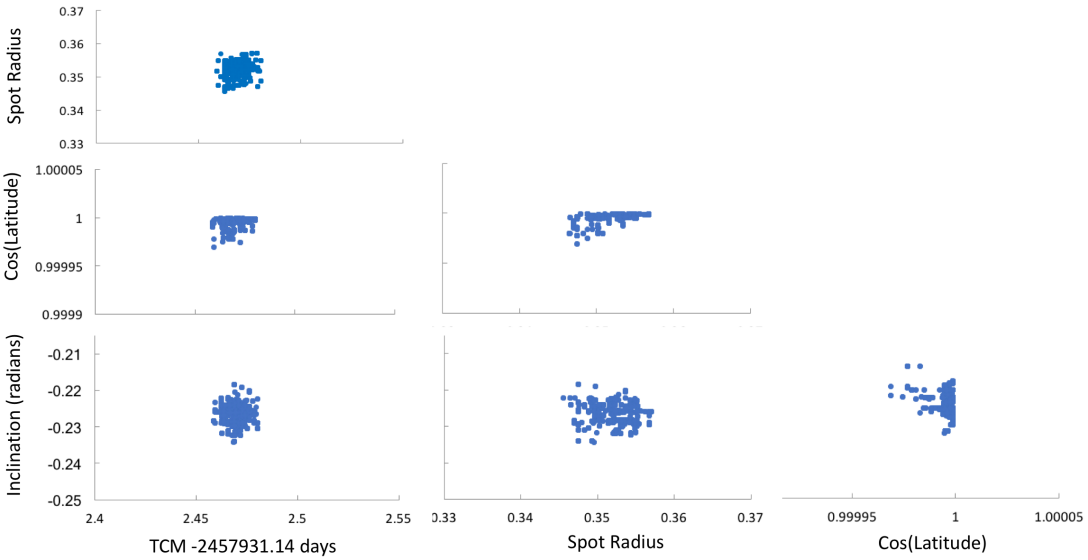

Figure 4.5.: Correlation diagrams for the four parameters from the forward models for a black spot fitted to the HARPS Red Dots spectra

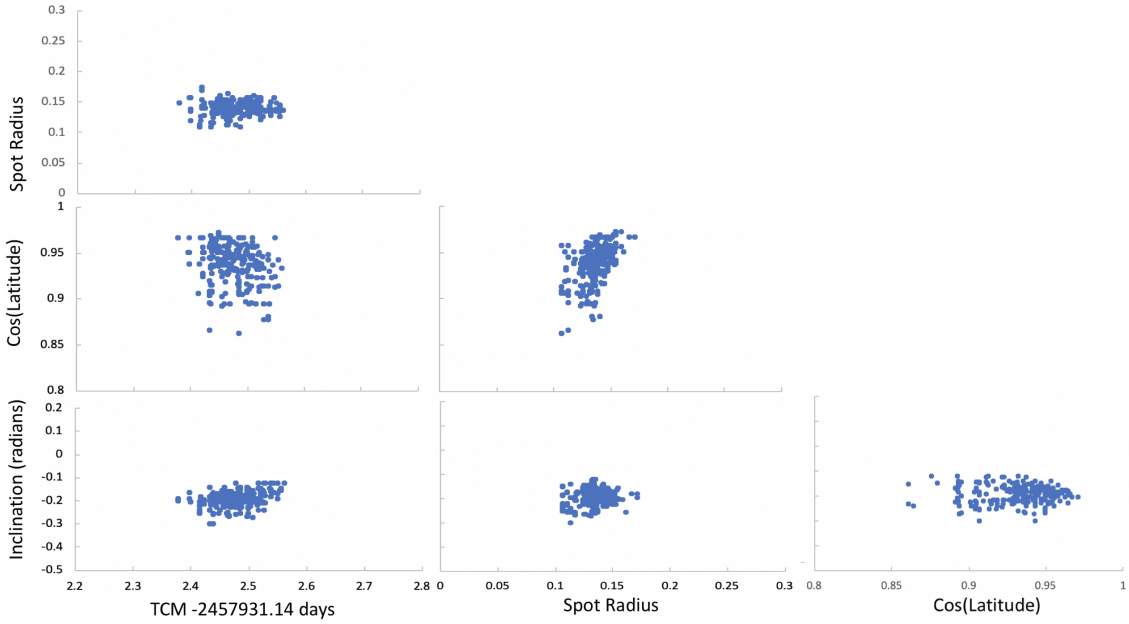

Figure 4.6.: Correlation diagrams for the four parameters from the forward models for a black spot fitted to the CARMENES Red Dots spectra

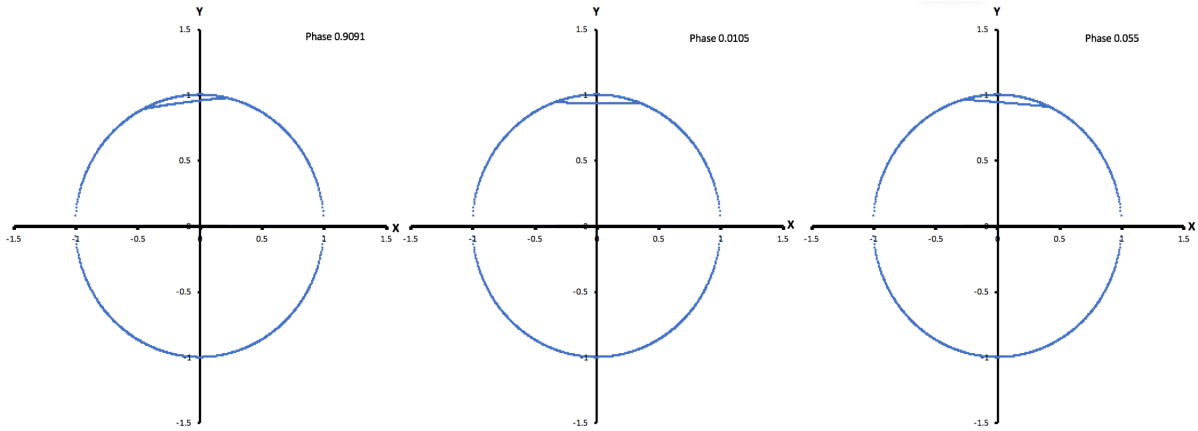

Figure 4.7.: Depiction of black spot moving across the star derived from forward model fitted to the HARPS data. The X and Y axis are in the plane of the sky and the Y axis coincides with the projection of the rotation axis in the plane of the sky.

strong correlation with the radius of the star). After allowing a burn in of 200 accepted proposals for the MCMC chain we then captured a chain of 1000 accepted proposals. A correlation diagram for the probability distributions of the four free parameters is shown in Figure 4.5. The free parameter for the coordinate of the y axis of the spot at time of central meridian passage is just $\cos\theta$. Where θ is the latitude (angle subtended at origin of star between the spot and the rotational axis of the star). This figure shows no significant correlation between the parameters. Table A.6 gives the mean and one sigma errors for the fitted parameters. We can see from the parameters that the spot is close to polar with a radius approximately a third that of the star and a representation of the spot as it crosses the star is given in Figure 4.7.

We carried out the same analysis on the CARMENES spectra. The correlation diagram is shown in Figure 4.6. Table A.7 gives the mean and one sigma errors for the fitted parameters. The spot again is at the pole though it is not centred on it. The spot is significantly smaller with radius $0.14R_*$. These differences could be explained by the wavelength coverage of CARMENES which operates at longer wavelengths than HARPS (see table A.5) where the spot may appear smaller.

We determined the photometric light curve for a black spot and fitted to the HARPS Red Dots spectra for Ross 154. Figure 4.8 shows the comparison of the forward model light curve against the ASH2 photometric R band measurements. We can see from the figure that the phase and the amplitude of the model fit are not in good agreement suggesting the one spot model is not adequate to describe the photometry.

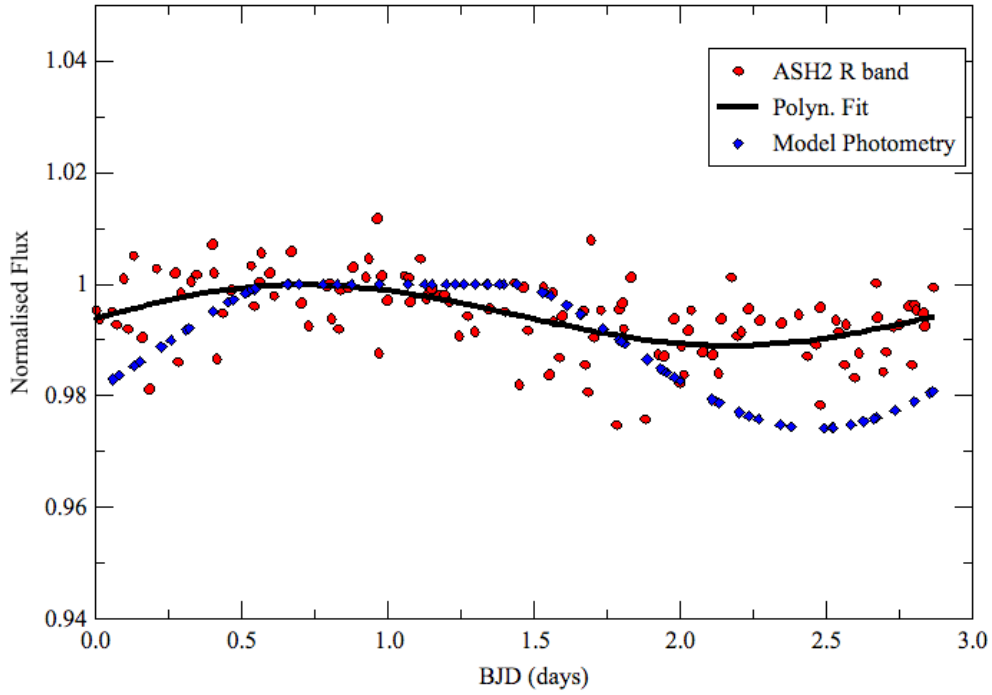

Figure 4.8.: R band photometric measurements from the ASH2 observatory (red dots) which have been normalised to the maximum of the 5th degree polynomial that has been fitted to the data (black line). The photometry derived from the one spot model is also shown (blue)

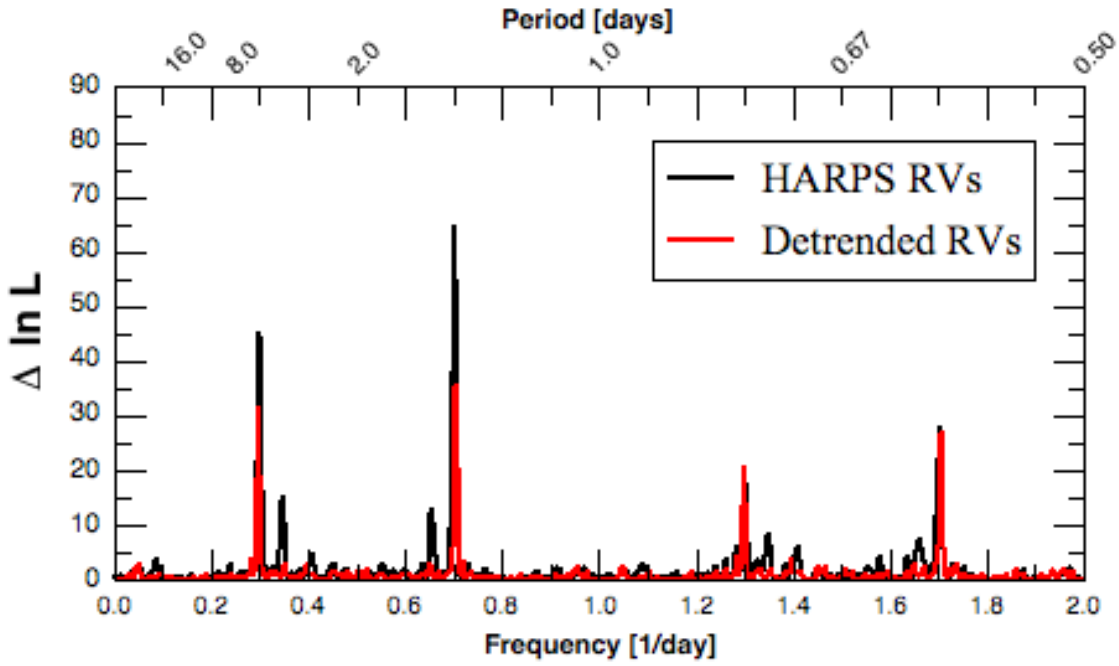

Figure 4.9.: Periodogram for the HARPS RVs compared with periodogram for these RVs but with Doppler shift due to polar spot from Forward Model removed. Stellar rotation period was set at 2.87 days

4.5.2. Analysis of detrended RVs

Given the fit to the forward model we can remove the activity from the RVs directly by observing that the velocity shift v_{shift} due to the stellar activity/spot for each spectrum observed at time t is the first moment of the broadening function G′ - (1-Γ)D:

$$v_{shift}(t) = \int_{-\infty}^{\infty} \frac{G' - (1-\Gamma)D}{\int_{-\infty}^{\infty} G' - (1-\Gamma)D dv'} v dv \tag{4.13}$$

Here G′, D amd Γ are as defined in equations 4.7 and 4.8.

We deliberately ignored the effect if any of convective blueshift (or redshift) in our velocity model as we expected this to be a second order effect (Cegla et al., 2016).

We determined the velocity shifts for the forward model with a black spot and fitted to the HARPS Red Dots spectra for Ross 154. We subtracted the velocity shifts from the HARPS RVs and ran the log likelihood periodogram on them. The periodogram for the first solution is shown in Figure 4.9 and a summary of the three solutions are given in Table 4.4.

The results from the log likelihood periodigrams show that the signal at 2.87 days has been significantly weakened to such an extent that it only appears in the three

Table 4.4.: Three strongest signals detected using the recursive log likelihood with the HARPS Red Dots RVs with the RV contribution from the detected spot removed.

One Signal Model	
Period (days)	1.42
Delta LogLikelihood	35.543
Amplitude (ms^{-1})	13.568
FAP	<0.001%
Two Signals Model	
Period (Signal 1)	1.42
Period (Signal 2)	18.835
Delta LogLikelihood	11.196
Amplitude (Signal 1) (ms^{-1})	14.1
Amplitude (Signal 2) (ms^{-1})	5.098
FAP	0.586%
Three Signals Model	
Period (Signal 1)	1.421
Period (Signal 2)	18.550
Period (Signal 3)	2.867
Delta LogLikelihood	10.479
Amplitude (Signal 1) (ms^{-1})	14.225
Amplitude (Signal 2) (ms^{-1})	5.371
Amplitude (Signal 3) (ms^{-1})	4.474
FAP	1.341%

Table 4.5.: Three strongest signals detected using the recursive log likelihood with the HARPS Red Dots RVs with the RV contribution from the polar spot and the second lower latitude spot removed.

One Signal Model	
Period (days)	1.42
Delta LogLikelihood	35.519
Amplitude (ms^{-1})	13.255
FAP	<0.001%
Two Signals Model	
Period (Signal 1)	1.42
Period (Signal 2)	18.808
Delta LogLikelihood	11.192
Amplitude (Signal 1) (ms^{-1})	13.774
Amplitude (Signal 2) (ms^{-1})	4.983
FAP	0.588%
Three Signals Model	
Period (Signal 1)	1.420
Period (Signal 2)	18.510
Period (Signal 3)	2.867
Delta LogLikelihood	10.408
Amplitude (Signal 1) (ms^{-1})	13.907
Amplitude (Signal 2) (ms^{-1})	5.304
Amplitude (Signal 3) (ms^{-1})	4.338
FAP	1.760%

signal model and that model has a FAP greater than 1%. The two signals model which includes 1.42 days and 18.8 days has a FAP greater than 0.5%.

The one spot signal model still however showed a significant signal at 1.42 days with a FAP of less than 0.001%. In order to check if this could be due to additional spots we repeated the steps in Section 4.5.1 this time fitting the dLSD spectral linee profiles obtained from the HARPS data minus the dLSD spectral line profiles obtained from the one spot forward model. The MCMC converged with a spot nearer the equator $L_P = 0.23$ but with a relatively small radius $0.04R_*$. Repeating the process of subtracting the RVs caused by the spot and then running recursive log likelihood periodograms showed no significant difference to the results (see Table 4.5).

In order to understand why a 1.42 day signal remained we first re-examined the photometry. The periodogram analysis of the K2 data though captured several years earlier had the strongest two signals at 2.854 and 1.427 days. The second signal being at exactly the first harmonic of the first. Perhaps the 2.87 period we were assuming for the rotational period of the spots was not accurate enough and that it should be 2.854 days. However even assuming this was the case the phase folded photometry for *Kepler* (Figure 4.10) was significantly different. It had two peaks in it as opposed to one. The time series of the *Kepler* photometry (Figure 4.10) also showed that the second peak was not always present and was sometimes present but of a smaller amplitude. In order to look for a potential second peak in the photometry we phased the AAVSO photometry to 2.854 days and chose photometry only on the nights where spectra were observed. We did not bin this data due to the lack of data points. The results are shown in Figure 4.11 where we can see that there is two peaks in this data.

Next we fitted the two spots to the HARPS dLSD spectral line profiles as we had done previously but using the *Kepler* derived period for the rotational period of the star. The fitted parameters are given in Table 4.6. We then derived the RVs for the spots and then used these RVs to detrend the HARPS RVs. The detrending reduced the scatter on the RVs from 15.3ms^{-1} to 9.1ms^{-1}. Finally we ran the recursive periodogram with the detrended RVs to examine the impact on the HARPS signals. The periodogram of the detrended RVs along with that from the original HARPS RV is shown in Figure 4.12. Although the periodogram of the detrended RVs still have the main signals from the periodogram of the HARPS RVs their log likelihood values are significantly less. In particular the False Alarm Probability for the strongest signal is greater than 2%.

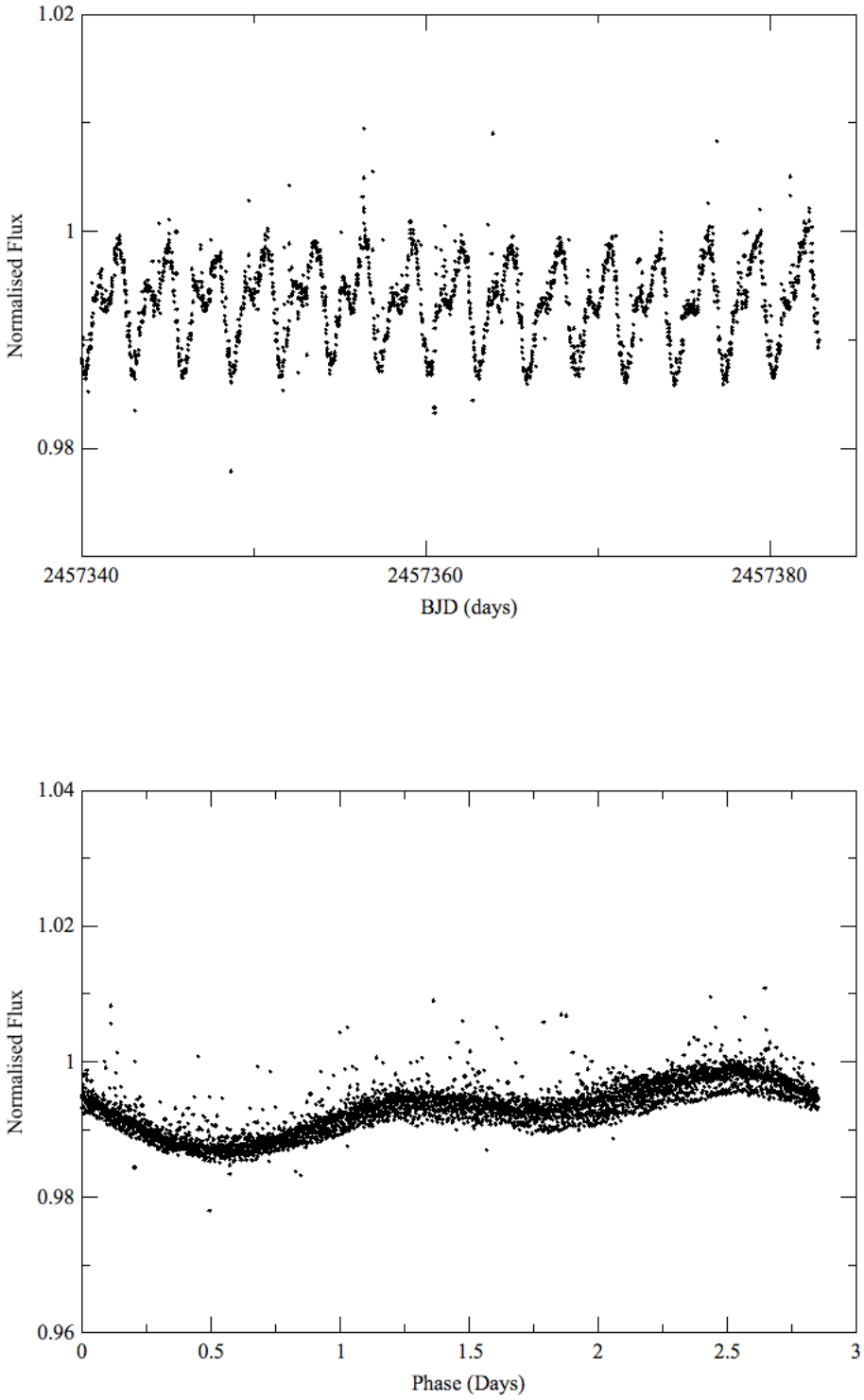

Figure 4.10.: Section of the time series of the K2 data clearly showing the 2.854 day periodicity along with a second spot which varies in strength (top). Phase folded photometry for the K2 data (bottom)

Table 4.6.: Mean and one sigma errors for the fitted parameters for the black spot forward model using the HARPS Red Dots spectra but using the *Kepler* period for the rotation of the star.

Parameter	Value	σ	units
cos(I)	-0.2513	0.0033	
Spot 1			
t_{CM}	2457933.9438	0.0034	BJD
R_s	0.3720	0.0022	R_*
L_P	0.999926	0.000010	R_*
Spot 2			
t_{CM}	2457932.397	0.010	BJD
R_s	0.1050	0.0021	R_*
L_P	0.762	0.012	R_*

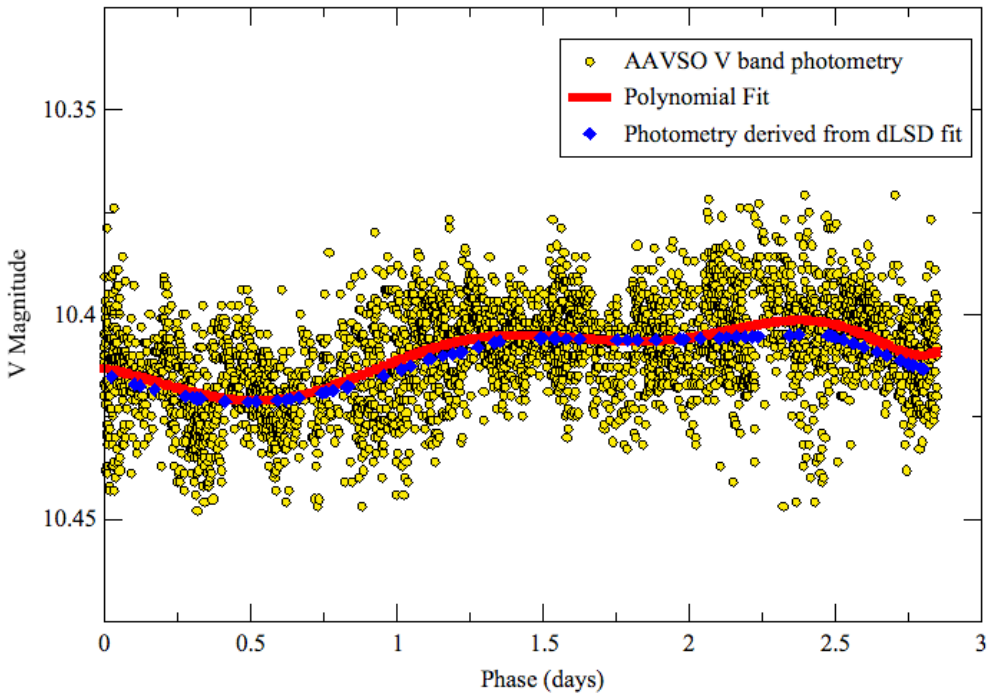

Figure 4.11.: V band photometric measurements from AAVSO observatory (in green) of the night when HARPS spectra were taken. A polynomial fit to this data is shown in red and the results of the photometry derived from fitting of a two spot model to the dLSD data are shown in blue.

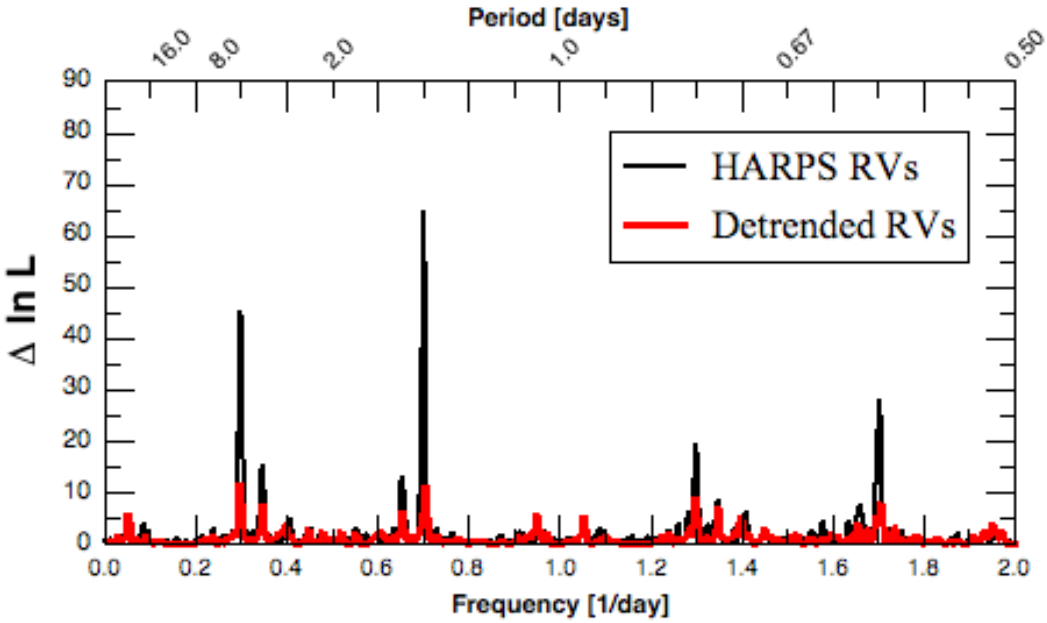

Figure 4.12.: Recursive periodogram showing the periodogram for the HARPS RVs (in black) along with the detrended HARPS RVs (in red). The RVs have been detrended by subtracting the RVs from two spots which had been fitted to the dLSD spectral line profiles and where the rotation period of the spots was taken from the *Kepler* photometry.

4.6. Summary and Conclusions

The Red Dots campaign and CARMENES observations have given us an opportunity to study Ross 154. Although the periodograms from the photometry, activity indices, moments and RVs spectroscopy suggested a stellar rotation period of between 2.86 and 2.87 days we suggest a more accurate value may be 2.854 days which came from the historic K2 data. This was confirmed by our ability to fit a two spot model to the dLSD profiles which we then used to detrend the RVs in order to successfully remove the majority of the activity from them.

We stress here the importance of having high quality photometry - ideally from space, taken simultaneously with the spectra and with regular sampling - in order to be able to identify activity on the stars and remove it. For Ross 154 we were fortunate that the signal of the spots seems to be fairly constant over time despite the strength of the second spot sometimes weakening according to the K2 data.

The potential planet candidate at 18.5 days was still present in the detrended RVs although not statistically significant. In order to confirm if it is a planet or otherwise we would recommend another campaign over a season with spectra captured daily in order for us to be able to easily disentangle the aliases and to see if the power of the 18.5 day signal would increase significantly.

Although the analysis performed has identified and quantified some of the stellar activity on Ross 154 more could yet be done for this star. Use of a higher resolution spectroscope such as ESPRESSO (Pepe et al., 2014) which has approximately twice the resolution of HARPS and CARMENES in its ultra high resolution mode would allow activity on the star to be monitored in significantly greater detail and further characterise the spots on the star. A high precision photometric campaign should be performed simultaneously with the spectroscopy and ideally would be space based similar to the *Kepler* photometry. The Transiting Exoplanet Survey Satellite (TESS) photometric survey (Ricker et al., 2010) would provide an excellent opportunity to study this star.

Acknowledgements

We are grateful to the HARPS team at Observatoire de Genéve, Observatoire de Haute-Provence, Laboratoire d'Astrophysique de Marseille, Service d'éronomie du CNRS, Physikalisches Institut de Universitat Bern, ESO La Silla, and ESO Garching, who built and maintained the HARPS instrument, and were generous enough to make the data public. We are also grateful to the members of the CARMENES consortium and the staff at Calar Alto Spain for making the observations and for

making the data available via their data archive. Thanks also go to the operators of the ASH2 and LCOGT observatories for capturing photometric data of the star. Thanks in paticular to Cristina Rodríguez-López for coordinating the photometry and providing me with access to the data. Thanks also to the AAVSO observers: John Briol, Franklin Guenther, Barbara Harris, John Hall, Franz-Josef Hambsch, Peter Nelson, Victor Ruiz and Chris Stockdale who took part in the campaign and provided photometric data. Finally, thanks also to NASA and to the Space Telescope Science Institute who have made photometry from *Kepler* publicly available via the MAST portal.

5. Doppler shifts and spectral line profile changes in the starlight scattered from an exoplanet

This chapter is based on the accepted paper Strachan & Anglada-Escudé (2020).

Abstract

Scattered starlight from an exoplanet, commonly called reflected light, can be used to characterise the planet including the determination of its albedo and inclination of orbit. The relatively low flux ratio between directly observed starlight and starlight scattered off hot Jupiters make these systems the prime candidates for detection of reflected light using high-resolution spectroscopy. The first detections have been claimed for 51 Peg b.

In a first calculation we derive the Doppler shift of reflected light measured by a remote observer for a planet modelled as a pointlike particle in orbit around a star. We find that the Doppler shift of reflected light from planets have a different Doppler shift to that of light emitted directly from the planet with magnitude equivalent to the radial motion of the planet with respect to the star. This only occurs for non-circular orbits.

Secondly, restricting our investigation to planets which are tidally locked and orbit in circular orbits we account for the finite size of the star and planet by integrating the contribution to a simulated spectral line across both their surfaces. Since exact analytical expressions cannot be easily derived as a function of all free parameters of the problem, we have developed a software tool called RESTART (REflected STARlighT) that produces the resulting line profiles. By applying it to study cases found in the literature, we explicitly show that hot Jupiters such as WASP-19b and 51 Peg b should show substantial broadening and asymmetric distortions compared to the nominal stellar line.

5.1. Introduction

Since the detection of the first exoplanet orbiting a main sequence star in 1995 (Mayor & Queloz, 1995) there are now over 4100 planet candidates with more than 400 of these being either hot or very hot Jupiters according to the Extrasolar Planet Encyclopaedia (Schneider et al., 2011). Hot Jupiters are defined as planets with mass approximately that of Jupiter (here we assume greater than 100 Earth masses) and which orbit in a period of 3-9 days and have a semi-major axis less than 0.1au. Very hot Jupiters orbit in period P<3 days. (Perryman, 2018).

Reflected light is the light scattered off the planet originating from its parent star. Reflected light is readily observed in the planets of the solar system. The continuum of a typical spectrum of a solar system planet has two peaks relating to where the reflected light dominates the spectrum at visible wavelengths and where thermal emission dominates in the near infrared. Models derived for the spectrum of hot Jupiters also show the same peaks (Seager, 2010).

Detecting reflected light is difficult. Even for planets in the solar neighbourhood there is a very small angle separating the planet from its parent star. This makes it difficult to separate the light from the planet and its parent star. This difficulty is compounded by the extremely small flux ratio between them (Claudi, 2016). The largest flux ratios are expected for hot Jupiters and to be of the order of a few parts in 10^{-5} and is due to the large size of the planet and its proximity to its parent star. For an Earth twin orbiting a Sun like star a contrast ratio is expected of the order 10^{-10} (Martins et al., 2016).

High-resolution spectroscopy is seen as a potentially advantageous method of detecting reflected light as although light scattered from the planet is expected to have a similar spectrum to the starlight (Seager & Sasselov, 1998) it can be disentangled from the spectrum of the star in velocity space due to the large Doppler shift of the planet with respect to the star. Various techniques have been used to identify the signal of the reflected light including most recently using cross correlation functions (CCFs) by Martins et al. (2015b) or auto correlation functions (ACFs) by Borra & Deschatelets (2018) on each spectrum. These techniques effectively combine the lines in the planet spectrum in order to increase the signal to noise. The CCFs (or ACFs) are then moved to the frame of the planet and combined in order to increase the signal to noise further to a level where the signal from the reflected light can be detected. If no detection can be made then an upper bound on the strength of the reflected light signal can be given. In order to know the wavelength position of the reflected light in the spectrum the required orbital parameters of the orbit need

to be known in advance and come from the transit and radial velocity (RV) planet detection methods. In the case where the planet does not transit then the inclination parameter has to be fitted whilst performing the search for the reflected light. Indeed detecting the reflected light for a system without a previously known inclination is important as once identified the mass of the planet can then be determined (Charbonneau et al., 1999).

Photometry can also be used to detect reflected light. Light curves with high enough signal to noise should be able to show the increase in light towards the superior conjunction and decrease towards inferior conjunction. The light curves of ν And b in the mid-infrared (Harrington et al., 2006) and HAT-P-7b in the visible (Borucki et al., 2009) provide examples of this. From the detection of reflected light in photometry the flux ratio can be determined and provide input to the required signal to noise required to detect the reflected light in high-resolution spectroscopy.

The 51 Peg system is the only system where high-resolution spectroscopic detection of reflected light has been claimed in the optical where Martins et al. (2015b) used the CCF method and Borra & Deschatelets (2018) used the ACF method. Contrast levels were of the order of 6×10^{-5} and significant broadening was observed in the CCF line profile. High precision photometry from MOST (Walker et al., 2006) of 51 Peg also shows evidence for reflected light with a light curve which peaks just before orbital phase 0.1 at a level of 2.5×10^{-4} greater than the minimum in the light curve.

In this paper we determine the Doppler shift of starlight scattered off of exoplanets and show how for hot Jupiters the scattering can result in significant broadening of the spectral line profiles. We have produced a tool called RESTART (Reflected STARlightT) which will produce a template spectrum of the reflected light from the planet based on the spectra from the star. This software tool is available on request from the author.

In Section 2 of this paper we describe analytical models for reflected light and also describe the code RESTART which models reflected light spectra.

In Section 3 we provide results from running RESTART for the examples of the very hot Jupiter WASP-19b, the hot Jupiter 51 Peg b, and an Earth analogue system where the system is 10 parsecs from the observer. We compare our results with what we expect and from the detection paper for 51 Peg b.

In Section 4 we give the discussion and Section 5 the conclusions to the paper. Appendices A to C provide derivations of some of the results that are referred to in Section 2.

5.2. Analytical model and the RESTART code

We first determine the Doppler shift formula in a suitable form for starlight reflected off of a particle (Section 2.1). Then using this equation we compute the Doppler shift of reflected light in a two-body star/planet system where the planet and the star are far enough away from each other that they can both be considered to be pointlike (Section 2.2). We then model the flux of reflected starlight from a star and planet two-body system where the size of the planet and the star has to be taken into account due to their proximity. We restrict the orbits in this system to be circular and the planet to be tidally locked which are expected for hot Jupiter systems (Section 2.3).

The final expressions for the flux from Section 2.3 cannot be easily solved analytically as a function of all the parameters of the problem. Thus we describe our software implementation called RESTART of these equations in Section 2.4 where we take as input the rotationally unbroadened spectrum from a star and have as output the spectrum of the reflected starlight as seen by a distant observer.

5.2.1. Doppler shift of light reflected from a pointlike particle

In order to detect scattered starlight from an exoplanet we need to be able to determine the Doppler shift of the reflected light as viewed by the observer on Earth. The non-relativistic Doppler equation commonly used for reflection off of a mirror from Anglada-Escudé et al. (2007) is

$$\nu' = \nu\left[1 - 2\frac{1}{c}\Big((\hat{\sigma}\cdot\hat{\mathbf{n}})(\mathbf{v_m}\cdot\hat{\mathbf{n}})\Big)\right], \tag{5.1}$$

where c is the speed of light, ν' is the Doppler shifted frequency, ν is the original frequency, $\hat{\sigma}$ is the unit vector of the incoming light ray, $\hat{\mathbf{n}}$ is the normal to the mirror and $\mathbf{v_m}$ is the velocity the mirror.

In the case of light scattering off of a particle we take the mirror to be perpendicular to the bisector between the incoming light ray and the outgoing scattered ray. Thus $\hat{\mathbf{n}}$ is

$$\hat{\mathbf{n}} = \frac{\hat{\sigma}' - \hat{\sigma}}{|\hat{\sigma}' - \hat{\sigma}|}, \tag{5.2}$$

where $\hat{\sigma}'$ is the unit vector of the outgoing ray.

Substituting this value for $\hat{\mathbf{n}}$ in equation 5.1 and denoting $\mathbf{v_p}$ as the velocity of the particle we have

$$\nu' = \nu + \frac{\nu}{c}\mathbf{v_p} \cdot (\hat{\sigma}' - \hat{\sigma}). \tag{5.3}$$

Setting $\Delta\nu = \nu' - \nu$ and using the non-relativistic version of the Doppler shift equation

$$\frac{\Delta\nu}{\nu} = \frac{\Delta \mathrm{v}}{c}, \tag{5.4}$$

where Δv is the Doppler shift of the outgoing ray in velocity space and then substituting for $\frac{\Delta\nu}{\nu}$ in equation 5.3 we have

$$\Delta \mathrm{v} = \mathbf{v_p} \cdot (\hat{\sigma}' - \hat{\sigma}). \tag{5.5}$$

The Doppler shift of scattered light caused by moving particles as a non-invasive way of determining the velocity of fluids has been studied extensively (see Charrett et al. (2012) for a review of laser Doppler velocimetry). Particles are inserted into the fluid (if the fluid itself is not reflective) and light rays usually using lasers are fired into the fluid. The light reflected is then captured on detectors and the frequency shift of the captured light is used to determine the velocity of the flows. The velocity flows studied range from small velocities to supersonic. In many cases these particles are small and exhibit mainly Rayleigh scattering (Yeh & Cummins, 1964) which is the same type of scattering we may expect from hot Jupiters (Seager & Sasselov, 1998). It is very straightforward to show that the equations used to determine the velocity of the flows in the aforementioned papers are consistent with equation 5.3.

5.2.2. Doppler Shift of reflected light from exoplanets modelled as pointlike particles

Here we determine the Doppler shift of reflected light observed from Earth of a star/planet system where the following assumptions hold:

1. the only gravitational influence on the planet in the system is the parent star so we can assume a simple two-body problem
2. the planet is far enough away from the star so that both objects can be treated as point masses and the starlight reaching the planet are in parallel rays
3. we ignore the effects of rotation of the planet and star

We follow the two-body problem as described in Murray & Correia (2010).

In the two-body problem the position of the planet with respect to the star is typically first determined in a planar Cartesian coordinate system xy which is in the plane of the orbit centred on the star, The coordinates of the planet are given by

$$x = r\cos f, \tag{5.6}$$

$$y = r\sin f, \tag{5.7}$$

where r is the distance from the planet to the star and f is the true anomaly (see Figure 5.1).

These equations are then transformed to the Cartesian coordinate system for the orbit in space where the X and Y axis are in the plane of the sky and the Z axis points towards the observer. The position of the planet with respect to the star is then given by the following equations

$$X = r(\cos\Omega\cos(\omega+f) - \sin\Omega\sin(\omega+f)\cos I), \tag{5.8}$$

$$Y = r(\sin\Omega\cos(\omega+f) + \cos\Omega\sin(\omega+f)\cos I), \tag{5.9}$$

$$Z = r\sin(\omega+f)\sin I, \tag{5.10}$$

where the three angles involved in the transformation are the longitude of ascending node Ω, argument of pericentre ω and inclination I. These angles are used to rotate the xy axis, which is in the plane of the orbit, to the XYZ axis which is the orbit in space.

The above three equations can be used to give the position of the planet with respect to the barycentre of the system if their right hand sides are multiplied by the factor $\frac{m_*}{m_*+m_p}$ where m_p and m_* are the mass of the planet and the star respectively.

Similarly the equations can be used to give the position of the star with respect to the centre of mass if their right hand sides are multiplied by the factor $\frac{m_p}{m_*+m_p}$ and ω is replaced by ω_* where $\omega_* = \omega + \pi$.

The equation for the velocity shift $\Delta\mathbf{v}$ due to the reflection is given in Equation 5.5 where in this case $\hat{\sigma}$ is the unit vector in the direction of the planet from the barycentre and $\hat{\sigma}'$ is the unit vector from the planet to the observer. In the XYZ coordinate frame $\hat{\sigma}$ and $\hat{\sigma}'$ are:

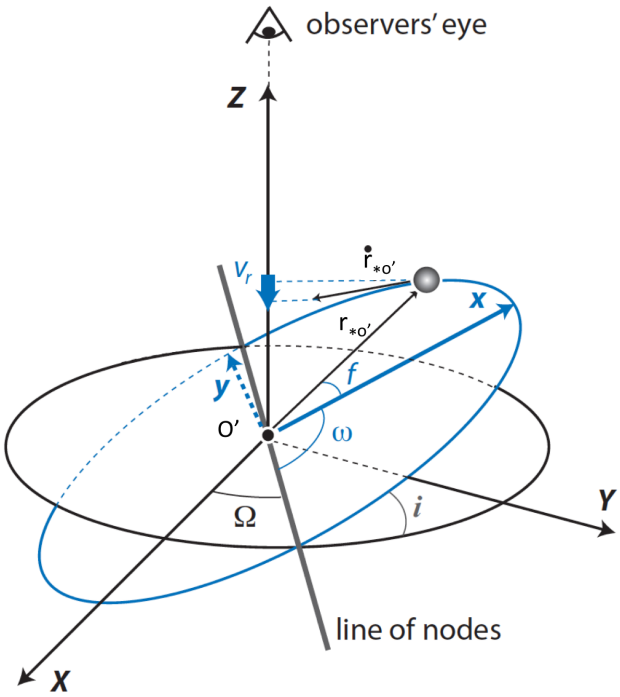

Figure 5.1.: The relationship between the plane of the orbit of the star (blue) to the plane of the sky (black) adapted from Murray & Correia (2010).

$$\hat{\sigma} = \begin{bmatrix} \cos\Omega\cos(\omega+f) - \sin\Omega\sin(\omega+f)\cos I \\ \sin\Omega\cos(\omega+f) + \cos\Omega\sin(\omega+f)\cos I \\ \sin(\omega+f)\sin I \end{bmatrix}, \tag{5.11}$$

$$\hat{\sigma}' = \begin{bmatrix} 0 \\ 0 \\ 1 \end{bmatrix}. \tag{5.12}$$

The position of the planet with respect to the observer is from Figure 5.2

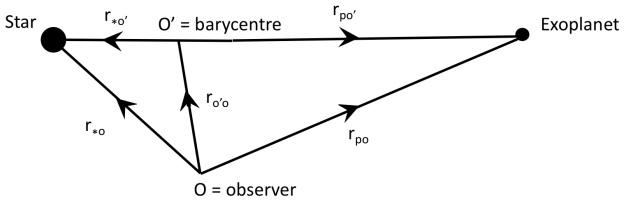

Figure 5.2.: Position vectors to planet and star with respect to barycentre O' and observer O.

$$\mathbf{r}_{po} = \mathbf{r}_{o'o} + \mathbf{r}_{po'}. \tag{5.13}$$

Differentiating we get the velocity

$$\dot{\mathbf{r}}_{po} = \dot{\mathbf{r}}_{o'o} + \dot{\mathbf{r}}_{po'}. \tag{5.14}$$

The first term on the right is the barycentric contribution to the velocity with respect to the observer. The second term is the velocity of the planet with respect to the observer. We will work in the barycentric frame to determine the velocity shift due to the reflection in that frame and then move to the observer frame to get the shift due to the observer moving with respect to the barycentre.

The velocity of the planet with respect to the barycentre is

$$\mathbf{v}_{p,b} = \dot{\mathbf{r}}_{po'} = \frac{m_*}{m_* + m_p} \begin{bmatrix} \dot{X} \\ \dot{Y} \\ \dot{Z} \end{bmatrix}, \tag{5.15}$$

where

$$\begin{aligned} \dot{X} = \dot{r}[\cos\Omega\cos(\omega+f) - \sin\Omega\sin(\omega+f)\cos I] \\ - r\dot{f}[\cos\Omega\sin(\omega+f) + \sin\Omega\cos(\omega+f)\cos I], \end{aligned} \tag{5.16}$$

$$\begin{aligned} \dot{Y} = \dot{r}[\sin\Omega\cos(\omega+f) + \cos\Omega\sin(\omega+f)\cos I] \\ + r\dot{f}[\cos\Omega\cos(\omega+f)\cos I - \sin\Omega\sin(\omega+f)], \end{aligned} \tag{5.17}$$

$$\dot{Z} = \dot{r}\sin(\omega+f)\sin I + r\dot{f}\cos(\omega+f)\sin I. \tag{5.18}$$

The observer in the barycentric frame observes the resultant effects of two Doppler shifts on the starlight. The first Doppler shift due to the radial component of velocity between the star and planet. The second Doppler shift due to the radial component of velocity between the planet and the observer. The total Doppler shift is given by

$$\Delta\mathbf{v}_{p,b} = -\frac{m_p}{m_* + m_p}\dot{r} + \mathbf{v}_{\mathbf{p},\mathbf{b}} \cdot (\hat{\sigma}' - \hat{\sigma}). \tag{5.19}$$

From equations 5.11 and 5.12 we have

$$\hat{\sigma}' - \hat{\sigma} = \begin{bmatrix} -\cos\Omega\cos(\omega+f) + \sin\Omega\sin(\omega+f)\cos I \\ -\sin\Omega\cos(\omega+f) - \cos\Omega\sin(\omega+f)\cos I \\ 1 - \sin(\omega+f)\sin I \end{bmatrix}, \tag{5.20}$$

and thus the total Doppler shift is

$$\Delta v_{p,b} = -\frac{m_p}{m_* + m_p}\dot{r} + \left(\frac{m_*}{m_* + m_p}\right)\left(\dot{r}[\sin(\omega+f)\sin I - 1] + r\dot{f}[\cos(\omega+f)\sin I]\right). \tag{5.21}$$

Now if we now consider the frame of the observer and assume the proper motion of the barycentre is V_z then we have

$$\Delta v_{p,o} = V_z - \frac{m_p}{m_* + m_p}\dot{r} + \left(\frac{m_*}{m_* + m_p}\right)\left(\dot{r}[\sin(\omega+f)\sin I - 1] + r\dot{f}[\cos(\omega+f)\sin I]\right). \tag{5.22}$$

From the point of view of the observer, the Doppler shift of light emitted from the planet is using Equation 5.14

$$\Delta v_{r,o} = \dot{\mathbf{r}}_{po} \cdot \hat{\mathbf{z}} = \dot{\mathbf{r}}_{o'o} \cdot \hat{\mathbf{z}} + \dot{\mathbf{r}}_{po'} \cdot \hat{\mathbf{z}}, \tag{5.23}$$

where $\hat{\mathbf{z}} = (0, 0, 1)^T$ and expanding out this equation using Equations 5.15 and 5.18 we have

$$\Delta v_{r,o} = V_z + \frac{m_*}{m_* + m_p}\left(\dot{r}\sin(\omega + f)\sin I + r\dot{f}\cos(\omega + f)\sin I\right). \tag{5.24}$$

Thus the difference between the Doppler shift of light reflected and light originating directly from the planet is given by

$$\Delta v_{p,o} - \Delta v_{r,o} = -\dot{r}, \tag{5.25}$$

where $\dot{r}$ is given in terms of eccentricity e, semi-major axis a, mean motion n where

$$n = \frac{2\pi}{P}, \tag{5.26}$$

and true anomaly f by

$$\dot{r} = \frac{na}{\sqrt{1-e^2}} e \sin f. \tag{5.27}$$

From the above equation we can see that there will be a difference in observed Doppler shift between reflected starlight and light emitted directly from the planet when either the eccentricity is 0 - we have a circular orbit - or when the true anomaly is 0.

An order of magnitude estimate of the size of $\dot{r}$ can be made by first observing that

$$\dot{r} \leq \frac{nae}{\sqrt{1-e^2}}. \tag{5.28}$$

From Kepler's third law we have

$$\mu = a^3 n^2, \tag{5.29}$$

where

$$\mu = G(m_p + m_*) \approx G m_* \tag{5.30}$$

and thus

$$\dot{r} \leq \frac{n^{1/3} \mu^{1/3} e}{\sqrt{1-e^2}}. \tag{5.31}$$

The upper bound for $\dot{r}$ given above can be expressed in terms of the period and eccentricity of the planet which we can obtain using the RV method and the mass of the star using equations 5.26, 5.29 and 5.30

$$\dot{r} \leq (2\pi G)^{1/3} m_*^{1/3} P^{-1/3} \sqrt{\frac{e^2}{1-e^2}}. \tag{5.32}$$

It is useful to express this equation in terms of more practical units

$$\dot{r} \leq 212.908 \text{ km s}^{-1} \left(\frac{m_*}{M_\odot}\right)^{1/3} \left(\frac{P}{\text{day}}\right)^{-1/3} \sqrt{\frac{e^2}{1-e^2}}. \tag{5.33}$$

When the eccentricity is small (e<<1) we can simplify the above equation to

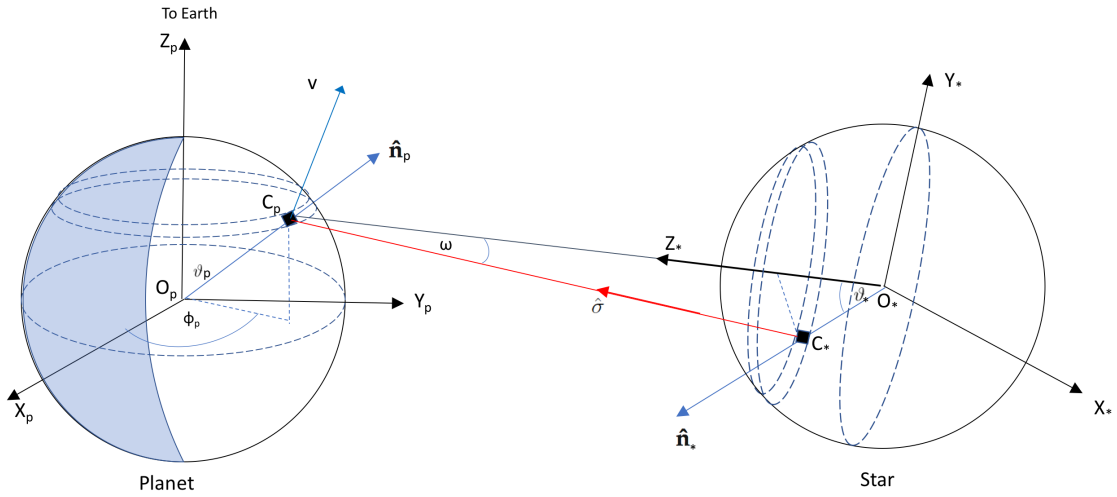

Figure 5.3.: Geometry showing the flux from the star to a point (ϑ_p, ϕ_p) on the planet

$$\dot{r} \leq 212.908 \text{ km s}^{-1} \left(\frac{m_*}{M_\odot}\right)^{1/3} \left(\frac{P}{\text{day}}\right)^{-1/3} e. \tag{5.34}$$

It is useful to observe that $\dot{r}$ is independent of the inclination of the orbit. An important implication of this is that high resolution spectroscopy could now be used to detect exoplanets, via detection of the Doppler shift of reflected light, in low inclination, even face on orbits, provided the orbits were eccentric.

5.2.3. Spectral line profile of reflected light from tidally locked hot Jupiters

In this subsection we outline how we determine the flux and thus spectral line profile of reflected light arriving at the observer on Earth from a tidally locked hot Jupiter in a circular orbit. Full details of the calculations are given in Appendix B.1. In this case our main assumptions are:

1. the only gravitational influence on the planet in the system is the parent star so we can assume a simple two-body problem

2. the tidal interactions between planet and star have caused the orbits around the barycentre to be circularised. The planet is tidally locked with the same face always pointing towards the star. All other tidal effects are ignored.

3. the planet and star are close enough to each other that the rays of starlight reaching the planet are not parallel

4. particles exist in the atmosphere (or on the surface) across the entire planet which reflect the starlight

The flux of the reflected light, $F_\oplus$, with frequency ν arriving at the distant Earth at time t is given by

$$F_\oplus(\nu,t) = \left(\frac{R_p}{d_{p\oplus}}\right)^2 \int_0^{2\pi}\int_0^{\pi/2} I_{s\vartheta_p\phi_p}(\vartheta_p,\phi_p,\nu,t) \sin\vartheta_p\cos\vartheta_p\, d\vartheta_p\, d\phi_p, \quad (5.35)$$

where R_p is the radius of the planet, $d_{p\oplus}$ is the distance from the planet to the Earth, ϑ_p, ϕ_p are colatitude coordinates centred on the planet and $I_{s\vartheta_p\phi_p}(\vartheta_p,\phi_p,\nu,t)$ is the intensity of the reflected starlight leaving the surface of the planet at cell (θ_p,ϕ_p) (see Figure 5.3). This intensity can be given in terms of the flux $H(\vartheta_p,\phi_p,\vartheta_*,\phi_*,\nu-\Delta\nu,t)$ reflecting off the planet cell (ϑ_p,ϕ_p) from the star cell (θ_*,ϕ_*)

$$I_{s\vartheta_p\phi_p}(\nu) = \int_0^{2\pi}\int_0^{\pi/2} \rho(\vartheta_p,\phi_p,\vartheta_*,\vartheta_*) H(\vartheta_p,\phi_p,\vartheta_*,\phi_*,\nu-\Delta\nu,t)(\hat{n}_p\cdot\hat{k})\, d\vartheta_*\, d\phi_*, \quad (5.36)$$

where $\rho(\vartheta_p,\phi_p,\vartheta_*,\vartheta_*)$ is the bidirectional reflectance distribution function (ratio of incident flux to reflected intensity), $\hat{k}$ is the unit vector in the direction of the Earth and the frequency Doppler shift $\Delta\nu$ is

$$\Delta\nu = \nu\frac{\Delta \mathrm{v}}{c}, \quad (5.37)$$

where Δv is the velocity shift due to the reflection of the light on the cell C_p and the shift due to the radial motion of the star cell with respect to the planet cell $\Delta v_{r,c_*c_p}$. This velocity shift is

$$\Delta \mathrm{v} = \mathrm{v}_p\cdot(\hat{k}-\hat{\sigma}) + \Delta \mathrm{v}_{r,c_*c_p}. \quad (5.38)$$

The surface velocity of the planet cell v_p is determined in Appendix B.2 and $\Delta \mathrm{v}_{r,c_*c_p}$ is determined in Appendix B.3.

We determine the flux $F_{\vartheta_p\phi_p}(\nu)$ at frequency ν arriving at a planet cell centred at $(\vartheta_p, \phi_p, R_p)$ by integrating all the contributions from the star cells

$$F_{\vartheta_p\phi_p}(\nu) = \int_0^{2\pi} \int_0^{\pi/2} H(\vartheta_p, \phi_p, \vartheta_*, \phi_*, \nu - \Delta\nu_*, t)\, d\vartheta_*\, d\phi_*, \tag{5.39}$$

where $H(\vartheta_p, \phi_p, \vartheta_*, \phi_*, \nu, t)$ is zero when starlight is blocked from reaching the planet cell:

$$H(\vartheta_p, \phi_p, \vartheta_*, \phi_*, \nu, t) \quad = \quad \begin{cases} 0, & \text{if } \hat{\sigma} \cdot \hat{n}_* < 0 \\ 0, & \text{if } -\hat{\sigma} \cdot \hat{n}_p < 0 \end{cases}, \tag{5.40}$$

otherwise non-zero when

$$H(\vartheta_p, \phi_p, \vartheta_*, \phi_*, \nu, t) = I_*(\vartheta_*, \phi_*, \nu, t)(-\hat{n}_p \cdot \hat{\sigma}) \left(\frac{-R_* \sin\vartheta_*}{\sqrt{R_*^2 + d^2 - 2R_* d cos\vartheta_*}} + \frac{R_* d \sin\vartheta_* (d - R_* \cos\vartheta_*)}{(R_*^2 + d^2 - 2dR_* \cos\vartheta_*)^{3/2}} \right), \tag{5.41}$$

and where $\hat{n}_p$, $\hat{n}_*$ are the unit normals to the surface of the planet cell and star cell, $\hat{\sigma}$ is the unit vector in the direction of the planet cell from the star cell, d is the distance from the planet cell to the centre of the star and $\Delta\nu_*$ is the frequency Doppler shift due to the motion of the star cell. $I_*(\vartheta_*, \phi_*, \nu, t)$ is the intensity of light from the surface of the star (the rotationally unbroadened stellar spectrum).

5.2.4. RESTART

RESTART is a software program that produces a synthetic spectrum of reflected light from hot Jupiters on circular orbits based on the spectrum of the star and the orbital parameters of the star-planet system. The code is written in Java and is portable to any system that supports the Java Virtual Machine. RESTART is available on request from the author.

There are two input files: the non-rotationally broadened spectrum or CCF of the star, obtained by deconvolving the CCF of the star with a rotational broadening kernel, and the parameters file containing the orbital details of the system and other configuration parameters. Table 5.1 gives an example of the contents of the configuration parameters file. The only output file is the spectrum of the reflected light. The files are in the format of comma separated files (csv files).

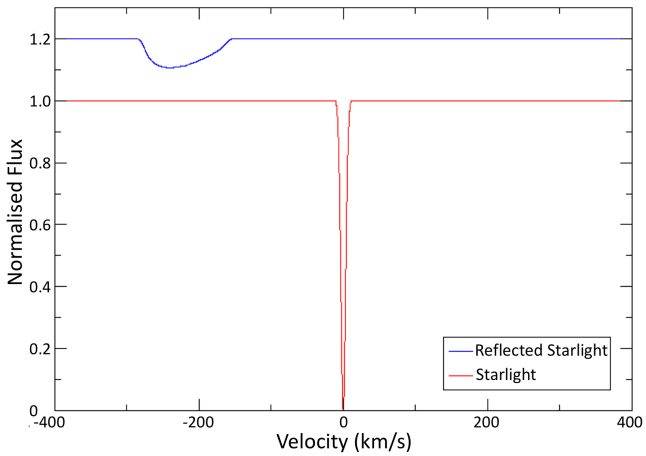

Figure 5.4.: In red the rotationally deconvolved absorption line from WASP-19 and in blue the reflected starlight as seen from an observer on Earth. The reflected starlight has been shifted by 0.2 units.The asymmetry of the line due to the phase of the planet can clearly be seen along in the reflected starlight spectrum along with the line broadening.

RESTART produces the output by performing a numerical integration of equation 5.35 in order to determine the flux of the reflected starlight observed from Earth.

5.3. Results from running RESTART

We ran the RESTART software for three systems. The first for a very hot Jupiter using the orbital parameters for WASP-19, the second for 51 Peg and thirdly for an Earth analogue at 10 parsecs.

Finally we explore the impact on line depth and FWHM for a hot Jupiter type system by changing a number of the key parameters of the system in turn: stellar radius, planet radius, stellar rotation and then planet to star distance.

5.3.1. Results for a very hot Jupiter system WASP-19b

The main input to RESTART is typically the non-rotationally broadened spectrum of the star. This spectrum can be obtained by deconvolving the observed stellar spectrum with a rotational broadening kernel.

In this analysis we use a simple single synthetic absorption line generated from a Gaussian function with FWHM= 8.963km s^{-1} - taken from FWHM of HARPS CCFs and deconvolved using the vsinI in Table 5.1. The line is centred at 0km s^{-1} as shown in Figure 5.4 Tab a) and has depth 1 relative to the continuum.

The input parameters for the system are given in Table 5.1. These parameters include the resolution number of 40 which means that the star and planet surface are broken into 40 × 2*40 = 3200 elements for the integration. The bidirectional reflection distribution coefficient was set to a constant $\frac{1}{\pi}$ so there would be isotropic scattering.

We ran RESTART with input time when the planet is at greatest elongation (t=2455169.16522 days). Figure 5.4 shows the normalised spectrum of the reflected light as seen from Earth. The asymmetry in the line is due to only one side of the planet being illuminated as viewed from Earth and due to the planet observed as rotating from Earth with period equal to that of the orbital period.

At greatest elongation we would expect the RV of light reflected from the substellar point of the planet to be at the velocity semi-amplitude where

$$K_{planet} = \frac{2\pi a}{P}\frac{\sin I}{1 + m_p/m_*} = 224\ km\ s^{-1}. \tag{5.42}$$

We fitted the reflected light to a Gaussian using the Levenberg-Marquardt algorithm and obtained a FWHM = 80.3 km s^{-1} which is over 10 times the FWHM of the line from the star. The Gaussian fit gave the centre of the line as -227.8 km s^{-1} and an amplitude of 0.1.

We checked the geometric albedo by running RESTART again this time setting the inclination to 90^o and the date to that corresponding to when the phase angle $\alpha = 0$ (time of secondary transit).

The expected geometric albedo can be derived from the following equation where the flux ratio between the reflected light and the light from the star and the planet (Collier Cameron et al. (2002a), Charbonneau et al. (1999) and Collier Cameron et al. (1999)) is

$$\epsilon(\alpha, \lambda) = \frac{F_{E,p}(\alpha, \lambda)}{F_{E,*}(\lambda)} = \Phi(\alpha, \lambda)p(\lambda)\frac{R_p^2}{d_{*p}^2}, \tag{5.43}$$

where $\Phi(\alpha, \lambda)$ is the the orbital phase function describing the amount of light reflected toward the observer at a given phase angle α and wavelength λ, p(λ) is the geometric albedo, R_p is the radius of the planet and d_{*p} is the distance from the planet to the star. All of the parameters on the right hand side of the equation except the geometric albedo are in Table 5.1 and the fluxes ratio on the left hand side comes from the continuum levels of the input spectrum file and the output spectrum file.

Using equation 5.43 we obtained p=0.68 which was only slightly higher than the

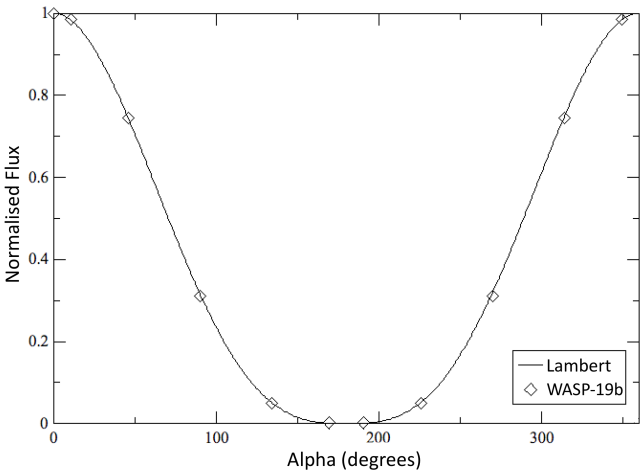

Figure 5.5.: Phase curve for reflected light of WASP-19b along with Lambert Phase Curve for comparison.

2/3 which would be expected for an isotropically scattered Lambert disk.

We next explored the phase curve for the planet by running RESTART for orbital phase $\theta = \{0, \pi/4, \pi/2, 3\pi/2, \pi, 5\pi/4, 3\pi/2\}$. where $\theta = 0$ is at time of central transit and having reset the inclination back to 79.4^o. The phase angle α is related to the orbital phase by

$$\cos\alpha = -\sin I \cos\theta, \tag{5.44}$$

from Mislis et al. (2012).

We normalised the flux values returned so that the flux at $\alpha = 0$ is 1 and plotted them against the curve of the Lambert phase function for this system (Figure 5.5). If the planet reflects light isotropically according to Lambert's law and we assume that the scattering phase function is grey - independent of wavelength - then we have from (Sobolev, 1975) that the Lambert phase function is:

$$\Phi(\alpha) = \frac{1}{\pi}[\sin\alpha + (\pi - \alpha)\cos\alpha]. \tag{5.45}$$

The figure shows that the reflected light from our model closely follows the Lambert phase function.

Finally we examined the line formed at time of secondary transit (superior conjunction). Figure 5.6 shows the line. It is as expected symmetric about velocity 0 km s^{-1} and when fitted with a Gaussian has a FWHM of 90.5 km s^{-1} and a line depth of 0.09.

Table 5.1.: Input Parameters for the very hot Jupiter

Parameter	Value	Units	References
t_0	2455168.96801	BJD	Hellier et al. (2011)
P	0.78884	days	Hellier et al. (2011)
m_p	1.168	m_{Jup}	Hellier et al. (2011)
R_p	1.386	R_{Jup}	Hellier et al. (2011)
m_*	0.97	$M_\odot$	Hellier et al. (2011)
R_*	0.99	$R_\odot$	Hellier et al. (2011)
Ω	0	Degrees	
i	79.4	Degrees	Hellier et al. (2011)
a	0.01655	au	Hellier et al. (2011)
$d_{*\oplus}$	270.409129	pc	Gaia Collaboration (2018)
vsinI	4.63	km s^{-1}	Hellier et al. (2011)
$P_{*,rot}$	10.5	days	Hebb et al. (2010)
resolution	40		
ρ	$1/\pi$		

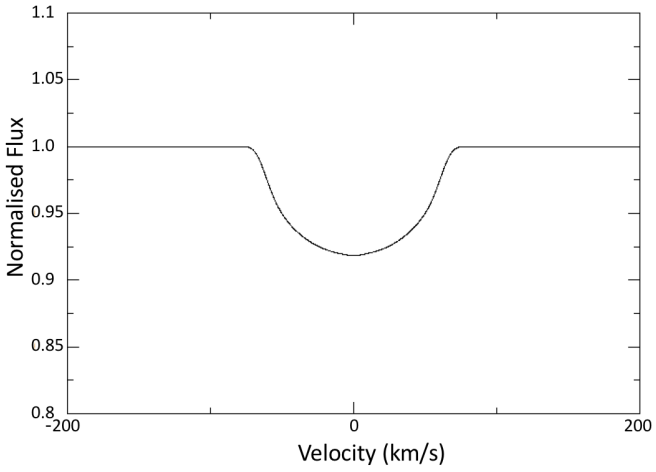

Figure 5.6.: Absorption line for reflected light for the very hot Jupiter WASP-19b at time of secondary transit.

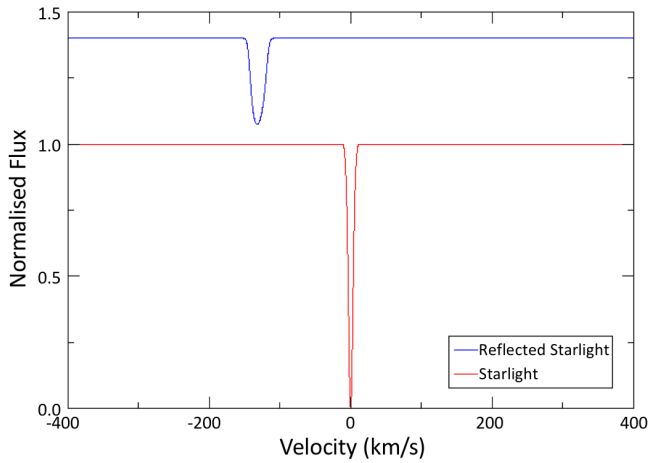

Figure 5.7.: In red the rotationally deconvolved absorption line from 51 Peg, in blue the reflected starlight from 51 Peg b. The reflected starlight has been shifted by 0.4 units.

5.3.2. Results for 51 Peg b system

As for WASP-19 we use a simple single synthetic absorption line generated from a Gaussian function with FWHM= 7.36 km s^{-1} taken from FWHM of HARPS CCFs and deconvolved using the vsinI in Table 5.2. The line is centred at 0 km s^{-1} as shown in Figure 5.7 and has depth 1 relative to the continuum.

The input parameters for the system are given in Table 5.2. We used a planet radius of 1.6 R_{Jup} as this according to the detection paper corresponded to a geometric albedo of 2/3.

We ran RESTART with input time when the planet is at greatest elongation (t=2456022.3137 days). Figure 5.7 shows the normalised spectrum of the reflected light as seen from Earth. The asymmetry in the line is due to only one side of the planet being illuminated as viewed from Earth and due to the planet being observed as rotating from Earth with period equal to that of the orbital period.

At greatest elongation we would expect the RV of light reflected from the substellar point of the planet to be at the velocity semi-amplitude where

$$K_{planet} = \frac{2\pi a}{P} \frac{\sin I}{1 + m_p/m_*} = 131 \; km \; s^{-1}. \tag{5.46}$$

We fitted the reflected light to a Gaussian using the Levenberg-Marquardt algorithm and obtained a FWHM = 19.0 km s^{-1}. The Gaussian fit gave the centre of the line as -131.2 km s^{-1} and an amplitude of 0.349.

Figure 5.7 shows in detail the reflected light absorption line. The line is slightly asymmetric with the deepest part of the line occurring at a velocity of -132 km s^{-1}.

Table 5.2.: Input Parameters for 51 Peg system

Parameter	Value	Units	References
t_0	2456021.256	BJD	Martins et al. (2015b)
P	4.231	days	Martins et al. (2015b)
m_p	0.457	m_{Jup}	Martins et al. (2015b)
R_p	1.6	R_{Jup}	Martins et al. (2015b)
m_*	1.04	$M_\odot$	Santos et al. (2003)
R_*	1.237	$R_\odot$	van Belle & von Braun (2009)
Ω	0.0	Deg.	
i	80	Deg.	Martins et al. (2015b)
a	0.052	au	Martins et al. (2015b)
$d_{*\oplus}$	14.7	pc	Gaia Collaboration (2018)
vsinI	2.8	km s^{-1}	Mayor & Queloz (1995)
$P_{*,rot}$	37.0	days	Mittag et al. (2018)
resolution	30		
ρ	$1/\pi$		

The asymmetry in the line is due to only one side of the rotating planet being illuminated as seen from Earth.

We examined the phase curve for the planet by running RESTART for a number of phases. We normalised the flux values returned so that the flux at $\alpha = 0$ is 1 and plotted them against the curve of the Lambert phase function (Figure 5.8. This figure shows that the reflected light from our model closely follows the Lambert phase function.

Finally we checked the FWHM and amplitude of the line RESTART predicts against the detected signal from. Martins et al. (2015b) at $\Phi(\alpha) = 0.87$. The FWHM from RESTART was 19.6 km s^{-1} which is within 1σ of the detected value 22.6 ± 3.6 kms^{-1}.

The flux ratio we obtained between the reflected light and the star at the same phase was 1.3×10^{-4}. However this is only the fractional difference in the level of the continuum but taking into account the reduction of the line amplitude due to the broadening (line amplitude was 0.41) we have a signal level of 5.4×10^{-5} which is within 1.5 σ of the detection result $6.0 \pm 0.4 \times 10^{-5}$ reported by Martins et al. (2015b). Increasing the radius of the planet to 1.7 R_{Jup} would bring the flux ratio to the detected value of 6.0×10^{-5}.

5.3.3. Results for a tidally locked Earth analogue

We used the absorption line generated for 51 Peg as the input stellar spectrum as 51 Peg has a similar spectral type to the Sun. The input parameters for the system

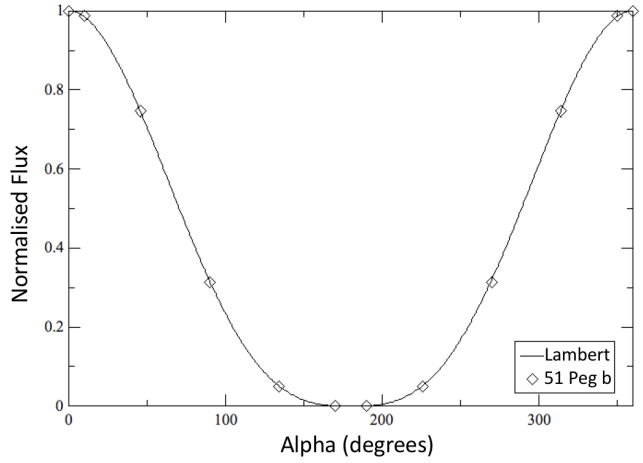

Figure 5.8.: Phase curve for reflected light of 51 Peg b along with Lambert Phase Curve for comparison.

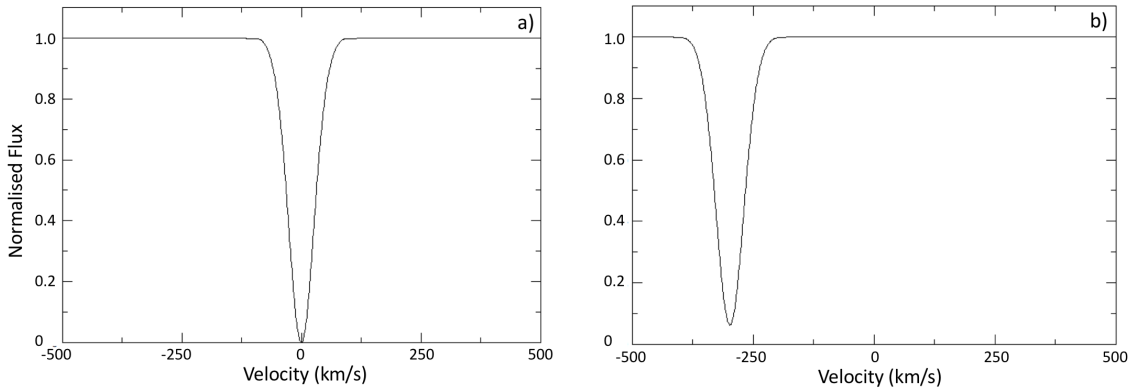

Figure 5.9.: Tab a) shows the rotationally deconvolved absorption line representing s solar line. Tab b) shows the reflected light as seen from Earth. Both tabs have had the continuum normalised to 1.

are given in Table 5.3.

We ran RESTART with input time when the planet is at greatest elongation. Figure 5.4 Tab b) shows the normalised spectrum of the observed reflected light.

At greatest elongation we would expect the RV of light reflected from the substellar point of the planet to be at the velocity semi-amplitude where

$$K_{planet} = \frac{2\pi a}{P} \frac{\sin I}{1 + m_p/m_*} = 29.8\ km\ s^{-1}. \tag{5.47}$$

Fitting a Gaussian using the Levenberg-Marquardt algorithm to the line gave its centre at -29.8 km s^{-1} as expected. Its FWHM of 6.8 km s^{-1} and depth of 0.93 showed broadening compared to the FWHM of 6.4 km s^{-1} and depth of 1.0 of the line before it was reflected. This is again due to light originating from opposing limbs of the star having different angles of incidence on the planet. In order to confirm this we reduced the radius of the Sun by a factor of ten and reran RESTART. This resulted in a line of depth 0.99 and FWHM of 6.4 km s^{-1} which were within 1% of the figures for the original line.

We checked the geometric albedo by running RESTART again this time setting the date to that corresponding to when the phase angle $\alpha = 0$ (time of secondary transit). The value for the geometric albedo obtained was p=0.668 which was consistent with the 2/3 which would be expected for a Lambert disk.

We next explored the phase curve for the planet by running RESTART for orbital phase $\theta = \{0, \pi/4, \pi/2, 3\pi/2, \pi, 5\pi/4, 3\pi/2\}$. where $\theta = 0$ is at time of centre of primary transit.

We normalised the flux values returned so that the flux at $\alpha = 0$ is 1 and plotted them against the curve of the Lambert phase function (Figure 5.10). This figure shows that the reflected light from our model follows the Lambert phase function.

5.3.4. Impact of system parameter changes to line depth and FWHM

Here we report on the impact on line depth and FWHM for a hot Jupiter type system by changing a number of the parameters of the system including star radius, planet radius, planet to star distance and stellar rotation in turn.

We use the parameters based on those for 51 Peg b as the base for the system except that we set the inclination to 90^o and the time of observation to be when the planet is fully illuminated with respect to the observer. This permits us to look at the system when the broadened line is symmetric. The parameters are specified in

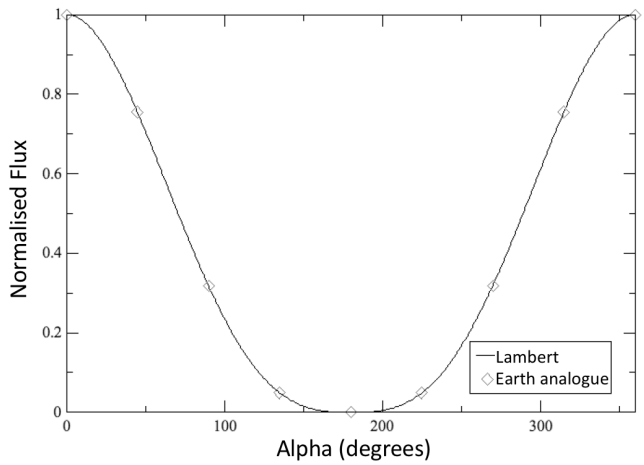

Figure 5.10.: Phase curve for reflected light from Earth analogue along with Lambert Phase Curve for comparison.

Table 5.3.: Input Parameters for the Earth analogue

Parameter	Value	Units	References
t_0	100.0	BJD	
P	365.25	days	
m_p	0.00315	m_{Jup}	
R_p	0.08921	R_{Jup}	
m_*	1.0	$M_\odot$	
R_*	1.0	$R_\odot$	
Ω	0	Degrees	
i	90	Degrees	
a	1.0	au	
$d_{*\oplus}$	10	pc	
$P_{*,rot}$	24	days	
resolution	30		
ρ	$1/\pi$		

Table 5.4.: Parameters set for hot Jupiter type system based on 51 Peg used for exploring the impact of system parameter changes to Line Depth and FWHM

Parameter	Value	Units	References
t_0	56020.756	MJD	Martins et al. (2015b)
P	4.231	days	Martins et al. (2015b)
m_p	0.457	m_{Jup}	Martins et al. (2015b)
R_p	1.6	R_{Jup}	Martins et al. (2015b)
m_*	1.04	$M_\odot$	Santos et al. (2003)
R_*	1.237	$R_\odot$	van Belle & von Braun (2009)
Ω	0.0	Deg.	
i	90	Deg.	
a	0.052	au	Martins et al. (2015b)
$d_{*\oplus}$	14.7	pc	Gaia Collaboration (2018)
vsinI	2.8	km s^{-1}	Mayor & Queloz (1995)
$P_{*,rot}$	37.0	days	Mittag et al. (2018)
resolution	30		
ρ	$1/\pi$		
FWHM	7.36	km s^{-1}	

Table 5.4.

The line depths and FWHM for the broadened lines output from RESTART are determined by fitting a Gaussian using the Levenberg-Marquardt algorithm as before.

The stellar radius was varied between 0.1 and 3 solar radii covering the domain of main sequence stars from M dwarfs to A stars. The results are shown in Figure 5.11. The FWHM is correlated with the stellar radius. We can also see that from approximately $0.5R_\odot$ upwards in stellar radius the increase in FWHM is approximately linear. In terms of line amplitude against stellar radius, below $0.5R_\odot$ the relationship is linear as it heads asymptotically towards the level of no broadening and a line amplitude of 1.

Next the planet radius was varied between 0.09 and 13 Jupiter radii covering the domain of Earth sized planets up towards the largest planets which approach 2 Jupiter radii and then beyond that in order to show the asymptotic relationship. The results are shown in Figure 5.12. The FWHM of the spectral line for the planet calculated from RESTART increases as we increase the planet radius. In particular this relationship when the planet radius is large ($>$ 8 Jupiter radii) is close to linear. As the planet radius decreases the FWHM asymptotically approaches a value of just over 19 km s^{-1} where the broadening is primarily due to the size of the star.

The line amplitude is inversely correlated with the planet radius. At planet radius 5-13 Jupiter radii the relationship with line amplitude is close to linear and as the

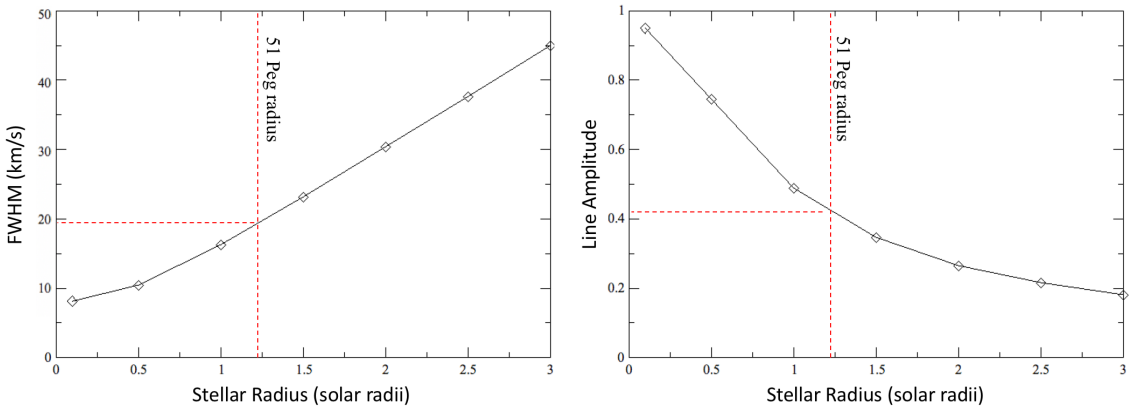

Figure 5.11.: Impact of change of Stellar Radius on FWHM (left) and Line Amplitude (right) for a hot Jupiter type system based on the 51 Peg system. The input parameters for the system are specified in Table 5.4.

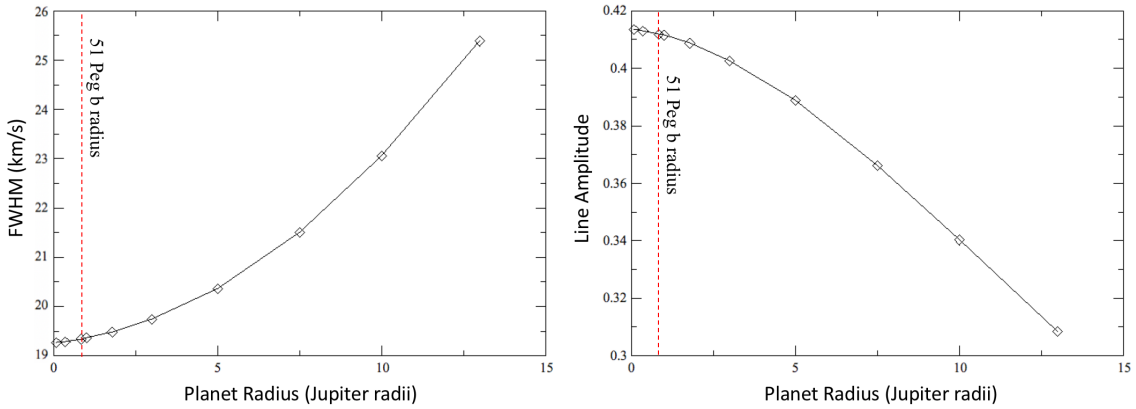

Figure 5.12.: Exoplanet system as for Figure 5.11 except showing the impact of change of Planet Radius on FWHM (left) and Line Amplitude (right).

planet radius decreases towards zero the line amplitude asymptotically approaches a value of just over 0.41.

The observed period of rotation of the star ($P_{*,rot}$) was varied between 0.1 and 100 days next. The results are shown in Figure 5.13. As expected the minimum FWHM and maximum line amplitude occurs when the planet and star are in synchronous orbit with each other which is when the observed stellar rotation period is at the planet orbital period of 4.231 days. As the observed stellar rotation period decreases below the orbital period then the broadening increases and the line amplitude decreases rapidly. For increasing stellar rotation period (as the star spins down) the broadening increases but then flattens out to a FWHM of just over 20 km s^{-1}.

Next we vary the distance between the star and the planet. In doing this we also modify the orbital period so that the system is consistent with Kepler's laws and

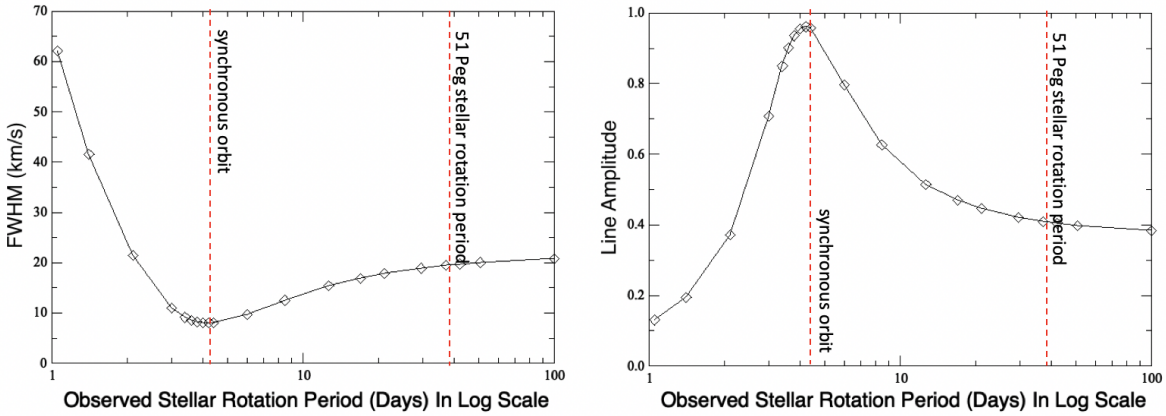

Figure 5.13.: Exoplanet system as for Figure 5.11 except showing the impact of change of Stellar Rotation on FWHM (left) and Line Amplitude (right).

we modify the observed stellar rotation so that it is always 30 days longer than the orbital period of the system. The results are shown in Figure 5.14. Here we see that the broadening is small with FWHM ¡ 10 km s^{-1} until the distance between planet and star is less than 0.25au and then as we get closer to the star the level of broadening increases and the line amplitude decreases very rapidly.

Finally we vary the distance between the star and the planet again but this time we also vary the observed stellar rotation so that its rate is that of the orbital period of the planet and thus the orbits are synchronised. The results are shown in Figure 5.15. The broadening is minimal until 0.05au where the broadening increases steeply with decreasing distance between planet and star. The broadening is due to the large range of incident angles for starlight being reflected from the planet due to the proximity of the star to the planet.

5.4. Discussion

In the development of the model for reflected starlight we have deliberately excluded a number of mainly lower order effects from the model. Here we describe some of them and detail how future versions of the model could include them.

We have only including isotropic scattering $\rho =$ constant in our model calculations resulting in the planet phase curves closely resembling those for a Lambert phase curve. For non isotropic and multiple scattering of reflected light from exoplanets (Seager et al., 2000) we would need to identify types and sizes of scatterers in the

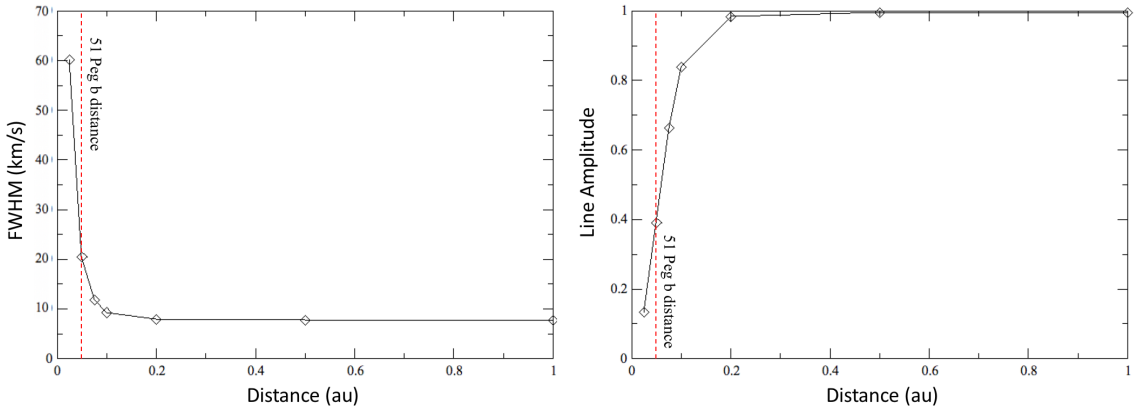

Figure 5.14.: Exoplanet system as for Figure 5.11 except showing the impact of change of distance between planet and star on FWHM (left) and Line Amplitude (right).

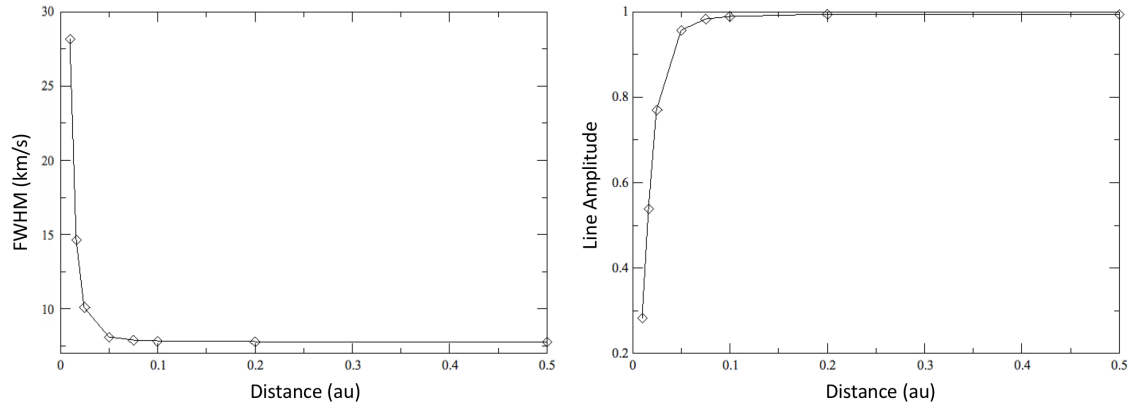

Figure 5.15.: Exoplanet system as for Figure 5.11 except showing the impact of change of distance between planet and star on FWHM (left) and Line Amplitude (right) for a synchronised hot Jupiter system

atmosphere of the planet along with their relevant phase functions. Models for these scatterers already exist, for example see the aforementioned paper and could be incorporated into the model.

We have also not taken account of the velocities of the particles/winds in particular those due to recirculation from day to night side which can be important in particular for hot Jupiters. These winds have been measured e.g. (Louden & Wheatley, 2015) and are typically of the order of a few km s^{-1}.

In terms of tides we have not taken account of the deformed shapes of the planet and star in our model. For instance Correia (2014) estimated the level of deformation of close in exoplanets assuming the deformed shape was in the form of a triaxial ellipsoid. For WASP-19b they estimated the length of the three axis to be 17.3, 15.4 and 14.8 $R_\oplus$ under the assumption that if the planet were spherical its radius would be $15.2R_\oplus$. In terms of our model this means that we would underestimate the flux and line broadening at greatest elongation and overestimate it at time of secondary transit. The size of the deformations are based on assumptions on the Love number used and to date no evidence of the deformations have been observed. We could similarly update the model to include the ellipticity of the star and gravitational darkening due to tides using a model such as that outlined in Jackson et al. (2012). For WASP-19b the maximum increase in radius due to tides would be $3.32 \times 10^{-4} R_*$.

Although it is expected that most hot Jupiters orbit their parent star in circular orbits and are expected to be tidally locked we could also lift these assumptions from our model.

5.5. Conclusions

In this work we have shown using a simple model of scattering that the Doppler shift of reflected light from planets whose parent star is at a distance where the light rays arriving at the planet can be considered to be parallel, have a different Doppler shift to that of light emitted directly from the planet. The magnitude of this difference in Doppler shift is equivalent to the radial motion of the planet with respect to the star.

We also showed that in the case of planets close to the parent star and in particular hot Jupiters the reflected starlight observed should be broadened due to the difference in angles of incidence of starlight arriving at the planet from different limbs of the star. We gave estimates for this broadening and developed a model that describes the scattering that takes place for tidally-locked hot Jupiters in circular

orbits.

We implemented the model in software (RESTART) and then ran this software tool for three exoplanets:. We found that significant broadening occurred for the WASP-19b very hot Jupiter system and significant broadening also took place for the 51 Peg b system. Our results for 51 Peg were consistent with the detection results provided we assumed the planet had size of $1.7R_{Jup}$. Very minimal broadening took place for our Earth analogue

Light curves produced for all three planets showed no significant deviations from a Lambertian phase curve as was expected for isotropic scattering.

Acknowledgements

We are grateful to the HARPS team at Observatoire de Genéve, Observatoire de Haute-Provence, Laboratoire dAstrophysique de Marseille, Service d'éronomie du CNRS, Physikalisches Institut de Universitat Bern, ESO La Silla, and ESO Garching, who built and maintained the HARPS instrument, and were generous enough to make the data public.

6. Conclusions

In Chapter 2 I stated that one of the major questions humans have asked is whether there is life out there in the universe or are we alone? I then stated that the detection of exoplanets gave new possibilities for the search for life outside our Solar System. I also noted that currently detecting Earth like planets in the habitable zones of nearby solar type stars was extremely difficult with the current sensitivity of detection methods. However, detecting Earth like planets in the habitable zones of M dwarfs was significantly easier with transiting planets around several M dwarfs already detected. But we still have to wait until JWST to potentially detect biosignatures in the atmospheres of these planets.

I discussed some limitations with using CCFs as part of the radial velocity for detecting exoplanets. This included line blending in M dwarfs and mentioned an alternative method which was differential and used stellar templates which addressed these limitations.

In Chapter 3 I reported on a differential method dLSD that I had developed which measures small changes in the mean line profile of a spectrum. This method had the advantage that as it was differential it did not require linelists and could be used on stars with blended lines such as M dwarfs. I showed that dLSD could be used successfully to determine the projected spin orbit misalignment angle of a transiting planet and the projected equatorial velocity of its host star.

In Chapter 4 I reported on my research in attempting to detect planets orbiting the M dwarf Ross 154. The star was active with a lot of short term activity related to the rotation of the star. I used dLSD and developed Doppler imaging code which was able to map spots on the surface of the star. I used this information of the spots to determine the radial velocity shifts that they caused and I then used these shifts to detrend the activity from the measured RVs of the star. The detrended velocities had no significant planetary signals in them.

In Chapter 5 I showed how the observed line profiles of starlight reflected from a planet are Doppler shifted and broadened. This is an important step in building an accurate model template for the reflected starlight in order that it can be compared with the reflected starlight buried in the spectra of the star.

I now look at future research at two levels: tactical and strategic. Tactical is short term research that can be done and completed now by myself or others. Strategic is research typically over a much longer time frame that cannot be completed until facilities (telescopes, detectors, spectrographs) exist which have the sensitivity, precision etc for the work to be completed.

At the tactical level there is a significant set of small projects some of which have been discussed in earlier chapters. I include them below.

6.1. Tactical level research

6.1.1. Transiting exoplanets

I am Principal Investigator on a project which has just won Director Discretionary Time (DDT) to observe the transit of a planet using ESPRESSO on the VLT. The planet is a Neptune size/mass planet on a 8.46-day orbit around a nearby pre-main sequence (approx. 20 Myr) M dwarf star. The planet was preliminarily detected in Doppler radial velocity time series and recently confirmed to be transiting with data from the NASA/TESS mission. A paper reporting on these results led by Peter Plavchan is currently in preparation.

The project will obtain high-resolution spectra with ESPRESSO to measure the Rossiter-McLaughlin effect and constrain the spin-orbit alignment of the star and planet, and retrieve the planets atmospheric transmission spectrum. Since the star is an M type star it will be an excellent candidate to use dLSD to determine the projected spin-orbit alignment of the star and planet. The Rossiter-McLaughlin effect will also be measured using radial velocities and compared with the results from dLSD. The hope is that the observations will allow us to study for the first time the early phases of the atmospheric and dynamical evolution of such planets.

6.1.2. Performance Improvements for spot and transit forward models

dLSD requires significant computer processing power and as datasets (number of spectra) grow larger it will become prohibitive to run on the laptop which I use currently. I have already improved the performance by having the option of loading all the data into memory at the start of the run.

The algorithm is also amenable to parallelisation, There are two main loops in the algorithm: the outer one one for processing each spectra and the inner one which

processes each order within a spectrum. Each of these loops could be rewritten so that they are run concurrently in their own thread. So in theory you would have number of spectra times number of orders running in parallel which should lead to significant performance improvements.

6.1.3. Functional Update to RESTART

As reported in the discussion in Chapter 5 there are several updates to the RESTART program which should be made in the next version of the code:

- Generalising the software to cope with planets on elliptical orbits.
- Including the effects of tides distorting the shapes of the planet and star.
- Allowing for different types of scattering models based on the expectation of the types and sizes of particles that are expected to be present in the atmosphere of the planet.
- Taking into account winds on the planet.

6.1.4. Search for reflected light

This research involves conducting a search for reflected light using the dLSD algorithm and taking account of the expected spectral line broadening and Doppler shifts using RESTART. New HARPS datasets for 51 Peg b are becoming publicly available this year which should permit a straightforward detection of the reflected light for the planet and potentially allow us to determine the wavelength dependence of the albedo of the planet. In addition obtaining spectra from other spectroscopes with different wavelength coverage such as CARMENES, would allow further determination of the wavelength dependence of the albedo for the planet.

6.1.5. Search for molecules in planetary atmospheres

In Section 2.7 we discussed the possibility of using dLSD instead of cross-correlation to search for molecules. This has yet to be done and it would be interesting comparing the results from the currently used CCF method.

6.2. Strategic level research

I take the main strategic goal to be detecting biosignatures in the atmospheres of exoplanets. I now show where my research in this thesis and extensions to it can have an impact on achieving this strategic goal.

As discussed earlier in this chapter searching transiting Earth like planets in the habitable zone of M dwarfs is currently the best chance to find biosignatures.

Searches for biosignatures could be done using JWST which is expected to launch in 2021. There are 9 rocky candidates on the Habitable Exoplanet Catalog. In addition to these there are expected to be 10 exoplanets found with TESS in the habitable zone orbiting M dwarfs with radius 1.25 to 2.5 Earth radii (Barclay et al., 2018b). Only a couple of these TESS planets may be Earth sized (<1.5 Earth radii) as opposed to super Earths. Thus we are talking around 10-15 habitable zone Earth like planets which could be analysed with JWST. A significant number of transits will have to be observed to identify biosignatures. Barstow & Irwin (2016) suggested that an Earth like ozone layer, if it exists, could be detected in 30 transits by JWST for TRAPPIST-1c and 60 transits for TRAPPIST-1d, assuming an Earth-like atmosphere.

The research I have performed relates to high resolution spectroscopy and the JWST instrument NIRSpec (Near InfraRed Spectroscope) to be used in the search for biosignatures is a low resolution spectroscope (R 1000-2700) so it may seem that my research may not have an impact on this work. However I do not think that should be the case. It will be vital to understand the activity on the star when observations are being made to rule out false positives from the JWST observations. Ideally photometry and high resolution spectroscopy should be done at the same time as the observations to identify and characterise any short term activity on the star which would have an impact on the JWST observations. My use of dLSD with Doppler imaging has shown that I can track short term activity on M dwarfs. I could do this on the M dwarfs being observed by JWST.

An alternative search for biosignatures is to use ground based observations. Proxima b being our closest habitable zone exoplanet has after the transiting nearby exoplanets the best opportunity to detect biosignatures. Techniques such as high dispersion spectroscopy and high contrast imaging (HDS+HCI) can be used together to detect the reflected light in the optical or the thermal emission from the planet in the infrared. Lovis et al. (2017) suggested a HDS+HCI method using SPHERE high contrast imager on the VLT to analyse the reflected light of Proxima b with ESPRESSO. This could retrieve the O_2 biosignature from Proxima b in 20-40

Table 6.1.: Next generation of large telescopes

Name	Diameter (m)	Collecting area (m^2)	First light
Extremely Large Telescope (ELT)	39.3	978	2025
Thirty Metre Telescope (TMT)	30	655	2027
Giant Magellan Telescope (GMT)	24.5	368	2025

nights of observation.

The dLSD software I have produced could be used to help detect the reflected light here instead of using CCFs. In particular the dLSD software could be adapted to include searching for reflected light with the relevant biosignatures in it, including O_2 in this case.

The next generation of large telescopes (Table 6.1) have the potential to let us detect biosignatures of Earth like exoplanets orbiting M dwarfs from the ground far more quickly. For example, it has been estimated (Lovis et al., 2017) that the atmospheric characterisation of Proxima Centauri b could be accomplished in about 6 nights using ELT and it is clear that the GMT (Giant Magellan Telescope) and the TMT (Thirty Metre Telescope) would also be able to characterise the atmosphere of Proxima b. The ELT will have the high resolution METIS spectrograph at first light which works in the infrared. A second generation spectrograph (HIRES) will eventually be available which is high resolution in the visible and the infrared. The GMT will have the GMT-Consortium Large Earth Finder (G-CLEF) high resolution spectrograph available at first light which operates in the optical and will be ideal for searching for biosignatures in reflected light (Szentgyorgyi et al., 2018). dLSD could be used to help with the detection of these biosignatures with the data from the next generation of telescopes.

If there is no success in finding biosignatures around M dwarfs and in any rate to continue with our search for habitable planets we will have to observe planets in the habitable zone around solar type stars. A number of these planets will be detected with the PLATO (PLAnetary Transits and Oscillations of stars) mission which has a planned launch date of 2026.

According to Snellen et al. (2019) direct imaging with a large space telescope is the only way to obtain spectra of the atmospheres of rocky planets in the habitable zones of solar type stars in a systematic way, because ground based instrumentation is unable to reach the extreme contrasts (order of 10^{-10} required). Thus new space based direct imaging systems will have to be built for this.

NASA are producing plans for two space based direct imaging systems, HabEx (Habitable Exoplanet Observatory) and LUVOIR (Large UV Optical Infrared Sur-

veyor). Reports on these systems have just been completed for the 2020 Astrophysics Decadal Survey. The reports are available on their websites at https://www.jpl.nasa.gov/habex/ and https://asd.gsfc.nasa.gov/luvoir/. Both systems have the ability to detect biosignatures in the atmospheres of Earth like planets in the habitable zone of solar type stars.

HabEx has a single 4 metre mirror and can perform high contrast imaging using a coronagraph or a starshade. The high contrast it achieves is of the order of 10^{-10}. It is expected to launch in the mid 2030s and detect and characterise the atmospheres, including detecting biosignatures, of 7.8 exo-Earths (in the habitable zone of solar type stars) using low resolution spectroscopy R=140 during its 5 year mission.

LUVOIR has two proposed versions: LUVOIR-A and LUVOIR-B. LUVOIR-A has an on-axis 15 metre primary mirror. It is expected to detect 54 habitable candidate exo-Earths. It will characterise their atmospheres, including detecting biosignatures using the ECLIPS instrument which is a combined coronagraph, low resolution integral field spectrograph (R = 70-200) and imaging camera.

LUVOIR-B has an off-axis 8 metre primary mirror and is expected to detect 28 habitable candidate exo-Earths and characterise their atmospheres using the ECLIPS instrument.

The planned launch date for LUVOIR is 2039.

Of course detecting biosignatures is only an indicator that life may be there. It may be a false positive. The next steps would be to do further characterisation including performing exoplanet surface imaging (EPSI) of the planet so that continents/oceans could be observed from photometry and spectroscopy (Berdyugina & Kuhn, 2019). In order to reduce the contrast between the planet and star adaptive optics and coronography will be used and EPSI is within reach of the next generation of coronagraphic telescopes. For example, a hybrid telescope-interferometer of 1220m diameter could generate surface maps in different colours for the nearest exoplanet, Proxima b. Dozens of Earth-size exoplanets and hundreds of larger planets could be imaged this way with such a telescope of 30m or larger diameter.

Finally we would want to visit the planet.

A. Appendix for Chapter 3

A.1. Forward Model

Our Forward Model follows the exoplanet transit model given in Hartman et al. (2015) but with modifications due to the fact we are dealing with spots. The spectrum S_R of the rotating star without spots is given by the convolution

$$S_{R,nospot} = S * G, \tag{A.1}$$

where S is the unbroadened spectrum of the star, G is the broadening kernel. Following Gray (2005) G is given by

$$G(v) = \frac{G'(v)}{\int_{-\infty}^{\infty} G'(v')dv'}, \tag{A.2}$$

where v is velocity and we scale the velocity so that a value of 1 corresponds to the v_{eq}sinI of the star. G′(v) is defined in terms of an integral of stellar surface brightness I(v,y). The coordinate system we are using is in the plane of the sky with the centre of the star at the origin and where the y-axis corresponds to the projected stellar rotation axis in the plane of the sky and the x-axis is perpendicular to that axis. The z-axis points towards the observer. Thus G′(v) is

$$G'(v) = \int_{y_{min}(v)}^{y_{max}(v)} I(v,y)dy, \tag{A.3}$$

where velocity v represents the ordinate for the x-axis and

$$y_{min}(v) = -\sqrt{1-v^2}, \tag{A.4}$$

and

$$y_{max}(v) = \sqrt{1-v^2}. \tag{A.5}$$

The stellar surface brightness I(θ) is defined using a standard quadratic limb darkening law

$$I(\theta) = I_c(1 - u_1(1 - cos\theta) - u_2(1 - cos\theta)^2), \tag{A.6}$$

where θ is the angle between the line normal to the stellar surface and the line of sight from centre of star to observer.

Using this equation, equation A.3 becomes

$$G'(v) = 2(1 - u_1 - u_2)\sqrt{1 - v^2} + \frac{\pi}{2}(u_1 + 2u_2)(1 - v^2) - \frac{4}{3}u_2(1 - v^2)^{3/2}, \tag{A.7}$$

when $|v| \leq 1$ and is 0 when $|v| > 1$.
The denominator for equation A.51 becomes

$$\int_{-\infty}^{\infty} G'(v')dv' = \pi(1 - u_1/3 - u_2/6). \tag{A.8}$$

We model a rotating star with a spot as

$$S_{R,spot}(v) = \frac{1}{\int_{-\infty}^{\infty} G'(v')dv'} S * (G' - (1 - \Gamma)D)(v), \tag{A.9}$$

where the removal of light from the spectrum of the star due to the spot is given by the function $(1 - \Gamma)$D(v) where D(v) is the light that would be emitted from the region of the star where the spot is if the spot were not there and Γ is an estimate of the fraction of light that the spot lets through. For Γ we assume the fraction of light the spot emits is given using the Stefan-Boltzman law

$$\Gamma = \frac{T_S^4}{T_*^4}, \tag{A.10}$$

where T_S is the effective temperature of the spot and T_* is the effective temperature of the star. D(v) in given in terms of intensity by

$$D(v) = \int_{y_1(v,x_P,y_P,R_s)}^{y_2(v,x_P,y_P,R_s)} I(v, y)dy, \tag{A.11}$$

where y_2 and y_1 are the maximum and minimal values on the Y-axis which contain the spot for a given value of v.

From Hartman et al. (2015) D(v) can be expressed as

$$D(v) = (y_2 - y_1)(1 - u_1 - u_2(2 - v^2)) + \left(\frac{1}{2}u_1 + \frac{2}{3}u_2\right)(y_1^3 - y_2^3) + \frac{1}{2}(u_1 + 2u_2)\Bigg\{(y_2 - y_1)(1 - v^2) + (1 - v^2)\Bigg(sin^{-1}\left(\frac{y_2}{\sqrt{1 - v^2}}\right) - sin^{-1}\left(\frac{y_1}{\sqrt{1 - v^2}}\right)\Bigg)\Bigg\}. \quad \text{(A.12)}$$

In order to determine y_2 and y_1 at any given time t we have to be able to track the spot as it moves around the star. We do this through a series of four rotations. The rotations are performed using the three basic rotation matrices $\mathbf{R}_x, \mathbf{R}_y$ and $\mathbf{R}_z$ defined in equations A.13, A.14 and A.15 in a right handed coordinate system

$$\mathbf{R}_x(\theta) = \begin{bmatrix} 1 & 0 & 0 \\ 0 & cos\theta & -sin\theta \\ 0 & sin\theta & cos\theta \end{bmatrix}, \quad \text{(A.13)}$$

$$\mathbf{R}_y(\theta) = \begin{bmatrix} cos\theta & 0 & sin\theta \\ 0 & 1 & 0 \\ -sin\theta & 0 & cos\theta \end{bmatrix}, \quad \text{(A.14)}$$

$$\mathbf{R}_z(\theta) = \begin{bmatrix} cos\theta & -sin\theta & 0 \\ 0 & 1 & 0 \\ sin\theta & cos\theta & 1 \end{bmatrix}. \quad \text{(A.15)}$$

.

Here θ is the angle that the axis is rotated by in direction according to the right hand grip rule.

The spot is initially positioned at the time of central meridian passing t_{CM} but with the spot rotated so that it is at position (0,0,R_*). It is positioned here so that it is readily determined whether a point on the sphere is in the spot or not from the size of the projected radius of the spot R_s.

The first rotation is to rotate about the x-axis to move the spot to the correct latitude as seen by the observer in the plane of the sky. That position is at $(0_{,p}, \sqrt{(}R_*^2 - L_p^2)$ then we have to rotate by $-\theta_L$ degrees where

$$\theta_L = arcsin(L_p/R_*). \quad \text{(A.16)}$$

.

The second rotation is about the x-axis with angle -$(\frac{\pi}{2} - I)$ where I is the inclination

of the rotation axis of the star with respect to the observer. This rotation moves the y-axis so that it coincides with the stellar rotation axis. Next a rotation of angle ω about the y-axis is performed to allow for the movement of the spot due to stellar rotation. Here ω is

$$\omega = \frac{2\pi}{P}(mod(t - t_{CM}, P)), \tag{A.17}$$

where mod is the modulus function.

The fourth rotation is about the x-axis again by $(\frac{\pi}{2} - I)$ degrees in order to move back to the plane of the sky. Thus the relationship between a point on the sphere **X** = (x,y,z) in the frame where the spot is at the origin and the point **X'** = (x',y',z') in the plane of the sky frame at time t is given by

$$\mathbf{X}' = \mathbf{R}_x(\frac{\pi}{2} - I)\mathbf{R}_y(\omega)\mathbf{R}_x(I - \frac{\pi}{2})\mathbf{R}_x(-\theta_L)\mathbf{X} = \mathbf{A}\mathbf{X}, \tag{A.18}$$

where A is just the result of multiplying the 4 rotational matrices together.

The above equation permits us to determine where the spot is at a given time t. We can also use the inverse of the above equation to help us determine y_1 and y_2. The inverse of the above equation is

$$\mathbf{X} = \mathbf{A}^{-1}\mathbf{X}' = \mathbf{R}_x(\theta_L)\mathbf{R}_x(\frac{\pi}{2} - I)\mathbf{R}_y(-\omega)\mathbf{R}_x(I - \frac{\pi}{2})\mathbf{X}'. \tag{A.19}$$

Lets assume:

$$\mathbf{X}' = \{x_c, y_c, z_c\}, \tag{A.20}$$

where y_c will have the values y_1 and y_2 and where

$$\mathbf{X} = \{x_o, y_o, z_o\}, \tag{A.21}$$

and

$$\mathbf{A}^{-1} = \begin{bmatrix} a_{00} & a_{01} & a_{02} \\ a_{10} & a_{11} & a_{12} \\ a_{20} & a_{21} & a_{22} \end{bmatrix}. \tag{A.22}$$

In our forward model we have 4 free parameters which we will fit: t_{CM} the time of central meridian passing of the spot; R_S the radius of the spot; the latitude L_P of the spot and I the inclination of the stellar rotation axis. Given the values for these parameters we can determine the values of the angles for the four rotations

and thus we can determine the contents of matrix A. The velocity x_c is known as that is the value we want to find the corresponding two values of y_c for.

Expanding equation A.18 we have

$$z_c = (x_o - a_{00}x_c - a_{01}y_c)/a_{02}, \tag{A.23}$$

$$y_o = a_{10}x_c + a_{11}y_c + a_{12}z_c, \tag{A.24}$$

$$z_o = a_{20}x_c + a_{21}y_c + a_{22}z_c. \tag{A.25}$$

Now as $\mathbf{X}$ has to lie on circumference of spot with radius R_s we have

$$x_o^2 + y_o^2 = R_s^2, \tag{A.26}$$

and given that we assume radius of star is 1 we also have

$$x_o^2 + y_o^2 + z_o^2 = 1. \tag{A.27}$$

So from equations A.26 and A.27 we have

$$z_o = \sqrt{1 - R_s^2}. \tag{A.28}$$

Here we take the +ve square root for z_o as spot is visible to the observer at the time of central meridian passage. Multiply equation A.23 by a_{12} to get

$$a_{12}x_o = a_{12}a_{00}x_c + a_{12}a_{01}y_c + a_{12}a_{02}z_c. \tag{A.29}$$

Multiply equation A.24 by a_{02}

$$a_{02}y_o = a_{02}a_{10}x_c + a_{02}a_{11}y_c + a_{02}a_{12}z_c. \tag{A.30}$$

Subtract A.30 from A.29

$$a_{12}x_o - a_{02}y_o = Ax_c + By_c, \tag{A.31}$$

where

$$A = a_{12}a_{00} - a_{02}a_{10}, \tag{A.32}$$

and

$$B = a_{12}a_{01} - a_{02}a_{11}. \tag{A.33}$$

Multiply equation A.23 by a_{22}

$$a_{22}x_o = a_{22}a_{00}x_c + a_{22}a_{01}y_c + a_{22}a_{02}z_c. \tag{A.34}$$

Multiply equation A.25 by a_{02}

$$a_{02}z_o = a_{02}a_{20}x_c + a_{02}a_{21}y_c + a_{02}a_{22}z_c. \tag{A.35}$$

Subtract A.35 from A.34

$$a_{22}x_o - a_{02}z_o = Cx_c + Dy_c, \tag{A.36}$$

where

$$C = a_{22}a_{00} - a_{02}a_{20}, \tag{A.37}$$

and

$$D = a_{22}a_{01} - a_{02}a_{21}. \tag{A.38}$$

Multiply equation A.24 by a_{22}

$$a_{22}y_o = a_{22}a_{10}x_c + a_{22}a_{11}y_c + a_{22}a_{12}z_c. \tag{A.39}$$

Multiply equation A.25 by a_{12}

$$a_{12}z_o = a_{12}a_{20}x_c + a_{12}a_{21}y_c + a_{12}a_{22}z_c. \tag{A.40}$$

Subtract A.40 from A.39

$$a_{22}y_o - a_{12}z_o = Ex_c + Fy_c, \tag{A.41}$$

where

$$E = a_{22}a_{10} - a_{12}a_{20}, \tag{A.42}$$

and

$$F = a_{22}a_{11} - a_{12}a_{21}. \tag{A.43}$$

Multiply A.31 by D

$$Da_{12}x_o - Da_{02}y_o = DAx_c + DBy_c. \tag{A.44}$$

Multiply A.36 by B

$$Ba_{22}x_o - Ba_{02}z_o = BCx_c + BDy_c. \tag{A.45}$$

Subtract A.45 from A.44

$$(Da_{12} - Ba_{22})x_o - Da_{02}y_o + Ba_{02}z_o = (DA - BC)x_c. \tag{A.46}$$

Square above equation

$$(Da_{12} - Ba_{22})^2 x_o^2 = [(DA - BC)x_c + Da_{02}y_o - Ba_{02}z_o]^2. \tag{A.47}$$

Aim now is to rearrange above equation into a quadratic equation in terms of y_o

$$(Da_{12} - Ba_{22})^2(R_s^2 - y_o^2) = [Da_{02}y_o + [(DA - BC)x_c - Ba_{02}z_o]]^2, \tag{A.48}$$

$$\begin{aligned}[D^2a_{02}^2 + (Da_{12} - Ba_{22})^2]y_o^2 + 2[(DA - BC)x_c - Ba_{02}z_o]Da_{02}y_o \\ + [(DA - BC)x_c - Ba_{02}z_o]^2 - (Da_{12} - Ba_{22})^2R_s^2 = 0.\end{aligned} \tag{A.49}$$

Simplifying with constants for the coefficients in the quadratic we have

$$Gy_o^2 + Hy_o + I = 0, \tag{A.50}$$

where

$$G = [D^2a_{02}^2 + (Da_{12} - Ba_{22})^2], \tag{A.51}$$

$$H = 2[(DA - BC)x_c - Ba_{02}z_o]Da_{02}, \tag{A.52}$$

$$I = [(DA - BC)x_c - Ba_{02}z_o]^2 - (Da_{12} - Ba_{22})^2R_s^2. \tag{A.53}$$

Solving equation A.50 we have:

$$y_o = \frac{-H \pm \sqrt{H^2 - 4GI}}{2G}. \tag{A.54}$$

So this gives us up to two real values of y_o say y_{o1} and y_{o2}. Zero real values correspond to the spot not being at that value of x_c. One real value corresponds to the spot being tangential to the given value of x_c. Two real values corresponds to the spot being intersected by the plane parallel to the z-axis with constant x-component x_c. This two value solution is the solution of interest.

Given the two values for y_{o1} and y_{o2} we can calculate the corresponding pair of values for x_o (x_{o1} and x_{o2}) and the single value of z_o. From equation A.26 we can determine the absolute value of x_{o1} and x_{o2} (we don't however know which sign to use from the square root). Knowing this we can then determine z_o1 and z_{o2} from equation A.27 remembering we have to use the positive root for z_o1 and z_o2. Finally we get the values for x_{o1} and x_{o2} using equation A.46 and then the two values of y_c (y_{c1} and y_{c2}) from equation A.44.

Thus for a given value of x_c at time t which we have the two solutions

$$\begin{aligned}(x_{o1}, y_{o1}, z_o) &\mapsto (x_c, y_{c1}, z_{c1}),\\ (x_{o2}, y_{o2}, z_o) &\mapsto (x_c, y_{c2}, z_{c2}).\end{aligned} \tag{A.55}$$

This solution tells us that points on the edge of the spot are at x_c. We have to determine if for the given x_c the region of the spot with that x-coordinate is completely visible, partially visible or not visible at all to the observer in the plane of the sky.

We determine if these points on the edge of the spot are visible to the observer from the sign of z_{c1} and z_{c2}. If the sign is positive then they are visible otherwise they are not visible to the observer.

We have three cases which I will consider in turn: 0,1, or 2 edges of the spot visible.

Zero edges of spot visible implies that either the spot is not visible at x_c or is visible all along the chord at x_c. To determine this we check whether the spot is visible at the edges of the star at the points $(x_c, \pm\sqrt{(}1 - x_c^2, 0)$

$$u = (x_u, y_u, z_u) = \mathbf{A}^{-1}(x_c, +\sqrt{1 - x_c^2}, 0), \tag{A.56}$$

and

$$l = (x_l, y_l, z_l) = \mathbf{A}^{-1}(x_c, -\sqrt{1 - x_c^2}, 0). \tag{A.57}$$

If both u and l have z-coord greater than equal to 0 and $x_u^2 + y_u^2 < R_s^2$ and $x_l^2 + y_l^2 < R_s^2$ then y_1 and y_2 is $-\sqrt{1 - x_c^2}, 0$ and $+\sqrt{1 - x_c^2}, 0$ respectively.

In the second case then we will have the solution $y_1 = -\sqrt{1 - x_c^2}, 0, y_2 = y_{c2}$ if l is in the spot. Otherwise solution is $y_1 = y_{c1}, y_2 = \sqrt{1 - x_c^2}, 0$ if u is in the spot.

The final case is when both edges of spot are visible. In this case $y_1 = y_{c1}$ and $y_2 = y_{c2}$.

If the spot is small ($R_s << R_*$) then we could avoid performing the convolution in equation A.9 which will save a significant amount of computer processing time. Instead we perform the following:

$$S_{R,spot}(v) = (\frac{1}{\int_\infty^\infty G'(v')dv'}[(S * G')(v) - (1 - \Gamma)WS(v + v_s)] \tag{A.58}$$

where v_s is the velocity (position) of the spot which can be determined by taking the first moment of D(v) and W is the area of the spot.

We can now perform dLSD on the forward model to determine the model kernel residuals K_m from the following convolution

$$S_{R,spot} - S_{R,nospot} = K_m * S_{R,nospot}. \tag{A.59}$$

A Bayesian analysis can then be performed in an analogous way to that described in Strachan & Anglada-Escudé (2017) but this time we determine the posterior probability distributions of the four free parameters in the spot forward model using the kernel residuals derived from the HARPS and CARMENES spectra.

We can also use the forward model to determine the Doppler velocity shift caused by the spot and also to estimate the change in relative flux caused by the spot which will be able to provide a light curve which we can compare with our photometry. A relatively simple way to do this is to use equation A.9. This equation involves a convolution S of our rotationally unbroadened template spectra with a kernel G' - (1-Γ)D which caters for the spot and the rotationally broadening to produce our model spectrum. It is firstly obvious that the information relating to the Doppler shift and the relative flux lies solely in this kernel. Given the properties of the convolution operator where flux is conserved if the kernel is normalised and reduced proportionately when the kernel is reduced (due to subtracting the spot D) this means that we can determine the relative flux by taking the zeroth velocity moment of the kernel. Thus we have

$$F_m(t) = \int_{-\infty}^{\infty} G'(v)dv - \int_{-\infty}^{\infty} (1-\Gamma)Ddv, \tag{A.60}$$

where the suffix m stands for a flux derived from the forward model. We then define the standard flux value as

$$F_{m,standard} = max\{F_m(t) : t \in T\}, \tag{A.61}$$

where T is the set of observation times from the photometry.

Finally we define the normalised model flux as

$$\hat{F}_m(t) = \frac{F_m(t)}{F_{m,standard}}. \tag{A.62}$$

We can similarly determine the velocity shift by calculating the first velocity moment of the normalised kernel

$$v_{shift}(t) = \int_{-\infty}^{\infty} \frac{G' - (1-\Gamma)D}{\int_{-\infty}^{\infty} G' - (1-\Gamma)Ddv'} vdv. \tag{A.63}$$

A.2. Data Tables

Table A.1.: Radial velocities and indicator values for the HARPS Red Dots spectra.

BJD (days)	**RV (ms^{-1})**	σ**(ms^{-1})**	**FWHM**	**Halpha**	**CCF BIS**	**RHK**
2457934.67135	-9.175	2.089	4.165	-2.391	-7.47	10.847
2457935.67347	-7.59	2.917	4.139	-2.732	12.575	11.79
2457936.63890	7.934	1.64	4.191	-2.61	9.523	11.383
2457937.65955	-12.264	1.967	4.161	-2.969	20.198	11.595
2457942.60497	-7.05	1.256	4.193	-2.266	5.244	9.97
2457943.59327	8.011	2.138	4.119	-2.313	7.742	8.469
2457944.57569	13.089	1.462	4.114	-2.614	0.419	12.552
2457945.62243	-16.546	1.447	4.164	-1.911	11.054	9.95
2457946.75065	13.654	2.036	4.155	-2.32	-4.591	11.191
2457948.67162	-9.978	3.504	4.165	-2.988	20.763	15.141
2457949.69978	4.212	4.307	4.152	-1.683	-6.191	9.866
2457951.68486	-7.446	2.711	4.145	-2.526	4.155	13.126
2457952.67349	-8.586	2.427	4.143	-2.288	10.755	12.011
2457953.72408	11.479	1.737	4.172	-2.259	-26.128	11.521
2457954.64622	-8.698	1.945	4.148	-3.7	0.915	19.507
2457955.65790	-14.952	2.983	4.146	-2.282	-3.837	11.807
2457956.68534	5.542	2.163	4.191	-2.583	-7.204	13.207
2457958.76172	0.768	3.351	4.12	-2.317	11.068	14.133
2457959.64293	-9.733	2.552	4.2	-2.139	2.364	10.747
2457960.66738	-2.359	2.635	4.126	-3.861	-1.51	20.247
2457961.65259	12.594	1.536	4.1	-1.788	-13.18	9.371
2457962.64176	-12.944	2.341	4.17	-2.637	12.971	13.008
2457964.65368	24.056	2.002	4.123	-2.262	-34.235	10.524
2457965.66280	-21.262	2.559	4.137	-2.39	13.942	11.503
2457966.65112	6.653	2.157	4.152	-2.551	0.653	14.082
2457967.57875	29.047	5.416	4.172	-1.775	-20.571	9.421
2457968.51069	-23.44	2.73	4.156	-1.955	15.18	10.411
2457969.65084	-3.732	2.651	4.145	-2.385	16.693	10.668
2457970.65314	2.709	4.333	4.185	-2.114	-24.444	8.212
2457971.64075	-19.067	2.417	4.162	-2.062	11.904	10.177
2457972.66246	-18.233	2.045	4.14	-1.954	13.165	9.642
2457973.66388	15.065	2.104	4.174	-2.247	0.182	11.542
2457974.66267	-9.756	1.974	4.143	-2.029	9.153	9.794
2457979.72386	-14.643	1.669	4.179	-2.555	14.577	12.399
2457980.62705	7.502	2.178	4.144	-2.061	1.867	10.287
2457981.73145	13.296	7.16	4.099	-2.016	-38.162	12.129
2457984.53772	18.035	2.266	4.119	-1.924	-25.124	9.906
2457985.53620	-21.237	1.804	4.187	-2.287	20.681	11.866
2457986.54687	9.178	1.786	4.144	-2.299	-2.346	11.245
2457987.55833	22.835	1.794	4.145	-1.893	-18.007	10.024
2457990.52181	29.114	2.105	4.163	-2.426	-11.241	11.851
2457991.54399	-19.771	3.205	4.134	-2.627	21.611	14.247
2457992.53615	-18.005	0.942	4.15	-1.676	6.368	8.967
2457993.52061	16.113	1.579	4.171	-1.865	-4.775	9.571

Table A.1.: *continued* Radial velocities and indicator values for the HARPS Red Dots spectra.

BJD (days)	**RV (ms^{-1})**	**$\sigma(ms^{-1})$**	**FWHM**	**Halpha**	**CCF BIS**	**RHK**
2457994.507	-16.538	1.659	4.131	-2.199	9.541	11.135
2457995.513	-26.431	1.606	4.136	-2.778	15.698	14.833
2457996.516	8.441	2.232	4.172	-3.542	-9.06	15.453
2457998.546	-13.3	1.514	4.091	-1.77	10.294	9.283
2458000.545	11.037	2.379	4.142	-2.538	-6.516	12.618
2458001.551	-2.545	1.753	4.093	-2.229	-11.694	11.039
2458002.54	-8.191	1.548	4.174	-2.262	0.572	10.907
2458007.56	22.989	2.685	4.162	-1.819	-20.468	9.572
2458008.625	-21.74	2.926	4.139	-2.086	13.09	11.654
2458010.564	21.828	2.26	4.159	-1.632	-27.851	9.654
2458011.655	1.175	2.086	4.104	-2.206	-5.934	12.599
2458012.651	-24.826	3.233	4.111	-1.936	8.905	11.312
2458013.634	13.112	2.695	4.161	-2.042	-5.461	10.96
2458017.499	11.823	2.521	4.143	-2.592	-11.149	12.315
2458018.542	-10.706	1.792	4.084	-1.694	1.941	9.446
2458019.509	3.326	1.639	4.165	-1.956	-10.146	9.362
2458020.514	10.278	1.371	4.163	-1.885	9.575	10.471
2458021.492	3.865	2.161	4.089	-1.469	0.825	8.86
2458022.492	-11.212	2.226	4.19	-2.078	-3.438	10.686
2458023.494	0	3.059	4.178	-2.117	5.274	10.203
2458024.594	22.743	1.984	4.099	-1.718	-16.07	9.203
2458025.503	-18.467	2.843	4.155	-2.374	8.292	12.478
2458026.508	-17.588	2.872	4.154	-2.197	8.522	10.517
2458027.51	31.699	5.436	4.144	-2.398	-11.012	11.343

Table A.2.: Radial velocities and indicator values for the CARMENES spectra.

BJD (days)	**RV** (ms^{-1})	$\sigma(ms^{-1})$	**CRX index**	**DLW index**
2457948.48971	-12.346	3.578	70.282	20.343
2457949.51921	9.978	2.492	21.074	-25.85
2457950.48571	17.723	2.878	9.187	-1.954
2457951.50206	-10.615	4.634	87.6	-14.45
2457958.45854	-10.346	2.751	70.397	-15.466
2457960.47813	-3.539	3.009	40.794	-12.813
2457961.45536	-0.956	3.901	64.673	-42.999
2457962.44529	-2.938	2.713	53.559	35.315
2457963.45001	9.87	2.529	7.385	-8.235
2457964.44088	9.196	2.733	-7.12	-33.848
2457965.44389	-9.653	2.521	62.703	34.041
2457968.43935	-16.72	2.878	32.604	25.386
2457975.41861	-12.168	3.299	68.506	5.618
2457976.41040	17.47	3.17	26.304	22.588
2457977.41606	-11.409	2.557	37.834	1.436
2457979.44959	5.302	3.37	10.067	25.589
2457981.37796	-11.879	3.009	64.161	-39.399
2457982.39809	1.335	2.548	4.065	29.76
2457985.43401	-10.175	2.06	3.743	15.818
2457986.38238	8.7	2.293	-12.363	-23.866
2457987.41845	15.281	2.415	-65.838	-26.098
2457989.36370	4.073	3.087	-49.266	-23.918
2457990.41684	21.745	2.581	-58.858	0.008
2457993.42603	8.769	12.655	-97.79	48.684
2458002.34701	8.019	2.714	-6.309	26.361
2458005.33001	-1.223	3.153	-23.622	30.006
2458006.33201	2.053	4.779	-124.663	-10.389
2458007.32861	7.339	2.943	-46.494	-29.337
2458008.39012	-18.982	2.947	4.404	33.718
2458009.34389	-4.742	2.565	-32.432	-1.491
2458010.31598	22.286	2.872	-68.749	-21.775
2458017.31393	-8.351	2.746	-28.78	-6.388
2458018.30620	-18.256	6.64	-163.843	-48.518
2458022.29375	5.588	2.748	-29.826	20.768
2458023.39601	-2.483	4.386	-104.233	-1.553
2458029.29325	-7.978	3.451	-4.982	-6.252
2458033.28846	28.262	4.093	-116.938	-9.326

Table A.3.: m2 and m3 moments for the HARPS spectra.

BJD (days)	m2	m2 error	m3	m3 error
2457934.67135	6.446	0.052	-0.770	0.668
2457935.67347	6.428	0.076	-0.635	0.975
2457936.63890	6.681	0.051	0.384	0.681
2457937.65955	6.492	0.051	-0.665	0.652
2457942.60497	7.014	0.044	-0.535	0.599
2457943.59327	6.849	0.049	0.734	0.667
2457944.57569	6.808	0.051	0.929	0.683
2457945.62243	6.687	0.038	-0.968	0.505
2457946.75065	6.419	0.045	0.696	0.576
2457948.67162	6.354	0.099	-1.477	1.246
2457949.69978	6.233	0.082	0.558	1.016
2457951.68486	6.497	0.080	-0.921	1.040
2457952.67349	6.544	0.059	-0.774	0.765
2457953.72408	6.783	0.052	1.032	0.690
2457954.64622	6.546	0.051	-0.694	0.665
2457955.65790	6.525	0.085	-0.635	1.111
2457956.68534	6.929	0.071	1.180	0.962
2457958.76172	6.547	0.108	-0.229	1.408
2457959.64293	6.966	0.077	-0.291	1.053
2457960.66738	6.915	0.083	0.291	1.137
2457961.65259	6.316	0.034	0.873	0.432
2457962.64176	6.854	0.060	-1.114	0.807
2457964.65368	6.688	0.051	1.527	0.665
2457965.66280	6.716	0.069	-1.420	0.915
2457966.65112	6.547	0.059	0.972	0.766
2457967.57875	6.517	0.090	1.997	1.143
2457968.51069	6.730	0.078	-1.416	1.040
2457969.65084	6.936	0.092	-0.448	1.278
2457970.65314	11.368	0.196	1.916	4.194
2457971.64075	6.840	0.072	-1.856	0.960
2457972.66246	6.406	0.044	-1.187	0.546
2457973.66388	6.884	0.061	1.752	0.833
2457974.66267	6.519	0.050	-0.396	0.658
2457979.72386	6.949	0.050	-0.937	0.687
2457980.62705	6.628	0.060	0.960	0.773
2457981.73145	6.676	0.114	1.710	1.517
2457984.53772	6.485	0.062	0.907	0.797
2457985.53620	6.885	0.053	-1.346	0.714
2457986.54687	6.672	0.046	0.436	0.609
2457987.55833	6.516	0.041	1.852	0.524
2457990.52181	6.559	0.049	2.258	0.635
2457991.54399	6.631	0.083	-1.447	1.073
2457992.53615	6.587	0.037	-1.771	0.483

Table A.3.: *continued* m2 and m3 moments for the HARPS spectra.

BJD (days)	**m2**	**m2 error**	**m3**	**m3 error**
2457993.52061	6.718	0.047	1.397	0.616
2457994.50692	6.607	0.049	-0.872	0.631
2457995.51275	6.581	0.050	-2.183	0.652
2457996.51609	6.913	0.056	0.564	0.764
2457998.54607	6.381	0.040	-0.768	0.498
2458000.54549	6.816	0.067	0.864	0.904
2458001.55061	6.334	0.043	-0.620	0.549
2458002.54048	6.969	0.048	-0.859	0.661
2458007.56015	6.527	0.074	2.008	0.954
2458008.62514	6.676	0.085	-1.546	1.117
2458010.56353	6.640	0.062	1.463	0.801
2458011.65456	6.375	0.057	0.305	0.722
2458012.65073	6.437	0.078	-1.786	0.979
2458013.63396	6.754	0.068	1.623	0.899
2458017.49889	6.621	0.068	0.770	0.891
2458018.54176	6.415	0.046	-0.469	0.594
2458019.50854	6.953	0.042	0.364	0.571
2458020.51380	6.569	0.051	0.356	0.663
2458021.49173	6.217	0.053	0.575	0.659
2458022.49174	7.201	0.084	-1.985	1.176
2458023.49424	6.822	0.089	-0.186	1.200
2458024.59385	6.525	0.051	1.917	0.655
2458025.50309	7.339	0.082	-2.055	1.172
2458026.50818	6.652	0.072	-1.327	0.937
2458027.50998	6.262	0.103	1.158	1.293

Table A.4.: m2 and m3 moments for the CARMENES spectra.

BJD (days)	m2	m2 error	m3	m3 error
2457948.48971	7.022	0.984	3.185	14.059
2457949.51921	6.422	0.441	-0.341	5.493
2457950.48571	6.544	0.398	-4.364	4.764
2457951.50206	6.237	2.59	1.187	32.948
2457953.49437	5.881	3.263	-7.011	39.473
2457958.45854	6.277	0.434	2.916	5.017
2457960.47813	6.589	0.4	0.979	4.764
2457961.45536	6.097	0.813	0.787	8.913
2457962.44529	7.393	0.521	-0.398	7.768
2457963.45001	6.781	0.458	-1.246	6.12
2457964.44088	6.318	0.404	-1.089	5.799
2457965.44389	7.229	0.419	3.589	5.761
2457968.43935	6.803	0.712	6.318	8.985
2457974.40784	6.707	0.55	3.435	6.794
2457975.41861	6.494	0.72	3.677	9.554
2457976.41040	6.923	0.701	-4.797	8.692
2457977.41606	6.638	0.291	1.543	3.612
2457979.44959	6.92	0.564	-3.112	7.77
2457981.37796	6.09	0.474	2.653	5.54
2457982.39809	7.276	0.372	-0.23	4.765
2457986.38238	6.365	0.247	-0.902	3.018
2457987.41845	6.346	0.416	-1.931	5.525
2457989.36370	6.457	0.563	-0.166	7.361
2457990.41684	6.593	0.393	-2.846	4.944
2457993.42603	2.481	5.536	-2.882	34.38
2458007.32861	6.142	0.732	-0.516	8.545
2458008.39012	6.992	0.476	5.575	6.11
2458009.34389	6.677	0.362	1.397	4.86
2458010.31598	6.289	0.309	-3.102	4.015
2458017.31393	6.577	0.245	1.93	3.309
2458018.30620	5.788	3.764	3.194	40.851
2458022.29375	7.074	0.309	0.193	4.262
2458029.29325	6.694	0.539	2.098	6.612
2458033.28846	6.278	0.419	-2.518	4.808
2458034.28588	6.624	0.457	4.666	5.73

Table A.5.: Input Params for Forward Model

Parameter	Value	Units	Reference
Teff	3548 ± 68	K	Maldonaldo 2015
[Fe/H]	-0.06 ± 0.1	dex	Maldonaldo 2015
log g	4.8 ± 0.05	cgs	Maldonaldo 2015
HARPS min λ	553.0	nm	this document
HARPS max λ	691.3	nm	this document
u_1 for HARPS	0.485 ± 0.012		this document
u_2 for HARPS	0.267 ± 0.017		this document
CARMENES min λ	561.7	nm	this document
CARMENES max λ	919.7	nm	this document
u_1 for CARMENES	0.310 ± 0.007		this document
u_2 for CARMENES	0.312 ± 0.011		this document

Table A.6.: Mean and one sigma errors for the fitted parameters for the black spot forward model using the HARPS Red Dots spectra with period 2.87 days.

Parameter	**Value**	σ	**units**
t_{CM}	2457933.60992	0.00439	BJD
R_s	0.35212	0.00249	R_*
L_P	1.00000	0.005	R_*
cos(I)	-0.22699	0.00273	

Table A.7.: Mean and one sigma errors for the fitted parameters for the black spot forward model using the CARMENES Red Dots spectra with period 2.87 days.

Parameter	**Value**	σ	**units**
t_{CM}	2457933.6146	0.0036	BJD
R_s	0.138	0.011	R_*
L_P	0.938	0.020	R_*
cos(I)	-0.197	0.030	

B. Appendix for Chapter 4

B.1. Flux and Doppler shift of reflected light from hot Jupiters

Here we determine the flux and Doppler shift of the reflected light arriving at Earth from a tidally locked hot Jupiter in a circular orbit, The geometry we use to determine this is shown in Figure 5.3.

We use two main coordinate systems. The first is the Cartesian coordinate system $X_pY_pZ_P$ centred on the planet where the Z_P axis is pointing towards the Earth and the X_p and Y_p axis in the plane of the sky as viewed from the Earth. We use a colatitude coordinate system $(\vartheta_p, \phi_p, R_p)$ to describe the location of points on the surface of the planet.

In order to determine the reflected starlight arriving at the Earth we first determine the starlight incident at each point (ϑ_p, ϕ_p) on the surface of the planet.

For this we use a second stellar Cartesian coordinate system $X_*Y_*Z_*$ centred on the star and which has Z_* axis pointing towards (ϑ_p, ϕ_p) as shown in Figure 5.3. This stellar coordinate system also has its associated colatitude system $(\vartheta_*, \phi_*, R_*)$ in order to describe points on the surface of the star. Let d be the distance between C_P and the centre of the star. C_P is the point $(R_p \cos\phi_p \sin\vartheta_p,\ R_p \sin\phi_p \sin\vartheta_p, R_p \cos\vartheta_p)$ in the planet frame. In this frame we assume we have that $O_* = (x_*, y_*, z_*)$ and we can determine d as follows.

Angle $C_p\hat{O}_pO_* = \gamma$ is

$$\cos(\gamma) = \cos\phi_p \sin\vartheta_p \frac{x_*}{a} + \sin\phi_p \sin\vartheta_p \frac{y_*}{a} + \cos\vartheta_p \frac{z_*}{a}. \tag{B.1}$$

Using the cosine rule we have

$$d^2 = a^2 + R_p^2 - 2aR_p \cos\gamma, \tag{B.2}$$

and we can now determine $\tan\omega$ as

$$\tan\omega = \frac{R_* \sin\vartheta_*}{d - R_* \cos\vartheta_*}. \tag{B.3}$$

$\sin\omega$ and $\cos\omega$ and their implicit differentials are

$$\sin\omega = \frac{R_* \sin\vartheta_*}{\sqrt{R_*^2 + d^2 - 2R_* d\cos\vartheta_*}}, \tag{B.4}$$

$$\cos\omega \; dw = \left(\frac{R_* \cos\vartheta_*}{\sqrt{R_*^2 + d^2 - 2dR_*\cos\vartheta_*}} - \frac{R_*^2 d \sin^2\vartheta_*}{(R_*^2 + d^2 - 2dR_*\cos\vartheta)^{3/2}} \right) d\vartheta_*, \tag{B.5}$$

$$\cos\omega = \frac{d - R_* \cos\vartheta_*}{\sqrt{R_*^2 + d^2 - 2R_* d\cos\vartheta_*}}, \tag{B.6}$$

$$\sin\omega \;\; d\omega \;\; = \;\; \frac{-R_* \sin\vartheta_*}{\sqrt{R_*^2 + d^2 - 2R_*\, d\cos\vartheta_*}} + \frac{R_* d \sin\vartheta_* (d - R_*\cos\vartheta_*)}{(R_*^2 + d^2 - 2dR_*\cos\vartheta)^{3/2}} \;\; d\vartheta_*. \tag{B.7}$$

The solid angle of the star subtended by the planet cell is

$$\Omega_{\theta_p\phi_p} = \int_0^{2\pi} \int_0^{\tan^{-1}\left(\frac{R_*}{d}\right)} \sin\omega \; d\omega \; d\phi_* - \text{ blocked portion.} \tag{B.8}$$

The blocked portion of the solid angle is the portion where light cannot travel to the planet cell due to some part of the star or planet being in its path. In order to take account of this when we calculate the integral numerically for each element we check whether

$$0 \leq \hat{\sigma} \cdot \hat{n}_* < 1, \tag{B.9}$$

and

$$0 \leq -\hat{\sigma} \cdot \hat{n}_p < 1. \tag{B.10}$$

If the light is blocked then at least one of the two inequalities will not hold and instead of using the $\sin\omega$ factor in the integral we use 0 instead.

The flux at the point (ϑ_p, ϕ_p) of the planet from the star is

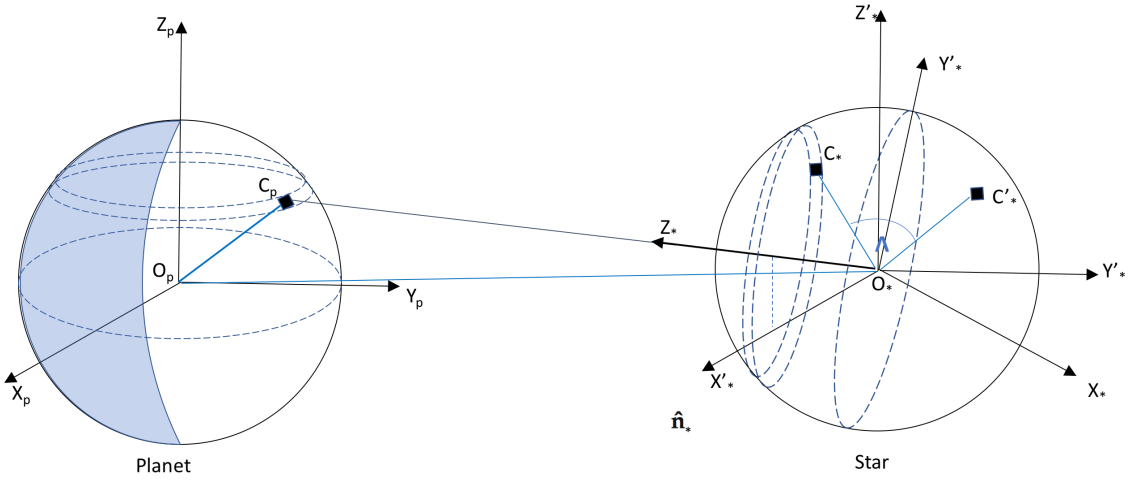

Figure B.1.: Geometry showing the rotation from the original star frame $X'_*Y'_*Z'_*$ to the frame $X_*Y_*Z_*$ where the Z_* axis points towards the planet cell C_p.

$$F_{\vartheta_p\phi_p}(\nu) = \int_0^{2\pi} \int_0^{\tan^{-1}\left(\frac{R_*}{d}\right)} I_*(\vartheta_*, \phi_*, \nu - \nu_*, t) \\ (-\hat{n}_p \cdot \sigma) \sin\omega \; d\omega \; d\phi_*, \quad \text{(B.11)}$$

where ν_* is the frequency Doppler shift due to the motion of the star cell.

We have to work out the dot product $(\hat{n}_p \cdot \sigma)$ which is complicated by the fact that currently we only know the position of the cell C_* in the coords of the star $(R_* \cos\phi_* \sin\vartheta_*,\ R_* \sin\phi_* \sin\vartheta_*, R_* \cos\vartheta_*)_*$.

In order to move to the planet frame from the star frame we have two rotations in order to align the Z_* axis and a translation to perform (see Figure B.1).

In terms of vectors we have

$$\overrightarrow{O_pC_*} = \overrightarrow{O_pO_*} + \overrightarrow{O_*C_*} = \overrightarrow{O_*C_*} + \mathbf{R}_x(-\Lambda_x)\mathbf{R}_y(-\Lambda_y)\overrightarrow{O_*C'_*}, \quad \text{(B.12)}$$

where $\mathbf{R}_x$ and $\mathbf{R}_y$ are rotation matrices about the X and Y axis respectively and the angles Λ_x and Λ_y are the angles so that the rotations $\mathbf{R}_y(\Lambda_y)\mathbf{R}_x(\Lambda_x)$ move the Z_p axis to be in the same direction as the Z_* axis.

In component form we have

$$\begin{bmatrix} C_{*x} \\ C_{*y} \\ C_{*z} \end{bmatrix}_p = \Big[\mathbf{R}_x(-\Lambda_x)\mathbf{R}_y(-\Lambda_y)\Big] \begin{bmatrix} R_* \cos\phi_* \sin\vartheta_* \\ R_* \sin\phi_* \sin\vartheta_* \\ R_* \cos\vartheta_* \end{bmatrix}_* + \begin{bmatrix} x_* \\ y_* \\ z_* \end{bmatrix}_p . \tag{B.13}$$

The subscripts on the matrix correspond to the Cartesian coordinate frame the components are in (p for planet and * for star).

Expanding out the rotation matrices we have

$$\begin{bmatrix} C_{*x} \\ C_{*y} \\ C_{*z} \end{bmatrix}_p = \begin{bmatrix} \cos\Lambda_y & 0 & -\sin\Lambda_y \\ \sin\Lambda_x \sin\Lambda_y & \cos\Lambda_x & \sin\Lambda_x \cos\Lambda_y \\ \cos\Lambda_x \sin\Lambda_y & -\sin\Lambda_x & \cos\Lambda_x \cos\Lambda_y \end{bmatrix} \begin{bmatrix} R_* \cos\phi_* \sin\vartheta_* \\ R_* \sin\phi_* \sin\vartheta_* \\ R_* \cos\vartheta_* \end{bmatrix}_* + \begin{bmatrix} x_* \\ y_* \\ z_* \end{bmatrix}_p . \tag{B.14}$$

Expanding out the components we have

$$C_{*x} = \cos\Lambda_y R_* \cos\phi_* \sin\vartheta_* - \sin\Lambda_y R_* \cos\vartheta_* + x_*, \tag{B.15}$$

$$C_{*y} = \sin\Lambda_x \sin\Lambda_y R_* \cos\phi_* \sin\vartheta_* + \cos\Lambda_x R_* \sin\phi_* \sin\vartheta_* + \sin\Lambda_x \cos\Lambda_y R_* \cos\vartheta_* + y_*, \tag{B.16}$$

$$C_{*z} = \cos\Lambda_x \sin\Lambda_y R_* \cos\phi_* \sin\vartheta_* - \sin\Lambda_x R_* \sin\phi_* \sin\vartheta_* + \cos\Lambda_x \cos\Lambda_y R_* \cos\vartheta_* + z_*. \tag{B.17}$$

We determine the components of $\sigma = (\sigma_x, \sigma_y, \sigma_z)^T$ as

$$\sigma_x = R_p \cos\phi_p \sin\vartheta_p - (\cos\Lambda_y R_* \cos\phi_* \sin\vartheta_* - \sin\Lambda_y R_* \cos\vartheta_* + x_*), \tag{B.18}$$

$$\sigma_y = R_p \sin\phi_* \sin\vartheta_p - (\sin\Lambda_x \sin\Lambda_y R_* \cos\phi_* \sin\vartheta_* + \cos\Lambda_x R_* \sin\phi_* \sin\vartheta_* + \sin\Lambda_x \cos\Lambda_y R_* cos\vartheta_* + y_*), \quad \text{(B.19)}$$

$$\sigma_z = R_p \cos\vartheta_p - (\cos\Lambda_x \sin\Lambda_y R_* \cos\phi_* \sin\vartheta_* - \sin\Lambda_x R_* \sin\phi_* \sin\vartheta_* + \cos\Lambda_x \cos\Lambda_y R_* \cos\vartheta_* + z_*). \quad \text{(B.20)}$$

The unit vector in the direction of σ is defined as

$$\hat{\sigma} = \frac{1}{s}\sigma, \quad \text{(B.21)}$$

where s is the distance between the cells C_p and C_* (the square root of the sum of squares of the components of σ given above).

The unit vector normal to the planet cell $\hat{n}_p$ is

$$\hat{\mathbf{n}}_p = \begin{bmatrix} \cos\phi_p \sin\vartheta_p \\ \sin\phi_p \sin\vartheta_p \\ \cos\vartheta_p \end{bmatrix}_p . \quad \text{(B.22)}$$

The dot product of the two unit vectors is

$$\begin{aligned}\hat{\sigma}.\hat{n}_p = \frac{1}{s}\{&\cos\phi_p \sin\vartheta_p [R_p \cos\phi_p \sin\vartheta_p \\ &- (\cos\Lambda_y R_* \cos\phi_* \sin\vartheta_* - \sin\Lambda_y R_* \cos\vartheta_* + x_*)] + \\ &\sin\phi_p \sin\vartheta_p [R_p \sin\phi_* \sin\vartheta_p - (\sin\Lambda_x \sin\Lambda_y R_* \cos\phi_* \sin\vartheta_* \\ &+ \cos\Lambda_x R_* \sin\phi_* \sin\vartheta_* + \sin\Lambda_x \cos\Lambda_y R_* \cos\vartheta_* + y_*)] \\ &+ \cos\vartheta_p [R_p \cos\vartheta_p - (\cos\Lambda_x \sin\Lambda_y R_* \cos\phi_* \sin\vartheta_* \\ &- \sin\Lambda_x R_* \sin\phi_* \sin\vartheta_* + \cos\Lambda_x \cos\Lambda_y R_* \cos\vartheta_* + z_*]\}. \quad \text{(B.23)}\end{aligned}$$

Now we determine the angles Λ_x and Λ_y. We use equation B.14 and set the position of the star cell to be in the direction of the Z'_* axis and we set it to unit length. When this axis is rotated it must be pointing towards the planet cell so we have

$$\frac{1}{q}\begin{bmatrix} C_{px}-x_* \\ C_{py}-y_* \\ C_{pz}-z_* \end{bmatrix}_p = \begin{bmatrix} \cos\Lambda_y & 0 & -\sin\Lambda_y \\ \sin\Lambda_x\sin\Lambda_y & \cos\Lambda_x & \sin\Lambda_x\cos\Lambda_y \\ \cos\Lambda_x\sin\Lambda_y & -\sin\Lambda_x & \cos\Lambda_x\cos\Lambda_y \end{bmatrix} \begin{bmatrix} 0 \\ 0 \\ 1 \end{bmatrix}_*, \tag{B.24}$$

where q is the normalising factor

$$q^2 = (R_p\cos\phi_p\sin\vartheta_p - x_*)^2 + (R_p\sin\phi_p\sin\vartheta_p - y_*)^2 + (R_p\cos\vartheta_p - z_*)^2. \tag{B.25}$$

Simplifying the equation we get

$$\frac{1}{q}\begin{bmatrix} R_p\cos\phi_p\sin\vartheta_p - x_* \\ R_p\sin\phi_p\sin\vartheta_p - y_* \\ R_p\cos\vartheta_p - z_* \end{bmatrix} = \begin{bmatrix} -\sin\Lambda_y \\ \sin\Lambda_x\cos\Lambda_y \\ \cos\Lambda_x\cos\Lambda_y \end{bmatrix}, \tag{B.26}$$

and from this we have

$$\Lambda_y = \sin^{-1}\left(\frac{x_* - R_p\cos\phi_p\sin\vartheta_p}{q}\right), \tag{B.27}$$

$$\Lambda_x = \sin^{-1}\left(\frac{R_p\sin\phi_p\sin\vartheta_p - y_*}{q\cos\Lambda_y}\right). \tag{B.28}$$

The flux arriving at the surface of the planet at the point $(\vartheta_p, \phi_p, R_p)$ is

$$F_{\vartheta_p\phi_p}(\nu) = \int_0^{2\pi}\int_0^{\pi/2} H(\vartheta_p, \phi_p, \vartheta_*, \phi_*, \nu - \Delta\nu_*, t)\, d\vartheta_*\, d\phi_*, \tag{B.29}$$

where $H(\vartheta_p, \phi_p, \vartheta_*, \phi_*, \nu, t)$ is zero when starlight is blocked from reaching the planet cell

$$H(\vartheta_p, \phi_p, \vartheta_*, \phi_*, \nu, t) = \begin{cases} 0, & \text{if } \hat{\sigma}\cdot\hat{n}_* < 0 \\ 0, & \text{if } -\hat{\sigma}\cdot\hat{n}_p < 0, \end{cases} \tag{B.30}$$

otherwise non-zero when:

$$H(\vartheta_p, \phi_p, \vartheta_*, \phi_*, \nu, t) = I_*(\vartheta_*, \phi_*, \nu, t)(-\hat{n}_p \cdot \hat{\sigma}) \left(\frac{-R_* \sin\vartheta_*}{\sqrt{R_*^2 + d^2 - 2R_* d\cos\vartheta_*}} + \frac{R_* d \sin\vartheta_* (d - R_*\cos\vartheta_*)}{(R_*^2 + d^2 - 2dR_*\cos\vartheta_*)^{3/2}} \right). \quad \text{(B.31)}$$

The intensity of the reflected light leaving the surface from the planet cell (θ_p, ϕ_p) in the direction of the Earth is

$$I_{s\vartheta_p\phi_p}(\nu) = \int_0^{2\pi} \int_0^{\pi/2} \rho(\vartheta_p, \phi_p, \vartheta_*, \vartheta_*) H(\vartheta_p, \phi_p, \vartheta_*, \phi_*, \nu - \Delta\nu, t)(\hat{n}_p \cdot \hat{k})\, d\vartheta_*\, d\phi_*, \quad \text{(B.32)}$$

where $\rho(\vartheta_p, \phi_p, \vartheta_*, \vartheta_*)$ is the bidirectional reflectance distribution function, $\hat{k}$ is the unit vector in the direction of the Earth and the frequency Doppler shift $\Delta\nu$ is

$$\frac{\Delta\nu}{\nu} = \frac{\Delta v}{c}, \quad \text{(B.33)}$$

where Δv is the velocity shift due to the reflection of the light on the cell C_p and the shift due to the radial motion of the star cell with respect to the planet cell $\Delta v_{r,c_*c_p}$. This velocity shift is

$$\Delta v = v_p \cdot (\hat{k} - \hat{\sigma}) + \Delta v_{r,c_*c_p}. \quad \text{(B.34)}$$

The surface velocity of the planet cell v_p is determined in Appendix B.2 and $\Delta v_{r,c_*c_p}$ is determined in Appendix B.3.

We now work out the reflected starlight reaching the observer at the Earth. The viewpoint of the observer is given in Figure B.2 and from this we can see that $d\Omega_p$ and $\tan\omega$ is

$$d\Omega_p = \frac{dA}{r^2} = \sin\omega\, d\omega\, d\phi_p, \quad \text{(B.35)}$$

$$\tan\omega = \frac{\rho}{d_{p\oplus}}. \quad \text{(B.36)}$$

Assuming the Earth is very far from the planet we can treat ω as a small angle and Taylor expanding only to first order we have $sin\omega = \omega$ and $cos\omega = 1$ and thus:

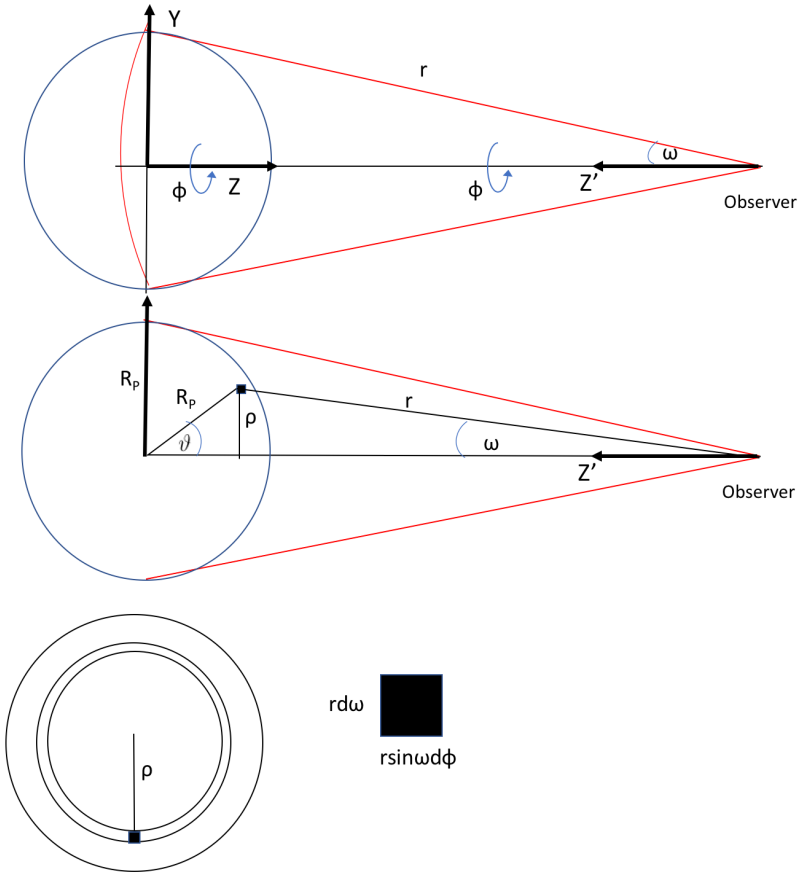

Figure B.2.: Geometry showing the view of the planet with respect to the observer

$$\omega = \frac{R_P \sin \vartheta_p}{d_{p\oplus}}, \tag{B.37}$$

where $d_{p\oplus}$ is distance from the earth to the planet. Differentiating we have:

$$d\omega = (R_P \cos \vartheta_p / d_{p\oplus})\, d\vartheta_p. \tag{B.38}$$

The flux arriving at the distant Earth is:

$$\begin{aligned} F_\oplus(\nu) &= \int_0^{2\pi} \int_0^{\frac{R_p}{d_{p\oplus}}} I_{s\vartheta_p\phi_p}(\vartheta_p, \phi_p, \nu, t) \cos\omega \sin\omega \; d\omega \; d\phi_p \\ &= \int_0^{2\pi} \int_0^{\frac{R_p}{d_{p\oplus}}} I_{s\vartheta_p\phi_p}(\vartheta_p, \phi_p, \nu, t) \omega \; d\omega \; d\phi_p, \end{aligned} \tag{B.39}$$

and thus:

$$F_\oplus(\nu, t) \;=\; \left(\frac{R_p}{d_{p\oplus}}\right)^2 \int_0^{2\pi} \int_0^{\pi/2} I_{s\vartheta_p\phi_p}(\vartheta_p, \phi_p, \nu, t) \sin\vartheta_p \cos\vartheta_p \quad d\vartheta_p \quad d\phi_p. \tag{B.40}$$

B.2. Position and Velocity of Points on Surface of the Planet

B.2.1. Introduction

Initially we work in the frame centred on the barycentre and with xy plane coincident with the plane of the orbit and measure position and velocity of points on the surface of the planet relative to the barycentre. We then move onto determining these velocities in the reference frame as is typically viewed from Earth by using circularised forms of the elliptical two-body equations in order to transform from the barycentric frame to the Earth frame.

The planet moves round the barycentre in a circle or radius a in xy plane with coordinates

$$x = a\frac{m_*}{m_* + m_p} \cos\theta, \tag{B.41}$$

$$y = a\frac{m_*}{m_* + m_p} \sin\theta. \tag{B.42}$$

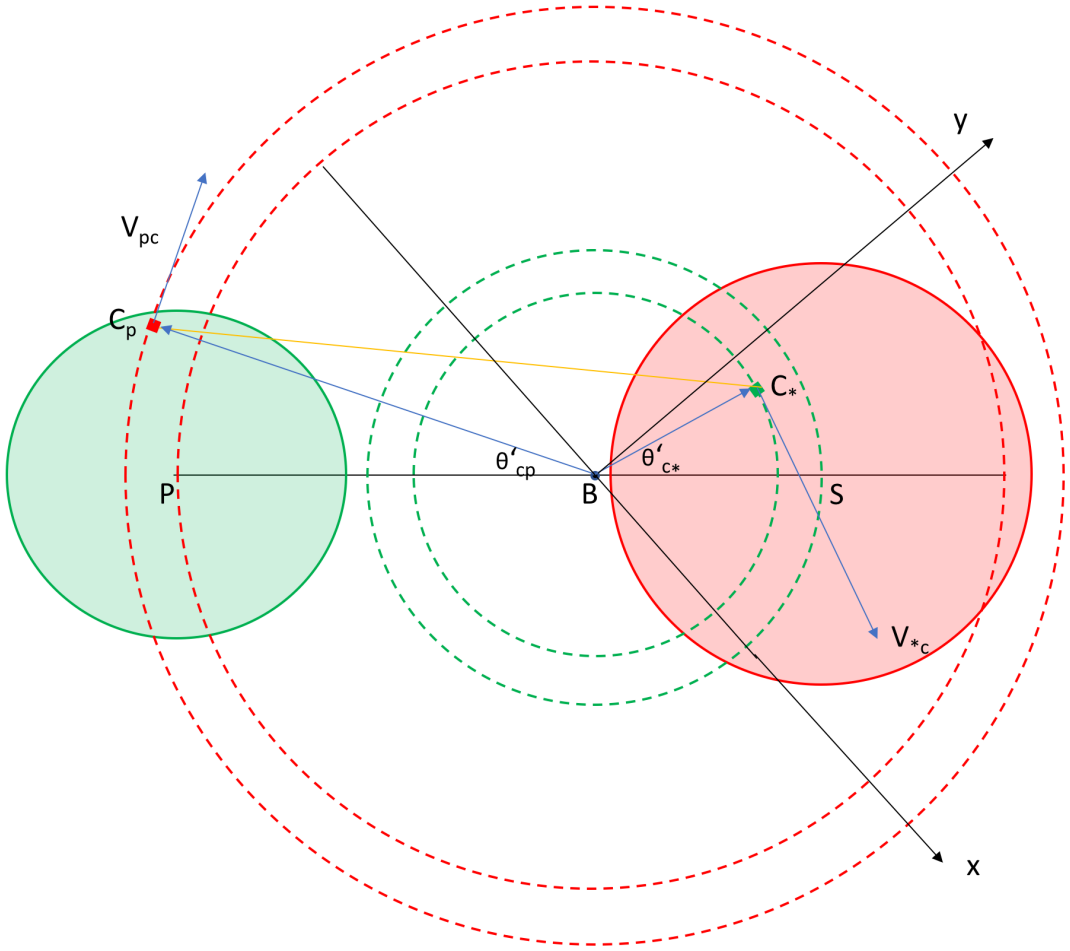

Figure B.3.: Geometry looking down on xy plane of planet and star orbiting the barycentre B along with the paths and motion of cells on the surface of the planet and the star

Figure B.3 shows the path of the orbit of the planet and star and that of the surface cells around the barycentre in the xy plane.

The coordinates of the planet are $P = (x_p, y_p, 0)$ and surface cell coords is $C_p = (x_{pc}, y_{pc}, z_{pc})$.

From Figure 14 it is clear that the cell C_p moves in a circular orbit with radius

$$d_{pc} = \sqrt{x_{pc}^2 + y_{pc}^2}, \tag{B.43}$$

at a height z_{pc} above the xy plane. We can write the x and y coords of the planet in terms of θ and d_{pc} as

$$x_{pc} = d_{pc} \cos(\theta + \theta'_{pc}), \tag{B.44}$$

$$y_{pc} = d_{pc}\sin(\theta + \theta'_{pc}), \tag{B.45}$$

where

$$\sin\theta'_{pc} = \frac{BP \times (x_{pc}, y_{pc}, 0)^T}{|BP||(x_{pc}, y_{pc}, 0)|}, \tag{B.46}$$

and θ'_{pc} is in range $\{-\pi/2, \pi/2\}$.
Differentiating we get the velocity of the cell in the frame to be

$$\dot{x}_{pc} = -d_{pc}\dot{\theta}\sin(\theta + \theta'_{pc}), \tag{B.47}$$

$$\dot{y}_{pc} = d_{pc}\dot{\theta}\cos(\theta + \theta'_{pc}), \tag{B.48}$$

$$\dot{z}_{pc} = 0. \tag{B.49}$$

We can now move to the barycentric frame with Z axis pointing to the Earth and the X and Y axis in the plane of the sky

$$\begin{bmatrix} X_{pc} \\ Y_{pc} \\ Z_{pc} \end{bmatrix} = \begin{bmatrix} \cos\Omega & -\sin\Omega & 0 \\ \sin\Omega & \cos\Omega & 0 \\ 0 & 0 & 1 \end{bmatrix} \begin{bmatrix} 1 & 0 & 0 \\ 0 & \cos I & -\sin I \\ 0 & \sin I & \cos I \end{bmatrix} \begin{bmatrix} d_{pc}\cos(\theta + \theta'_{pc}) \\ d_{pc}\sin(\theta + \theta'_{pc}) \\ z_{pc} \end{bmatrix}, \tag{B.50}$$

$$\begin{bmatrix} X_{pc} \\ Y_{pc} \\ Z_{pc} \end{bmatrix} = \begin{bmatrix} \cos\Omega & -\sin\Omega & 0 \\ \sin\Omega & \cos\Omega & 0 \\ 0 & 0 & 1 \end{bmatrix} \begin{bmatrix} d_{pc}\cos(\theta + \theta'_{pc}) \\ d_{pc}\sin(\theta + \theta'_{pc})\cos I - z_{pc}\sin I \\ d_{pc}\sin(\theta + \theta'_{pc})\sin I + z_{pc}\cos I \end{bmatrix}, \tag{B.51}$$

$$\begin{bmatrix} X_{pc} \\ Y_{pc} \\ Z_{pc} \end{bmatrix} =$$

$$\begin{bmatrix} d_{pc}(cos\Omega cos(\theta + \theta'_{pc}) - sin\Omega sin(\theta + \theta'_{pc})cosI) + z_{pc}sin\Omega sinI \\ d_{pc}(sin\Omega cos(\theta + \theta'_{pc}) + cos\Omega sin(\theta + \theta'_{pc})cosI) - z_{pc}cos\Omega sinI \\ d_{pc}sin(\theta + \theta'_{pc})sinI + z_{pc}cosI \end{bmatrix}. \tag{B.52}$$

Differentiating we get the velocity

$$\begin{bmatrix}\dot{X}_{pc}\\ \dot{Y}_{pc}\\ \dot{Z}_{pc}\end{bmatrix} = \begin{bmatrix}-\dot{\theta}d_{pc}(cos\Omega sin(\theta+\theta'_{pc}) + sin\Omega cos(\theta+\theta'_{pc})cosI)\\ -\dot{\theta}d_{pc}(sin\Omega sin(\theta+\theta'_{pc}) - cos\Omega cos(\theta+\theta'_{pc})cosI)\\ \dot{\theta}d_{pc}\cos(\theta+\theta'_{pc})\sin I\end{bmatrix}. \quad \text{(B.53)}$$

We typically know Ω, I and $\{X_{pc}, Y_{pc}, Z_{pc}\}^T$ and θ and need to determine d_{pc}, z_{pc} and θ'_{pc} from the above equations. Noting that the above equations are linear in $d_{pc}\cos(\theta+\theta'_{pc}), d_{pc}\sin(\theta+\theta'_{pc})$ and z_{pc} we can arrange the matrices as follows

$$\begin{bmatrix}X_{pc}\\ Y_{pc}\\ Z_{pc}\end{bmatrix} = \begin{bmatrix}\cos\Omega & -\sin\Omega\cos I & \sin\Omega\sin I\\ \sin\Omega & \cos\Omega\cos I & -\cos\Omega\sin I\\ 0 & \sin I & \cos I\end{bmatrix}\begin{bmatrix}d_{pc}\cos(\theta+\theta'_{pc})\\ d_{pc}\sin(\theta+\theta'_{pc})\\ z_{pc}\end{bmatrix}. \quad \text{(B.54)}$$

We can invert the above matrix (determinant is 1 so it is non-singular) and solve for our three parameters

$$\begin{bmatrix}d_{pc}\cos(\theta+\theta'_{pc})\\ d_{pc}\sin(\theta+\theta'_{pc})\\ z_{pc}\end{bmatrix} = \begin{bmatrix}\cos\Omega & \sin\Omega & 0\\ -\sin\Omega\cos I & \cos\Omega\cos I & \sin I\\ \sin\Omega\sin I & -\cos\Omega\sin I & \cos I\end{bmatrix}\begin{bmatrix}X_{pc}\\ Y_{pc}\\ Z_{pc}\end{bmatrix} = \begin{bmatrix}l\\ m\\ n\end{bmatrix}. \quad \text{(B.55)}$$

From this we can see that

$$d_{pc} = \sqrt{l^2+m^2}, \quad \text{(B.56)}$$

and

$$sin\theta' = \frac{mcos\theta - lsin\theta}{d_{pc}}. \quad \text{(B.57)}$$

B.3. Position and Velocity of Point On Surface of the Star

We determine the velocity and position of a point on the surface of the star - a star cell - with respect to the barycentre of the system.

The velocity of a star cell v_{*c} is formed of two components due to the motion of the orbit of the star around the centre of mass of the system $v_{*c,o}$ and the spin of

the star $v_{*c,sp}$

$$v_{*c} = v_{*c,o} + v_{*c,sp}. \tag{B.58}$$

In our determination of the Doppler shift of reflected light we need to know the component of the surface velocity in the direction of a given planet cell. If we denote $(\hat{\sigma})$ as the unit vector in that direction then the component velocity is given by

$$\Delta v_{r,c_*c_p} = v_{*c} \cdot \hat{\sigma}. \tag{B.59}$$

The next two subsections determine each of the terms on the right hand side of equation B.58 in turn.

B.3.1. Orbital component of velocity of star cell

The star moves round the barycentre in a circle of radius a in the xy plane with coordinates

$$x = a\frac{m_p}{m_* + m_p}\cos\theta, \tag{B.60}$$

$$y = a\frac{m_p}{m_* + m_p}\sin\theta. \tag{B.61}$$

Figure B.3 shows the path of the orbit of the planet and star and that of the surface cells around the barycentre in the xy plane. The coordinates of the star are $P = (x_*, y_*, 0)$ and surface cell coords is $C_p = (x_{*c}, y_{*c}, z_{*c})$. From B.3 it is clear that the cell C_* moves in a circular orbit with radius

$$d_{*c} = \sqrt{x_{*c}^2 + y_{*c}^2}, \tag{B.62}$$

at a height z_{*c} above the xy plane. We can write the x and y coords of the planet in terms of θ and d_{*c} as:

$$x_{*c} = d_{*c}\cos(\theta + \theta'_{*c} + \pi) = -d_{*c}\cos(\theta + \theta'_{*c}), \tag{B.63}$$

$$y_{*c} = d_{*c}\sin(\theta + \theta'_{*c} + \pi) = -d_{*c}\sin(\theta + \theta'_{*c}), \tag{B.64}$$

$$z_{*c} = z_{*c}, \tag{B.65}$$

where

$$\sin\theta'_{*c} = \frac{BS \times (x_{*c}, y_{*c}, 0)^T}{|BS||(x_{*c}, y_{*c}, 0)|}, \tag{B.66}$$

and θ'_{*c} is in range $\{-\pi/2, \pi/2\}$.

Differentiating we get the velocity of the cell in the frame to be

$$\dot{x}_{*c} = d_{*c}\dot{\theta}\sin(\theta + \theta'_{*c}), \tag{B.67}$$

$$\dot{y}_{*c} = -d_{*c}\dot{\theta}\cos(\theta + \theta'_{*c}), \tag{B.68}$$

$$\dot{z}_{*c} = 0. \tag{B.69}$$

We can now move to the barycentric frame with Z axis pointing to the Earth and the X and Y axis in the plane of the sky:

$$\begin{bmatrix} X_{*c} \\ Y_{*c} \\ Z_{*c} \end{bmatrix} = \begin{bmatrix} cos\Omega & -sin\Omega & 0 \\ sin\Omega & cos\Omega & 0 \\ 0 & 0 & 1 \end{bmatrix} \begin{bmatrix} 1 & 0 & 0 \\ 0 & cosI & -sinI \\ 0 & sinI & cosI \end{bmatrix} \begin{bmatrix} -d_{*c}cos(\theta + \theta'_{pc}) \\ -d_{*c}sin(\theta + \theta'_{pc}) \\ z_{*c} \end{bmatrix}, \tag{B.70}$$

$$\begin{bmatrix} X_{*c} \\ Y_{*c} \\ Z_{*c} \end{bmatrix} = \begin{bmatrix} cos\Omega & -sin\Omega & 0 \\ sin\Omega & cos\Omega & 0 \\ 0 & 0 & 1 \end{bmatrix} \begin{bmatrix} -d_{*c}cos(\theta + \theta'_{*c}) \\ -d_{*c}sin(\theta + \theta'_{*c})cosI - z_{*c}sinI \\ -d_{*c}sin(\theta + \theta'_{*c})sinI + z_{*c}cosI \end{bmatrix}, \tag{B.71}$$

$$\begin{bmatrix} X_{*c} \\ Y_{*c} \\ Z_{*c} \end{bmatrix} = \begin{bmatrix} -d_{*c}(cos\Omega cos(\theta + \theta'_{*c}) - sin\Omega sin(\theta + \theta'_{*c})cosI) + z_{*c}sin\Omega sinI \\ -d_{*c}(sin\Omega cos(\theta + \theta'_{*c}) + cos\Omega sin(\theta + \theta'_{*c})cosI) - z_{*c}cos\Omega sinI \\ -d_{*c}sin(\theta + \theta'_{*c})sinI + z_{*c}cosI \end{bmatrix}. \tag{B.72}$$

Differentiating we get the velocity

$$v_{*c,o} = \begin{bmatrix} \dot{X}_{*c} \\ \dot{Y}_{*c} \\ \dot{Z}_{*c} \end{bmatrix}, \tag{B.73}$$

$$v_{*c,o} = \begin{bmatrix} \dot{\theta} d_{*c}(cos\Omega sin(\theta + \theta'_{*c}) + sin\Omega cos(\theta + \theta'_{*c}) cosI) \\ \dot{\theta} d_{*c}(sin\Omega sin(\theta + \theta'_{*c}) - cos\Omega cos(\theta + \theta'_{*c}) cosI) \\ -\dot{\theta} d_{*c} cos(\theta + \theta'_{*c}) sinI \end{bmatrix}. \tag{B.74}$$

We typically know Ω, I and $\{X_{*c}, Y_{*c}, Z_{*c}\}^T$ and θ and need to determine d_{*c}, z_{*c} and θ'_{*c} from the above equations. Noting that the above equations are linear in $d_{*c}cos(\theta + \theta'_{*c}), d_{*c}sin(\theta + \theta'_{*c})$ and z_{*c} we can arrange the matrices as follows

$$\begin{bmatrix} X_{*c} \\ Y_{*c} \\ Z_{*c} \end{bmatrix} = \begin{bmatrix} cos\Omega & -sin\Omega cosI & sin\Omega sinI \\ sin\Omega & cos\Omega cosI & -cos\Omega sinI \\ 0 & sinI & cosI \end{bmatrix} \begin{bmatrix} -d_{*c}cos(\theta + \theta'_{*c}) \\ -d_{*c}sin(\theta + \theta'_{*c}) \\ z_{*c} \end{bmatrix}. \tag{B.75}$$

We can invert the above matrix (determinant is 1 so it is non-singular) and solve for our three parameters

$$\begin{bmatrix} -d_{*c}\cos(\theta + \theta'_{*c}) \\ -d_{*c}\sin(\theta + \theta'_{*c}) \\ z_{*c} \end{bmatrix} = \begin{bmatrix} \cos\Omega & \sin\Omega & 0 \\ -\sin\Omega\cos I & \cos\Omega\cos I & \sin I \\ \sin\Omega\sin I & -\cos\Omega\sin I & \cos I \end{bmatrix} \begin{bmatrix} X_{*c} \\ Y_{*c} \\ Z_{*c} \end{bmatrix} = \begin{bmatrix} l \\ m \\ n \end{bmatrix}. \tag{B.76}$$

From this we can see that

$$d_{*c} = \sqrt{l^2 + m^2}, \tag{B.77}$$

and

$$\sin\theta' = \frac{l\sin\theta - m\cos\theta}{d_{*c}}. \tag{B.78}$$

B.3.2. Star cell velocity component due to spin of star

Now we determine the velocity of the star cell due to the spin of the star $v_{*c,sp}$. We make the assumption that the stellar rotation is aligned to its orbit and in particular that there is no obliquity. We also assume that the observed rotation period of the star has been determined from photometry $P_{*,obs}$ and is related to the observed angular velocity $\Omega_{*,obs}$ as

$$\Omega_{*,obs} = \frac{2\pi}{P_{*,obs}}. \tag{B.79}$$

The observed angular velocity is made up of two components due to the spin of the star and the orbit of the system

$$\Omega_{*,obs} = \Omega_* + \Omega_{*,orb}. \tag{B.80}$$

The magnitude of $\Omega_{*,orb}$ is known from the period of the exoplanet and star from the RV measurements so we can determine the spin from the star Ω_*. We determine the spin axis unit vector by noting that it is in the same direction out of the plane of orbit of the two body model centred on the planet. Thus we have

$$\hat{\mathbf{\Omega}}_* = \frac{r \times \dot{r}}{|r \times \dot{r}|}. \tag{B.81}$$

Components or r and $\dot{r}$ with respect to the planet are

$$x = a\cos(\theta + \pi) = -a\cos\theta, \tag{B.82}$$

$$y = a\sin(\theta + \pi) = -a\sin\theta, \tag{B.83}$$

$$z = 0. \tag{B.84}$$

Transforming to viewpoint of earth in XYZ frame we have:

$$r = \begin{bmatrix} X_{*p} \\ Y_{*p} \\ Z_{*p} \end{bmatrix} = \begin{bmatrix} cos\Omega & -sin\Omega & 0 \\ sin\Omega & cos\Omega & 0 \\ 0 & 0 & 1 \end{bmatrix} \begin{bmatrix} 1 & 0 & 0 \\ 0 & cosI & -sinI \\ 0 & sinI & cosI \end{bmatrix} \begin{bmatrix} -acos\theta \\ -asin\theta \\ 0 \end{bmatrix}, \tag{B.85}$$

$$r = \begin{bmatrix} X_{*c} \\ Y_{*c} \\ Z_{*c} \end{bmatrix} = \begin{bmatrix} \cos\Omega & -\sin\Omega & 0 \\ \sin\Omega & \cos\Omega & 0 \\ 0 & 0 & 1 \end{bmatrix} \begin{bmatrix} -a\cos\theta \\ -a\sin\theta cosI \\ -a\sin\theta sinI \end{bmatrix}, \tag{B.86}$$

$$r = \begin{bmatrix} X_{*p} \\ Y_{*p} \\ Z_{*p} \end{bmatrix} = \begin{bmatrix} -a(\cos\Omega\cos\theta - \sin\Omega\sin\theta\cos I) \\ -a(\sin\Omega\cos\theta + \cos\Omega\sin\theta\cos I) \\ -a\sin\theta\sin I \end{bmatrix}. \tag{B.87}$$

Differentiating we get the velocity

$$\dot{r} = \begin{bmatrix} \dot{X}_{*p} \\ \dot{Y}_{*p} \\ \dot{Z}_{*p} \end{bmatrix} = \begin{bmatrix} \dot{\theta}a(\cos\Omega\sin\theta + \sin\Omega\cos\theta\cos I) \\ \dot{\theta}a(\sin\Omega\sin\theta - \cos\Omega\cos\theta\cos I) \\ -\dot{\theta}a\cos\theta\sin I \end{bmatrix}. \tag{B.88}$$

Now the cross product is

$$r \times \dot{r} = a^2\dot{\theta} \begin{bmatrix} \sin I\sin\Omega \\ -\sin I\cos\Omega \\ \cos I \end{bmatrix}. \tag{B.89}$$

Dividing out the leading term $a^2\dot{\theta}$ we get the unit vector for $\hat{\mathbf{\Omega}}_*$ to be

$$\hat{\mathbf{\Omega}}_* = \begin{bmatrix} \sin I\sin\Omega \\ -\sin I\cos\Omega \\ \cos I \end{bmatrix}. \tag{B.90}$$

If we let r_{*c} denote the vector $\overrightarrow{O_*C_*}$ from the centre of the star to the star cell then we have that the velocity of the star cell v_{C_*} is just

$$v_{*c,sp} = \mathbf{\Omega}_* \times r_{*c}. \tag{B.91}$$

Bibliography

Agol E., Steffen J., Sari R., Clarkson W., 2005, MNRAS, 359, 567

Aigrain S., Pont F., Zucker S., 2012, Monthly Notices of the Royal Astronomical Society, 419, 3147

Aigrain S., et al., 2016, in 19th Cambridge Workshop on Cool Stars, Stellar Systems, and the Sun (CS19). Cambridge Workshop on Cool Stars, Stellar Systems, and the Sun. p. 12, doi:10.5281/zenodo.154565

Albrecht S., Winn J. N., Butler R. P., Crane J. D., Shectman S. A., Thompson I. B., Hirano T., Wittenmyer R. A., 2012, ApJ, 744, 189

Alonso-Floriano F. J., et al., 2015, A&A, 577, A128

Angel J. R. P., Cheng A. Y. S., Woolf N. J., 1986, Nature, 322, 341

Angerhausen D., DeLarme E., Morse J. A., 2015, PASP, 127, 1113

Anglada-Escudé G., Butler R. P., 2012, ApJS, 200, 15

Anglada-Escudé G., Klioner S. A., Soffel M., Torra J., 2007, A&A, 462, 371

Anglada-Escudé G., et al., 2013, A&A, 556, A126

Anglada-Escudé G., et al., 2016, Nature, 536, 437

Astudillo-Defru N., Delfosse X., Bonfils X., Forveille T., Lovis C., Rameau J., 2017a, A&A, 600, A13

Astudillo-Defru N., et al., 2017b, A&A, 605, L11

Auvergne M., et al., 2009, A&A, 506, 411

Bakos G. Á., Hartman J. D., Torres G., Kovács G., Noyes R. W., Latham D. W., Sasselov D. D., Béky B., 2011, in European Physical Journal Web of Conferences. p. 01002 (arXiv:1101.0322), doi:10.1051/epjconf/20101101002

Baluev R. V., 2009, MNRAS, 395, 1541

Baluev R. V., 2013, MNRAS, 436, 807

Baranne A., Mayor M., Poncet J. L., 1979, Vistas in Astronomy, 23, 279

Baranne A., et al., 1996, Astronomy and Astrophysics Supplement Series, 119, 373

Barclay T., et al., 2013, Nature, 494, 452

Barclay T., Pepper J., Quintana E. V., 2018b, ApJS, 239, 2

Barclay T., Pepper J., Quintana E. V., 2018a, The Astrophysical Journal Supplement Series, 239, 2

Barstow J. K., Irwin P. G. J., 2016, MNRAS, 461, L92

Batalha N. M., 2014, Proceedings of the National Academy of Science, 111, 12647

Bennett D. P., 2008, Detection of Extrasolar Planets by Gravitational Microlensing. p. 47, doi:10.1007/978-3-540-74008-7˙3

Berdiñas Z. M., Amado P. J., Anglada-Escude G., 2015, in van Belle G. T., Harris H. C., eds, Cambridge Workshop on Cool Stars, Stellar Systems, and the Sun Vol. 18, 18th Cambridge Workshop on Cool Stars, Stellar Systems, and the Sun. pp 723–732

Berdiñas Z. M., Rodríguez-López C., Amado P. J., Anglada-Escudé G., Barnes J. R., MacDonald J., Zechmeister M., Sarmiento L. F., 2017, MNRAS, 469, 4268

Berdyugina S. V., Kuhn J. R., 2019, AJ, 158, 246

Berta Z. K., et al., 2012, ApJ, 747, 35

Bessel F. W., 1844, MNRAS, 6, 136

Birkby J. L., de Kok R. J., Brogi M., Schwarz H., Snellen I. A. G., 2017, AJ, 153, 138

Boisse I., et al., 2009, Astronomy and Astrophysics, 495, 959

Boisse I., Bouchy F., Hébrard G., Bonfils X., Santos N., Vauclair S., 2011, Astronomy and Astrophysics, 528, A4

Boisse I., Santerne A., Beaulieu J. P., Fakhardji W., Santos N. C., Figueira P., Sousa S. G., Ranc C., 2015, A&A, 582, L11

Bond I. A., et al., 2004, The Astrophysical Journal, 606, L155

Borra E. F., Deschatelets D., 2018, MNRAS, 481, 4841

Borucki W. J., et al., 2009, Science, 325, 709

Borucki W. J., et al., 2010, Science, 327, 977

Borucki W. J., et al., 2011, ApJ, 736, 19

Bouchy F., et al., 2005, A&A, 444, L15

Boyajian T., et al., 2015, MNRAS, 447, 846

Brogi M., Snellen I. A. G., de Kok R. J., Albrecht S., Birkby J., de Mooij E. J. W., 2012, Nature, 486, 502

Bundy K. A., Marcy G. W., 2000, PASP, 112, 1421

Butler R. P., Marcy G. W., 1996, ApJL, 464, L153

Butler R. P., Marcy G. W., Williams E., McCarthy C., Dosanjh P., Vogt S. S., 1996, Publications of the Astronomical Society of the Pacific, 108, 500

Butler R. P., Vogt S. S., Marcy G. W., Fischer D. A., Wright J. T., Henry G. W., Laughlin G., Lissauer J. J., 2004, ApJ, 617, 580

Caballero J. A., et al., 2016, in Observatory Operations: Strategies, Processes, and Systems VI. p. 99100E, doi:10.1117/12.2233574

Campbell B., Walker G. A. H., 1979, PASP, 91, 540

Cegla H. M., Lovis C., Bourrier V., Beeck B., Watson C. A., Pepe F., 2016, A&A, 588, A127

Chaplin W. J., et al., 2015, PASP, 127, 1038

Charbonneau D., Deming D., 2007, arXiv e-prints, p. arXiv:0706.1047

Charbonneau D., Noyes R. W., Korzennik S. G., Nisenson P., Jha S., Vogt S. S., Kibrick R. I., 1999, ApJL, 522, L145

Charbonneau D., Brown T. M., Latham D. W., Mayor M., 2000, ApJL, 529, L45

Charbonneau D., Brown T. M., Noyes R. W., Gilliland R. L., 2002, ApJ, 568, 377

Charbonneau D., et al., 2005, ApJ, 626, 523

Charrett T. O. H., James S. W., Tatam R. P., 2012, Measurement Science and Technology, 23, 032001

Chauvin G., Lagrange A.-M., Dumas C., Zuckerman B., Mouillet D., Song I., Beuzit J.-L., Lowrance P., 2004, A&A, 425, L29

Claudi R., 2016, Direct Imaging of Faint Companions. Springer International Publishing, Cham, pp 183–252, doi:10.1007/978-3-319-27458-4˙4, https://doi.org/10.1007/978-3-319-27458-4_4

Clements D. L., 2018, Journal of the British Interplanetary Society, 71, 222

Coffinet A., Lovis C., Dumusque X., Pepe F., 2019, A&A, 629, A27

Collier Cameron A., Horne K., Penny A., James D., 1999, Nature, 402, 751

Collier Cameron A., Horne K., Penny A., Leigh C., 2002a, MNRAS, 330, 187

Collier Cameron A., Donati J. F., Semel M., 2002b, MNRAS, 330, 699

Collier Cameron A., Bruce V. A., Miller G. R. M., Triaud A. H. M. J., Queloz D., 2010, MNRAS, 403, 151

Collier Cameron A., et al., 2019, Monthly Notices of the Royal Astronomical Society, 487, 1082

Connes P., 1985, Ap&SS, 110, 211

Correia A. C. M., 2014, A&A, 570, L5

Coustenis A., 1995, Earth Moon and Planets, 67, 95

Crane J. D., Shectman S. A., Butler R. P., Thompson I. B., Birk C., Jones P., Burley G. S., 2010, in Proc. SPIE. p. 773553, doi:10.1117/12.857792

Davison C. L., et al., 2015, AJ, 149, 106

Dawson R. I., Fabrycky D. C., 2010, ApJ, 722, 937

Des Marais D. J., et al., 2002, Astrobiology, 2, 153

Donati J.-F., Semel M., Carter B. D., Rees D. E., Collier Cameron A., 1997, MNRAS, 291, 658

Doyle L. R., et al., 2011, Science, 333, 1602

Dumusque X., 2016, Astronomy and Astrophysics, 593, A5

Dumusque X., 2018, Astronomy and Astrophysics, 620, A47

Dumusque X., Udry S., Lovis C., Santos N. C., Monteiro M. J. P. F. G., 2011a, Astronomy and Astrophysics, 525, A140

Dumusque X., et al., 2011b, Astronomy and Astrophysics, 535, A55

Dumusque X., et al., 2012, Nature, 491, 207

Eddington A. S., 1919, Nature, 104, 372

Eggenberger A., Udry S., 2010, in Montmerle T., Ehrenreich D., Lagrange A. M., eds, EAS Publications Series Vol. 41, EAS Publications Series. pp 27–75 (arXiv:0904.0415), doi:10.1051/eas/1041002

Faria J. P., Haywood R. D., Brewer B. J., Figueira P., Oshagh M., Santerne A., Santos N. C., 2016, Astronomy and Astrophysics, 588, A31

Feng F., Tuomi M., Jones H. R. A., Barnes J., Anglada-Escudé G., Vogt S. S., Butler R. P., 2017, The Astronomical Journal, 154, 135

Feroz F., Hobson M. P., 2014, Monthly Notices of the Royal Astronomical Society, 437, 3540

Gaia Collaboration 2018, VizieR Online Data Catalog, 1345

Gajjar V., et al., 2019, arXiv e-prints, p. arXiv:1907.05519

Gillon M., et al., 2007, A&A, 472, L13

Gillon M., et al., 2017, Nature, 542, 456

Goncharskii A. V., Stepanov V. V., Kokhlova V. L., Yagola A. G., 1977, Soviet Astronomy Letters, 3, 147

González Hernández J. I., Pepe F., Molaro P., Santos N. C., 2018, ESPRESSO on VLT: An Instrument for Exoplanet Research. p. 157, doi:10.1007/978-3-319-55333-7˙157

Gray D. F., 2005, The Observation and Analysis of Stellar Photospheres

Gray R. H., Mooley K., 2017, The Astronomical Journal, 153, 110

Gregory P. C., 2011, Monthly Notices of the Royal Astronomical Society, 410, 94

Griffin R., 1973, MNRAS, 162, 243

Groetsch C., 2007, J. Phys.: Conf. Ser., 73

Grunblatt S. K., Howard A. W., Haywood R. D., 2015, The Astrophysical Journal, 808, 127

Hansen P. C., 1994, Numerical Algorithms

Hansen P., 2010, Discrete inverse problems : insight and algorithms. SIAM

Harrington J., Hansen B. M., Luszcz S. H., Seager S., Deming D., Menou K., Cho J. Y.-K., Richardson L. J., 2006, Science, 314, 623

Hartman J. D., et al., 2015, AJ, 150, 197

Hastings W. K., 1970, Biometrika, 57, 97

Haywood R. D., et al., 2014, in Booth M., Matthews B. C., Graham J. R., eds, IAU Symposium Vol. 299, Exploring the Formation and Evolution of Planetary Systems. pp 237–240, doi:10.1017/S1743921313008478

Hebb L., et al., 2010, ApJ, 708, 224

Hébrard É. M., Donati J. F., Delfosse X., Morin J., Boisse I., Moutou C., Hébrard G., 2014, Monthly Notices of the Royal Astronomical Society, 443, 2599

Hellier C., Anderson D. R., Collier-Cameron A., Miller G. R. M., Queloz D., Smalley B., Southworth J., Triaud A. H. M. J., 2011, ApJL, 730, L31

Henry G. W., Winn J. N., 2008, AJ, 135, 68

Henry G. W., Marcy G., Butler R. P., Vogt S. S., 1999, IAU Circ., 7307, 1

Hewish A., Bell S. J., Pilkington J. D. H., Scott P. F., Collins R. A., 1968, Nature, 217, 709

Hosey A. D., Henry T. J., Jao W.-C., Dieterich S. B., Winters J. G., Lurie J. C., Riedel A. R., Subasavage J. P., 2015, AJ, 150, 6

Howell S. B., et al., 2014, PASP, 126, 398

Huang S.-S., 1959, PASP, 71, 421

Husser T.-O., Wende-von Berg S., Dreizler S., Homeier D., Reiners A., Barman T., Hauschildt P. H., 2013, A&A, 553, A6

Jackson B. K., Lewis N. K., Barnes J. W., Drake Deming L., Showman A. P., Fortney J. J., 2012, ApJ, 751, 112

Johns-Krull C. M., Valenti J. A., 1996, in Pallavicini R., Dupree A. K., eds, Astronomical Society of the Pacific Conference Series Vol. 109, Cool Stars, Stellar Systems, and the Sun. p. 609

Kasting J. F., Whitmire D. P., Reynolds R. T., 1993, Icarus, 101, 108

Kiefer F., 2019, A&A, 632, L9

Kiraga M., Stepien K., 2007, Acta Astronomica, 57, 149

Kochukhov O., 2016, Doppler and Zeeman Doppler Imaging of Stars. p. 177, doi:10.1007/978-3-319-24151-7˙9

Koen C., Kilkenny D., van Wyk F., Marang F., 2010, MNRAS, 403, 1949

Kopparapu R. K., et al., 2013, The Astrophysical Journal, 765, 131

Latham D. W., Mazeh T., Stefanik R. P., Mayor M., Burki G., 1989, Nature, 339, 38

Lockwood A. C., Johnson J. A., Bender C. F., Carr J. S., Barman T., Richert A. J. W., Blake G. A., 2014, The Astrophysical Journal, 783, L29

Louden T., Wheatley P. J., 2015, ApJL, 814, L24

Lovis C., Fischer D., 2010, Radial Velocity Techniques for Exoplanets. pp 27–53

Lovis C., Pepe F., 2007, A&A, 468, 1115

Lovis C., et al., 2017, A&A, 599, A16

Lurie J. C., Davenport J. R. A., Hawley S. L., Wilkinson T. D., Wisniewski J. P., Kowalski A. F., Hebb L., 2015, ApJ, 800, 95

Maldonado J., et al., 2015, A&A, 577, A132

Marcy G. W., Butler R. P., 1992, PASP, 104, 270

Marcy G. W., Butler R. P., 1995, in American Astronomical Society Meeting Abstracts. p. 70.04

Marcy G. W., Butler R. P., 1996, ApJL, 464, L147

Marois C., Lafrenière D., Doyon R., Macintosh B., Nadeau D., 2006, ApJ, 641, 556

Marois C., Macintosh B., Barman T., Zuckerman B., Song I., Patience J., Lafrenière D., Doyon R., 2008, Science, 322, 1348

Martins J. H. C., et al., 2015a, A&A, 576, A134

Martins J. H. C., et al., 2015b, A&A, 576, A134

Martins J. H. C., Santos N. C., Figueira P., Melo C., 2016, Origins of Life and Evolution of the Biosphere, 46, 487

Mayor M., Queloz D., 1995, Nature, 378, 355

Mayor M., et al., 2003, The Messenger, 114, 20

McArthur B. E., et al., 2004, ApJL, 614, L81

McKemmish L. K., Masseron T., Hoeijmakers H. J., Pérez-Mesa V., Grimm S. L., Yurchenko S. N., Tennyson J., 2019, MNRAS, 488, 2836

McLaughlin D. B., 1924, Popular Astronomy, 32, 558

Mesa D., et al., 2015, Astronomy & Astrophysics, 576, A121

Metropolis N., Rosenbluth A. W., Rosenbluth M. N., Teller A. H., Teller E., 1953, J. Chem. Phys., 21, 1087

Mills S. M., Fabrycky D. C., Migaszewski C., Ford E. B., Petigura E., Isaacson H., 2016, Nature, 533, 509?512

Mislis D., Heller R., Schmitt J. H. M. M., Hodgkin S., 2012, A&A, 538, A4

Mittag M., Schmitt J. H. M. M., Schröder K.-P., 2018, A&A, 618, A48

Muraki Y., et al., 1999, Progress of Theoretical Physics Supplement, 133, 233

Murray C. D., Correia A. C. M., 2010, Keplerian Orbits and Dynamics of Exoplanets. pp 15–23

Muterspaugh M. W., et al., 2010, AJ, 140, 1657

Ohta Y., Taruya A., Suto Y., 2005, ApJ, 622, 1118

Owen T., 1980, in Papagiannis M. D., ed., Astrophysics and Space Science Library Vol. 83, Strategies for the Search for Life in the Universe. p. 177, doi:10.1007/978-94-009-9115-6˙17

Pallé E., Zapatero Osorio M. R., Barrena R., Montañés-Rodríguez P., Martín E. L., 2009, Nature, 459, 814

Parviainen H., Aigrain S., 2015, MNRAS, 453, 3821

Pepe F., et al., 2000, in Iye M., Moorwood A. F., eds, Proc. SPIEVol. 4008, Optical and IR Telescope Instrumentation and Detectors. pp 582–592

Pepe F., Mayor M., Galland F., Naef D., Queloz D., Santos N. C., Udry S., Burnet M., 2002, Astronomy and Astrophysics, 388, 632

Pepe F., et al., 2013, The Messenger, 153, 6

Pepe F., et al., 2014, Astronomische Nachrichten, 335, 8

Perryman M., 2018, The Exoplanet Handbook. Cambridge University Press

Perryman M. A. C., et al., 1997, A&A, 500, 501

Perryman M., Hartman J., Bakos G. Á., Lindegren L., 2014, ApJ, 797, 14

Piskorz D., et al., 2016, ApJ, 832, 131

Pojmanski G., 1997, Acta Astronomica, 47, 467

Pojmański G., 2004, Astronomische Nachrichten, 325, 553

Pollacco D., et al., 2006, Ap&SS, 304, 253

Queloz D., Eggenberger A., Mayor M., Perrier C., Beuzit J. L., Naef D., Sivan J. P., Udry S., 2000, A&A, 359, L13

Queloz D., et al., 2001, Astronomy and Astrophysics, 379, 279

Quirrenbach A., et al., 2010, in Ground-based and Airborne Instrumentation for Astronomy III. p. 773513, doi:10.1117/12.857777

Rajpaul V., Aigrain S., Osborne M. A., Reece S., Roberts S., 2015, Monthly Notices of the Royal Astronomical Society, 452, 2269

Reiners A., Basri G., 2007, ApJ, 656, 1121

Reiners A., Bean J. L., Huber K. F., Dreizler S., Seifahrt A., Czesla S., 2010, ApJ, 710, 432

Reiners A., et al., 2018, A&A, 612, A49

Ricker G. R., et al., 2009, in American Astronomical Society Meeting Abstracts #213. p. 403.01

Ricker G. R., et al., 2010, in American Astronomical Society Meeting Abstracts #215. p. 459

Rivera E. J., et al., 2005, ApJ, 634, 625

Robertson P., Endl M., Henry G. W., Cochran W. D., MacQueen P. J., Williamson M. H., 2015, The Astrophysical Journal, 801, 79

Rodler F., Lopez-Morales M., Ribas I., 2012, ApJL, 753, L25

Rodríguez E., Rodríguez-López C., López-González M. J., Amado P. J., Ocando S., Berdiñas Z. M., 2016, MNRAS, 457, 1851

Rogers L. A., Seager S., 2010, ApJ, 712, 974

Rossiter R. A., 1924, ApJ, 60

Santos N. C., Israelian G., Mayor M., Rebolo R., Udry S., 2003, A&A, 398, 363

Schneider J., 2011, in EPSC-DPS Joint Meeting 2011. p. 3

Schneider J., Dedieu C., Le Sidaner P., Savalle R., Zolotukhin I., 2011, A&A, 532, A79

Schuh S., et al., 2010, Ap&SS, 329, 231

Schwarz H., Ginski C., de Kok R. J., Snellen I. A. G., Brogi M., Birkby J. L., 2016, A&A, 593, A74

Seager S., 2010, Exoplanet Atmospheres: Physical Processes. Princeton Series in Astrophysics, Princeton University Press, https://books.google.co.uk/books?id=XpaYJD7IE20C

Seager S., Mallén-Ornelas G., 2003, ApJ, 585, 1038

Seager S., Sasselov D. D., 1998, ApJL, 502, L157

Seager S., Whitney B. A., Sasselov D. D., 2000, ApJ, 540, 504

Seager S., Schrenk M., Bains W., 2012, Astrobiology, 12, 61

Sedaghati E., et al., 2017, Nature, 549, 238

Shulyak D., Reiners A., Seemann U., Kochukhov O., Piskunov N., 2014, A&A, 563, A35

Siemion A., et al., 2013, in van Leeuwen J., ed., IAU Symposium Vol. 291, Neutron Stars and Pulsars: Challenges and Opportunities after 80 years. pp 57–57, doi:10.1017/S1743921312023149

Snellen I. A. G., Albrecht S., de Mooij E. J. W., Le Poole R. S., 2008, A&A, 487, 357

Snellen I. A. G., de Kok R. J., de Mooij E. J. W., Albrecht S., 2010, Nature, 465, 1049

Snellen I. A. G., Brandl B. R., de Kok R. J., Brogi M., Birkby J., Schwarz H., 2014, Nature, 509, 63

Snellen I., et al., 2019, arXiv e-prints, p. arXiv:1908.01803

Sobolev V., 1975, Light scattering in planetary atmospheres. International series of monographs in natural philosophy, Pergamon Press, https://books.google.co.uk/books?id=MLp-AAAAIAAJ

Southworth J., 2011, Monthly Notices of the Royal Astronomical Society, 417, 2166

Stevens D. J., Gaudi B. S., 2013, PASP, 125, 933

Strachan J. B. P., Anglada-Escudé G., 2017, MNRAS, 472, 3467

Strachan J. B. P., Anglada-Escudé G., 2020, MNRAS

Strachan J. B. P., et al., 2020, MNRAS, tbd, tbd

Strassmeier K. G., 2009, A&AS, 17, 251

Struve O., 1952, The Observatory, 72, 199

Suárez Mascareño A., Rebolo R., González Hernández J. I., 2016, A&A, 595, A12

Suárez Mascareño A., et al., 2018, A&A, 612, A89

Sybilski P., Konacki M., Kozłowski S. K., 2010, MNRAS, 405, 657

Szentgyorgyi A., et al., 2018, in Proc. SPIE. p. 107021R, doi:10.1117/12.2313539

Tal-Or L., et al., 2018, A&A, 614, A122

Tarter J. C., Gulkis S., 1993, in American Astronomical Society Meeting Abstracts #182. p. 71.01

Tikhonov A. N., 1977, Solutions of ill-posed problems. John Wiley and Sons

Traub W. A., Oppenheimer B. R., 2010, Direct Imaging of Exoplanets. pp 111–156

Triaud A. H. M. J., et al., 2009, A&A, 506, 377

Trifonov T., et al., 2018, A&A, 609, A117

Tuomi M., Anglada-Escudé G., 2013, Astronomy and Astrophysics, 556, A111

Tuomi M., Anglada-Escudé G., Gerlach E., Jones H. R. A., Reiners A., Rivera E. J., Vogt S. S., Butler R. P., 2013, Astronomy and Astrophysics, 549, A48

Udalski A., et al., 1993, in Akerlof C. W., Srednicki M. A., eds, Vol. 688, Texas/PASCOS '92: Relativistic Astrophysics and Particle Cosmology. p. 626, doi:10.1111/j.1749-6632.1993.tb43947.x

Valenti J. A., Butler R. P., Marcy G. W., 1995, Publications of the Astronomical Society of the Pacific, 107, 966

Vanderburg A., Johnson J. A., 2014, PASP, 126, 948

Vogt S. S., Penrod G. D., 1983, PASP, 95, 565

Vogt S. S., Penrod G. D., Hatzes A. P., 1987, ApJ, 321, 496

Vogt S. S., Marcy G. W., Butler R. P., Apps K., 2000, ApJ, 536, 902

Walker G. A. H., et al., 2006, in Arnold L., Bouchy F., Moutou C., eds, Tenth Anniversary of 51 Peg-b: Status of and prospects for hot Jupiter studies. pp 267–273

Ward-Duong K., et al., 2015, MNRAS, 449, 2618

Wargelin B. J., Kashyap V. L., Drake J. J., García-Alvarez D., Ratzlaff P. W., 2008, ApJ, 676, 610

Wheatley P. J., et al., 2018, MNRAS, 475, 4476

Wilbraham H., 1848, The Cambridge and Dublin Mathematical Journal, 3, 198

Winn J. N., 2010, Exoplanet Transits and Occultations. pp 55–77

Winn J. N., et al., 2007, AJ, 133, 1828

Wolszczan A., Frail D. A., 1992, Nature, 355, 145

Wright J. T., Gaudi B. S., 2012, Exoplanet Detection Methods (arXiv:1210.2471)

Wright J. T., Gaudi B. S., 2013, Exoplanet Detection Methods. p. 489, doi:10.1007/978-94-007-5606-9˙10

Yeh Y., Cummins H. Z., 1964, Applied Physics Letters, 4, 176

Zechmeister M., et al., 2018, A&A, 609, A12

Zechmeister M., et al., 2019, A&A, 627, A49

Zsom A., 2015, The Astrophysical Journal, 813, 9

van Belle G. T., von Braun K., 2009, ApJ, 694, 1085

van de Kamp P., 1963, AJ, 68, 515

List of Figures

List of Tables